

CMS Draft Analysis Note

The content of this note is intended for CMS internal use and distribution only

2020/12/16

Archive Hash: cfc85a1-D

Archive Date: 2020/12/16

Search for long-lived particles decaying into two muons in proton-proton collisions at $\sqrt{s} = 13$ TeV using the CMS scouting data sets

A. Gandrakota¹, A. Lath¹, H. Routray¹, S. Thomas¹, P. Chang², L. Giannini², J. Guiang², V. Krutelyov², M. Masciovecchio², S. May², B. Venkat², F. Würthwein², Y. Xiang², A. Yagil², N. Amin³, C. Campagnari³, H. Mei³, U. Sarica³, S. Wang³, F. Setti³, M. Bryson⁴, S. Chauhan⁴, C. Fangmeier⁴, F. Golf⁴, I. Reed⁴, F. Chen⁵, K. Salyer⁵, D. Spitzbart⁵, I. Suarez⁵, L. Bauerick⁶, K. Burkett⁶, O. Gutsche⁶, R. Heller⁶, S. Jindariani⁶, M. Liu⁶, and H. Weber⁶

¹ Rutgers, The State University of New Jersey, New Brunswick, NJ, USA

² University of California, San Diego, CA, USA

³ University of California, Santa Barbara, CA, USA

⁴ University of Nebraska-Lincoln, Lincoln, NE, USA

⁵ Boston University, Boston, MA, USA

⁶ Fermi National Accelerator Laboratory, Batavia, IL, USA

Abstract

Supporting AN of a search for displaced dimuon resonances using proton-proton collision at a center-of-mass energy of 13 TeV, collected by the CMS experiment at the LHC in 2017–2018, corresponding to an integrated luminosity of 101.3 fb^{-1} . The data sets used in this search were collected using a dedicated dimuon scouting trigger stream, in order to explore otherwise inaccessible phase space at low dimuon mass and non-zero displacement from the interaction point.

This box is only visible in draft mode. Please make sure the values below make sense.

PDFAuthor:	The CMS dimuon scouting team
PDFTitle:	Search for long-lived particles decaying into two muons in proton-proton collisions at $s=13\text{TeV}$ using the CMS scouting data sets
PDFSubject:	CMS
PDFKeywords:	CMS, physics, exotica, long-lived, LLP, low-mass, resonance

Please also verify that the abstract does not use any user defined symbols

1 Contents

2	1	Changes from previous version	2
3	2	Introduction	3
4	3	Data sets, triggers and Monte Carlo simulation	5
5	3.1	Data sets and triggers	5
6	3.2	Monte Carlo simulation	6
7	4	Search strategy	7
8	5	Event selection	10
9	5.1	Baseline selection	10
10	5.2	Additional selections	21
11	6	Trigger scale factors	30
12	7	Signal lifetime reweighting	35
13	8	Parametrization of the signal resonance width	38
14	9	Background estimation in dimuon mass windows	42
15	9.1	Shape analysis: fit of the dimuon mass spectrum	42
16	9.2	Counting experiments	43
17	10	Results and interpretation	47
18	10.1	Systematic uncertainties in the signal yields	47
19	10.2	Constraints on models of BSM physics	48
20	11	Summary	51
21	A	Proof of principle: observation of known resonances	56
22	B	Invariant mass: on the correction of muon ϕ	57
23	C	Alternative signal mass interpolation	59
24	D	Two-dimensional signal acceptance interpolation	62
25	E	Fit vs. counting experiment	63
26	F	On the definition of “masked” mass windows	65
27	G	Bias and goodness-of-fit tests	68
28	H	On the choice of the background fit functional form	75
29	I	Inclusive distributions	76
30	J	Selection cut-flow	84

³¹ **1 Changes from previous version**

- ³² • **V1:** initial empty version of the AN.
- ³³ • **V2:** first full description of analysis.
- ³⁴ • **V3:** implementation of comments by EXO-LL sub-conveners.

DRAFT

35 2 Introduction

36 We describe a search for long-lived dimuon resonances using the dimuon scouting data col-
 37 lected with the CMS experiment during the CERN LHC Run-2, in 2017 and 2018. The 2016
 38 data are not used since the event content differs from 2017 and 2018.

39 Cosmological evidences point to the existence of dark matter [1–4], whose origin is one of the
 40 outstanding targets of particle physics and cosmology. If at all, dark matter is expected to inter-
 41 act very weakly with standard model (SM) particles. This introduces the possibility of a hidden
 42 (dark) sector of particles whose interaction with SM particles may be mediated by a hypothet-
 43 ical dark photon (Z_D) [5, 6]. Indeed, one compelling scenario involves a spontaneously broken
 44 dark $U(1)_D$ gauge symmetry, mediated by such dark photon, Z_D . In this scenario, the only
 45 renormalizable interaction with the SM will be through kinetic mixing with the hypercharge
 46 gauge boson. In addition, if a dark Higgs mechanism is responsible for the spontaneous break-
 47 ing of the $U(1)_D$ gauge symmetry, the dark Higgs boson will have a renormalizable coupling to
 48 the 125 GeV SM-like Higgs boson, resulting in a mixing between the two physical scalar states.
 49 Thus, the hidden sector may interact with the SM either through the hypercharge portal, via
 50 the kinetic mixing coupling (denoted as ϵ), or through the Higgs portal, via the Higgs mix-
 51 ing (denoted as κ). The dark photon Z_D may as well mix with the SM photon (γ) and the Z
 52 boson through the hypercharge portal. In absence of hidden-sector states below the Z_D mass,
 53 this mixing causes Z_D to decay exclusively to SM particles, with sizable branching fraction
 54 to leptons, with the coupling of the SM fermions to Z_D being proportional to ϵ , as shown in
 Fig. 1 (left). If $\epsilon \lesssim 10^{-4}$, then Z_D may be long-lived, as shown in Fig. 1 (right).

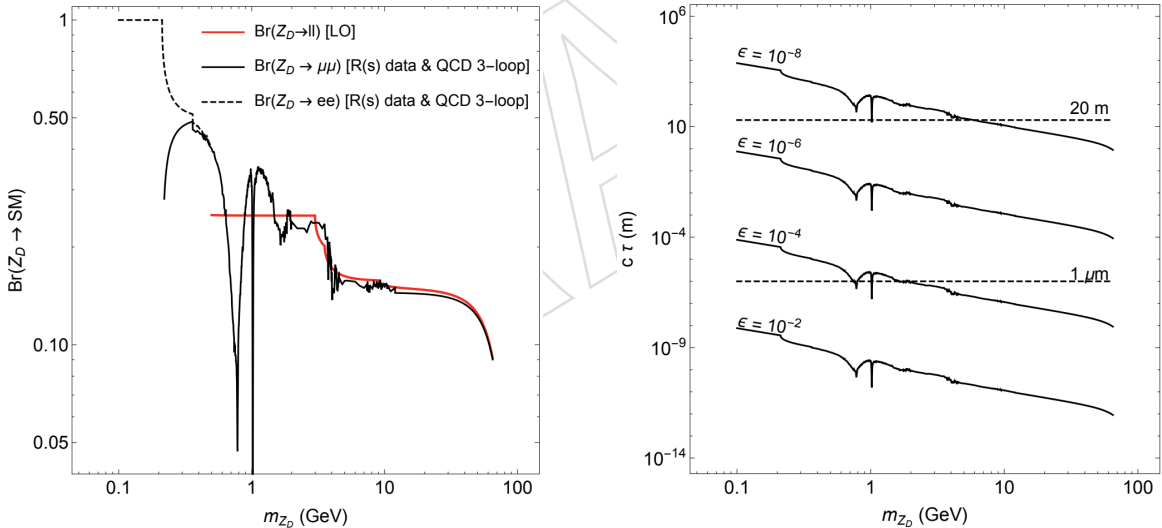


Figure 1: (Left) Leptonic branching ratio (Br) of Z_D as a function of m_{Z_D} [6]. (Right) Decay length ($c\tau$) of Z_D for different ϵ ; the dashed horizontal lines indicate boundaries between qualitatively different experimental regimes: prompt decay for $c\tau \lesssim 1 \mu\text{m}$ and likely escape from the detector for $c\tau \gtrsim 20 \text{ m}$ [6].

55

56 Diagrams in Fig. 2 illustrate the production of one or two Z_D from a Higgs boson (h).
 57 Constraints have been placed on the visible dark photon decays by previous beam-dump [7],
 58 fixed-target [8], collider [9], and rare-meson-decay experiments [10], by the LHCb experiment [11–
 59 13] and by the CMS experiment [14]. Some of these constraints and prospects from other ex-
 60 periments are summarized in Fig. 3.

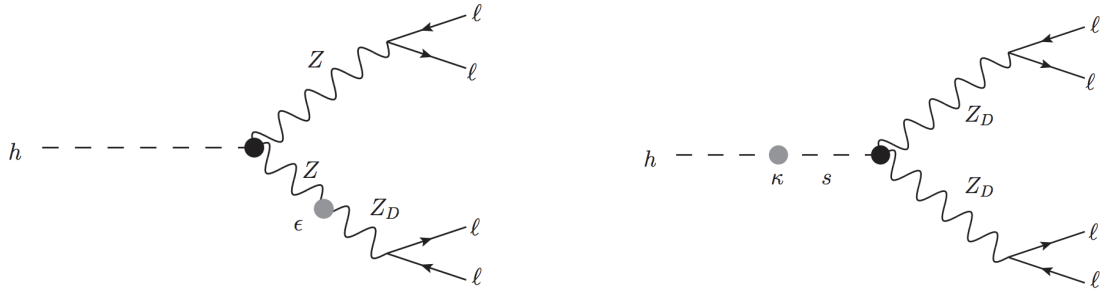


Figure 2: Diagrams illustrating a SM-like Higgs boson (h) decay to four leptons via one or two intermediate Z_D [6]: (left) $h \rightarrow ZZ_D \rightarrow 4\ell$, through the hypercharge portal; (right) $h \rightarrow Z_DZ_D \rightarrow 4\ell$, through the Higgs portal.

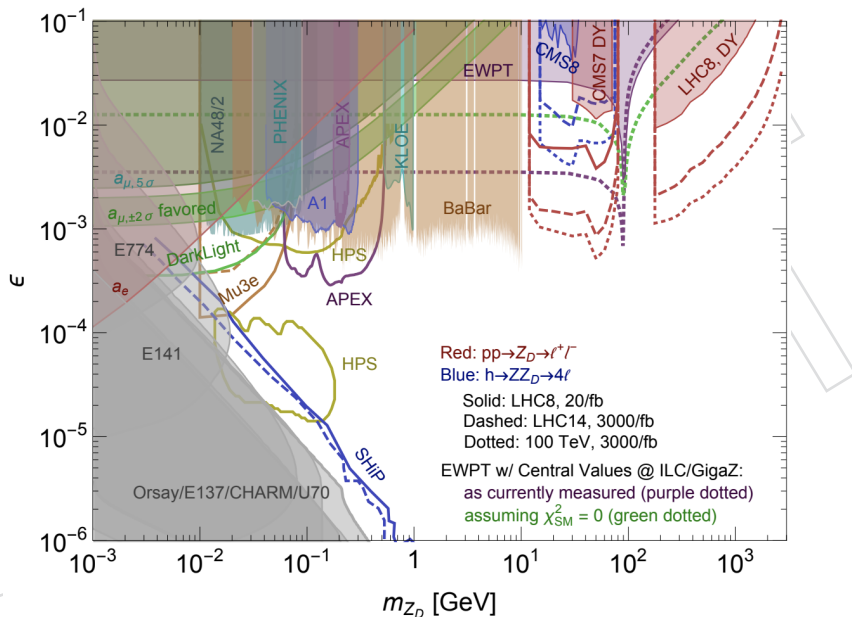


Figure 3: Summary of dark photon constraints and prospects [6].

- 61 Other scenarios may produce a low-mass long-lived resonance decaying into a dimuon pair.
 62 For instance, one of the most minimal extensions to the SM adds a singlet scalar field ϕ , which
 63 mixes with the SM-like Higgs and couples to all SM fermions [15]. Such a scalar resonance may
 64 arise from the decay of a B -meson, $B \rightarrow \phi X_s$, or directly from the proton-proton interaction,
 65 e.g., as illustrated in Fig. 4
- 66 The search presented in this note targets low-mass long-lived resonances decaying into a pair
 67 of oppositely charged muons, where the lifetime of the long-lived particle (LLP) is such that its
 68 decay vertex happens at a transverse displacement from the interaction point of 0–11 cm. The
 69 upper limit of 11 cm in the displacement range from the interaction point is due to a feature
 70 in the definition of the muon scouting trigger stream, which requires the presence of hits in at
 71 least two layers of the CMS pixel tracker. The signal is expected to appear as a narrow peak on
 72 top of the dimuon mass continuum mainly arising from Drell-Yan (DY).
- 73 We note that using scouting data is convenient and effective only in a search targeting low-
 74 mass long-lived resonances: for high-mass prompt signatures, using the standard muon trigger
 75 streams is found to offer better sensitivity [14].

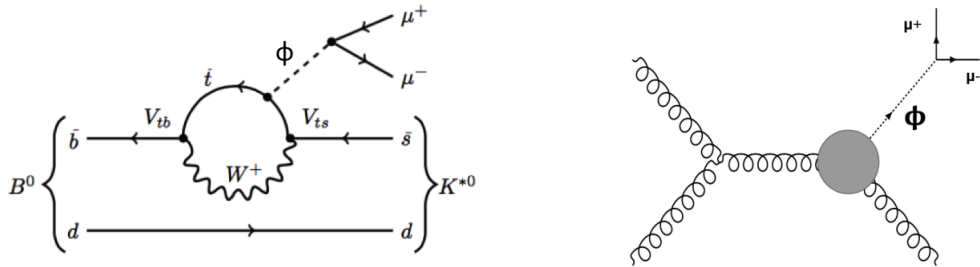


Figure 4: Diagrams illustrating the production of a scalar resonance ϕ (left) via a B -meson decay and (right) via gluon-gluon fusion.

76 3 Data sets, triggers and Monte Carlo simulation

77 3.1 Data sets and triggers

78 A two-level trigger system is employed in CMS. The first level trigger (L1T) consists of custom
 79 hardware processors, using information from the calorimeters and muon detectors to select the
 80 most interesting events in a fixed time interval of less than $4\ \mu\text{s}$. The high-level trigger (HLT)
 81 processor farm further decreases the event rate from around 100 kHz to about 1 kHz, before
 82 data storage. Typically, events are selected containing at least one physics object (e.g., a lepton)
 83 with large transverse momentum (\vec{p}_T). Thus, using standard trigger streams, it is only possible
 84 to search for narrow resonances decaying into two muons with $m_{\mu\mu} \gtrsim 45\ \text{GeV}$.

85 In Run-2, a new trigger scheme was developed, called *data scouting*, with dedicated trigger al-
 86 gorithms aimed at selecting events with dimuon mass $m_{\mu\mu} \gtrsim 200\ \text{MeV}$, at a rate of about 3 kHz.
 87 In order to compensate for the large rate, the event size is reduced by up to a factor of 1000 by
 88 retaining the muon-related information in addition to basic event variables, as reconstructed at
 89 HLT level.

90 A more detailed description of the CMS detector and trigger system, together with a definition
 91 of the coordinate system used and the relevant kinematic variables, can be found in Refs. [16,
 92 17]. More details about the dimuon scouting triggers can be found in Refs. [14, 18, 19]. The
 93 pixel tracker was upgraded before the start of the data taking period in 2017, providing one
 94 additional layer of measurements compared to the older tracker [20].

95 The following data sets are used in this search:

- 96 • 2017: /ScoutingCaloMuon/Run2017*/RAW;
- 97 • 2018: /ScoutingCaloMuon/Run2018*/RAW.

98 The data sets were collected using the data scouting trigger (DST) paths identified as:

- 99 • DST_DoubleMu3_noVtx_CaloScouting_v*.

100 Events with two oppositely charged muons at HLT are selected, each with $p_T^\mu > 3\ \text{GeV}$ and
 101 $|\eta^\mu| < 2.4$.

102 In 2017 (2018), an OR of the following L1T seeds is as well required:

- 103 • DoubleMu4_SQ_OS_dR_Max1p2 (DoubleMu4p5_SQ_OS_dR_Max1p2);
- 104 • DoubleMu0er1p4_SQ_OS_dR_Max1p4;
- 105 • DoubleMu_15.7.

106 The first L1T path preselects events with a pair of oppositely charged L1T muons, each with

¹⁰⁷ $p_T^\mu > 4$ (4.5) GeV and $\Delta R(\mu, \mu) < 1.2$, where $\Delta R(\mu, \mu) = \sqrt{|\Delta\phi(\mu, \mu)|^2 + |\Delta\eta(\mu, \mu)|^2}$. The
¹⁰⁸ second path preselects events with two L1T muons with opposite charge, $|\eta^\mu| < 1.4$ and
¹⁰⁹ $\Delta R(\mu, \mu) < 1.4$. Finally, the third path preselects events containing two L1T muons, with
¹¹⁰ $p_T^{\mu_1} > 15$ and $p_T^{\mu_2} > 7$ GeV.

¹¹¹ All triggers (L1T and HLT) are unprescaled. We always apply a Golden JSON to data for our
¹¹² results. The selected data correspond to a total integrated luminosity of 101.3 fb^{-1} (41.53 fb^{-1}
¹¹³ collected in 2017 and 59.74 fb^{-1} collected in 2018).

¹¹⁴ **For the R&D phase of the analysis, we have randomly selected about 10% of the full data set**
¹¹⁵ **(2017–2018), corresponding to an integrated luminosity of 10.1 fb^{-1} .**

¹¹⁶ 3.2 Monte Carlo simulation

¹¹⁷ 3.2.1 Standard model background

¹¹⁸ The SM background is estimated directly from data, by fitting the dimuon mass distribution
¹¹⁹ with an analytical function. Thus, the search does not rely on Monte Carlo (MC) simulation
¹²⁰ in order to predict the background. However, MC simulation is used to perform data/MC
¹²¹ comparisons to evaluate data/MC scale factors.

¹²² All the SM background samples used in this search are listed in Section 6

¹²³ 3.2.2 Signal beyond the standard model

¹²⁴ The MC simulation of signal beyond the SM (BSM) is used in order to interpret the results of
¹²⁵ the search. Three signal models are simulated, as described in Section 2.

- ¹²⁶ • A model of Higgs boson (H) production via gluon-gluon fusion, with $H \rightarrow Z_D Z_D$,
¹²⁷ where Z_D is a long-lived resonance; one Z_D is set to decay to a pair of oppositely
¹²⁸ charged muons with 100% probability; the other Z_D decays according to the SM
¹²⁹ Z decay table. This model is generated using the POWHEG v2.0 [21–23] generator
¹³⁰ at next-to-leading order (NLO) precision and JHUGEN 7.0.2 [24–28] generator at
¹³¹ leading-order (LO) precision. The JHUGEN generator is used to model the H decay,
¹³² setting the properties (mass and lifetime) of Z_D . The generators are interfaced with
¹³³ PYTHIA 8.2 [29] for the simulation of fragmentation and parton showering. The sig-
¹³⁴ nal production cross section is calculated at next-to-next-to-NLO ($N^3\text{LO}$) in α_S [30].
- ¹³⁵ • A model of scalar resonance ϕ production via gluon-gluon fusion, in association
¹³⁶ with an additional gluon, where ϕ is long-lived and decays to a pair of oppositely
¹³⁷ charged muons with 100% probability. This model is generated with the MAD-
¹³⁸ GRAPH5_aMC@NLO 2.3.3 generator [31] at LO precision, interfaced with PYTHIA 8.2
¹³⁹ to set the ϕ lifetime and decay mode as well as for the simulation of fragmentation
¹⁴⁰ and parton showering. The signal production cross section is taken directly from the
¹⁴¹ generator, at LO in α_S .
- ¹⁴² • A model of scalar resonance ϕ production via the decay of a B -hadrons, where ϕ is
¹⁴³ long-lived and decays to a pair of oppositely charged muons with 100% probability;
¹⁴⁴ all B -hadrons are considered, and each is set to decay according to its SM decay
¹⁴⁵ table with 50% probability, and as $B \rightarrow \phi X$ the other 50% of the times. This model is
¹⁴⁶ generated at LO precision using PYTHIA 8.2. The signal production cross section is
¹⁴⁷ calculated at fixed-to-next-to-the-leading (FONLL) order in α_S [32–35]. The FONLL
¹⁴⁸ calculations are as well used to reweight the B -hadron p_T spectrum.

¹⁴⁹ The CP5 PYTHIA 8.2 tune [36] and NNPDF3.1 sets of parton distribution functions (PDFs) [37]

150 are used. The detector response is simulated with a GEANT4 model [38] of the CMS detector.
 151 Multiple pp interactions are superimposed on the hard collision (pileup), and the simulated
 152 samples are reweighted such that the number of collisions per bunch crossing accurately re-
 153 flects the distribution observed in data.

154 The search is targeting a dimuon mass range from about 200 MeV (i.e., $m_{\mu\mu} \gtrsim 2m_\mu$) to about
 155 25 GeV, and a transverse displacement range $0 < l_{xy} < 11$ cm from the interaction point. For
 156 larger dimuon masses, using the standard trigger streams (instead of scouting data) is shown
 157 to become convenient [14], especially from promptly decaying resonances. The hard cut-off
 158 in transverse displacement at 11 cm is due to a feature of the scouting trigger stream, which
 159 requires the presence of hits in at least two layers of the CMS pixel tracker. Signal samples are
 160 generated to cover the full ranges of interest, in both $m_{\mu\mu}$ and $c\tau$ dimensions. For the model
 161 of scalar resonance (ϕ) production via the decay of a B -meson, only masses $m_\phi \lesssim 5$ GeV are
 162 simulated: larger masses would be highly kinematically disfavored.

163 A fixed coarse grid of $(m_{\phi/Z_D}, c\tau_0^{\phi/Z_D})$ signal points for each model is generated, then we
 164 perform a lifetime-based reweighting (Section 7) as well as a parametrization of the signal
 165 resonance width as a function of its mass (Section 8). Finally, in order to determine the signal
 166 acceptance in a finer $(m_{\phi/Z_D}, c\tau_0^{\phi/Z_D})$ grid, a two-dimensional interpolation method is used
 167 that combines the previous procedures, in bins of l_{xy} , as described in Appendix D.

168 **In order to allow for simpler interpretation (and reinterpretation) of the results, only sig-
 169 nal events with a single long-lived particle decaying into a pair of muons are selected at
 170 generator-level, for all signal models used in this search.**

171 4 Search strategy

172 This search primarily targets low-mass displaced dimuon resonances, characterized by the de-
 173 cay of a long-lived particle into a pair of muons. Therefore, the primary handle to be exploited
 174 in order to discriminate a potential signal from the SM background is the presence in each
 175 event of a pair of muons and of an associated displaced vertex (DV). Most of the physics pro-
 176 cesses contributing to the SM background are expected to be highly suppressed at increasing
 177 displacement from the primary vertex (PV). Because the vertex position resolution along the
 178 z -axis is not as good as the one achieved in the transverse (xy) plane, we exploit the transverse
 179 displacement of the DV, l_{xy} , in order to categorize events, in the attempt to maximize the search
 180 sensitivity to a range of potential BSM signal lifetimes. We note that vertices in proximity of a
 181 tracker module are vetoed, in order to suppress the presence of material vertices (as described
 182 in detail in Section 5.2).

183 In order to define l_{xy} categories, the CMS pixel tracker geometry is taken into account, as illus-
 184 trated in Fig. 5. In particular, Fig. 5 depicts the transverse position of the three innermost pixel
 185 tracker layers.

186 The l_{xy} categories are defined as follows:

- 187 • Within beam pipe:

188 [0.0, 0.2] cm

189 [0.2, 1.0] cm

190 [1.0, 2.4] cm

- 191 • Between beam pipe and 1st pixel tracker layer:

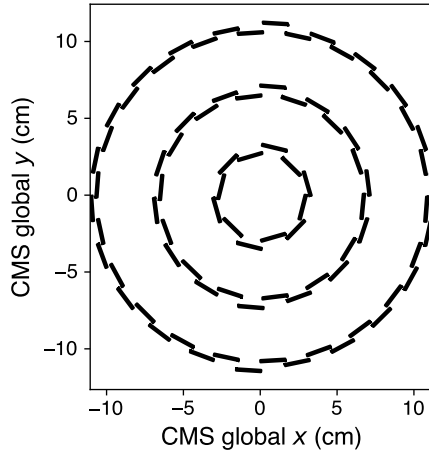


Figure 5: Illustration of the CMS pixel tracker geometry in 2017–2018: the transverse position of the three innermost pixel tracker layers is depicted.

[2.4, 3.1] cm

- Between 1st and 2nd pixel tracker layers:

[3.1, 7.0] cm

- Between 2nd and 3rd pixel tracker layers:

[7.0, 11.0] cm

In each l_{xy} category, we further divide events in bins of dimuon transverse momentum, $p_T^{\mu\mu}$.

This allows to maximize the sensitivity to different signal topologies, as shown in Fig. 6: $p_T^{\mu\mu}$ tends to be low in signal models where long-lived particles arise from the decay of a B -hadron, while it is expected to be larger in other models.

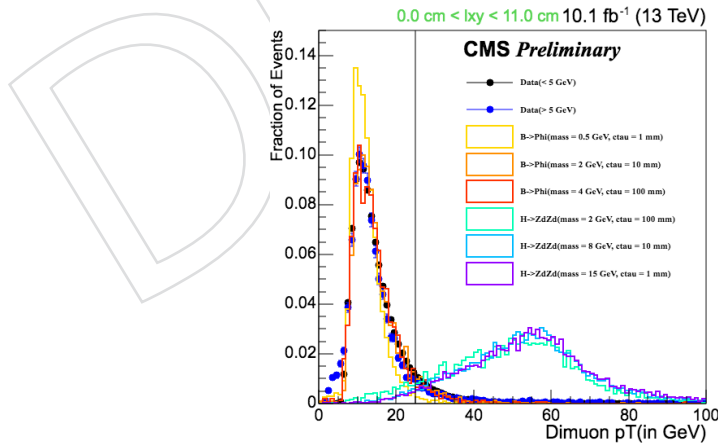


Figure 6: Distribution of $p_T^{\mu\mu}$ for data (10.1 fb^{-1}) and illustrative benchmark signal models, after applying the full event selection (see Section 5).

Finally, in each $(l_{xy}, p_T^{\mu\mu})$ category, events are divided in bins of isolation (to distinguish “isolated” and “non-isolated” topologies), in order to enhance the search sensitivity to signal models with long-lived particles arising from B -hadron decays, where muons tend to be not isolated due to the nearby presence of other B -hadron decay products. Further details on isolation are

- 205 provided in Section 5.
- 206 In each $(l_{xy}, p_T^{\mu\mu}, \text{isolation})$ bin, we define mass windows sliding along the dimuon invariant
207 mass spectrum, and we perform a search for a resonant dimuon peak in each mass window.
- 208 For mass windows where statistics allows, the SM background is estimated from a fit of the
209 dimuon mass distribution in data. For windows with low data statistics, the background is
210 instead estimated from sidebands by means of a constant transfer factor. This is explained in
211 detail in Section 9. Mass windows in each $(l_{xy}, p_T^{\mu\mu}, \text{isolation})$ bin are then used as input to a
212 final likelihood fit for the interpretation of the results, as described in Section 10.

213 The overall search strategy as described above is illustrated in Fig.7.

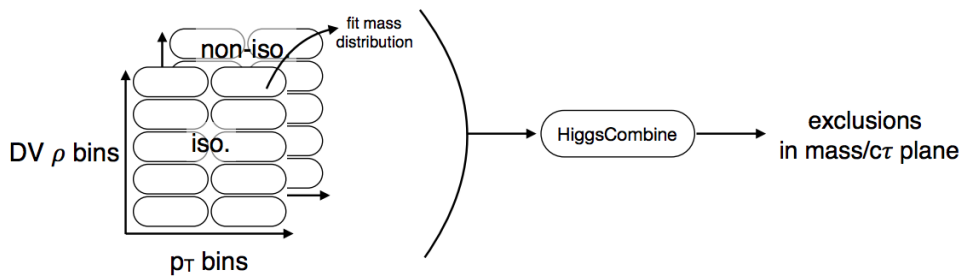


Figure 7: Plot illustrating the dimuon p_T of the signals signifying different phase space coverage. All analysis selections(see Section 5) have been applied.

214 5 Event selection

215 The events are collected using the DST paths and L1T seeds detailed in Section 3.1, and are
 216 required to satisfy the selection criteria described in the following. The selected events are
 217 then divided in categories, defined in order to maximize the search sensitivity to a range of BSM
 218 physics signatures, as already depicted in Section 4.

219 As described in Section 3.1, a limited amount of information is retained for events collected
 220 using the scouting trigger stream, in order to compensate for the large data-taking rate. This
 221 information is the result of the event reconstruction at HLT. The baseline selection criteria used
 222 in this search, as well as the event categorization, are therefore based on objects and event
 223 variables as reconstructed at HLT.

224 The events collected using the DST paths and L1T seeds detailed in Section 3.1, are preliminarily
 225 selected to contain at least a pair of oppositely charged (opposite-sign, OS) muons associated
 226 to a displaced vertex (DV). A large fraction of events contain only one OS muon pair and an
 227 associated DV. Among those events with more than a pair of OS muons, if more pairs satisfy
 228 the baseline selection described below then only the pair whose associated DV has the lowest
 229 transverse (x, y) error is used.

230 In the following, we describe the selection criteria used on top of the DST paths and L1T seeds
 231 detailed in Section 3.1, separating baseline (Section 5.1) and additional (Section 5.2) selection
 232 criteria.

233 The selection efficiency for background is mainly evaluated in data (10.1fb^{-1}), because simula-
 234 tion is not sufficient nor reliable in the phase-space of interest of this search (i.e., low-mass
 235 displaced dimuon signatures). For signal, we instead use signal simulation as described in Sec-
 236 tion 3. Selection cut-flow efficiencies for data (10.1fb^{-1}) and signal simulation are presented in
 237 Appendix J.

238 5.1 Baseline selection

239 5.1.1 Muon selection

240 The DST paths used in this analysis require each muon to have $p_T > 3\text{ GeV}$ and $|\eta| < 2.4$.
 241 This is shown in Figs. 8-9, for the second-highest p_T muon in each event (also referred to as
 242 “trailing muon”), for data as well as for illustrative signal models, in three different l_{xy} ranges.
 243 In Figs. 8-9, only DST and L1T selections are applied, and data events are further categorized
 244 according to the reconstructed dimuon invariant mass ($m_{\mu\mu} < 5\text{ GeV}$, or $m_{\mu\mu} > 5\text{ GeV}$). We
 245 divide data into events with low- and high-mass dimuon pairs in order to separate as much
 246 as possible the low-mass physics processes involving the production and decay of B -hadrons
 247 from other SM processes.

248 All muons with $p_T > 3\text{ GeV}$ and $|\eta| < 2.4$ are used in this search: more stringent selections,
 249 especially in p_T , would limit the analysis sensitivity to low-mass dimuon resonances, as also
 250 visible from Fig. 8.

251 For data, we use 10.1 fb^{-1} of pp collisions, corresponding to about 10% of all runs in both 2017
 252 and 2018 data-taking periods.

253 On top of p_T and η selections, muons are required to satisfy additional quality criteria:

- 254 • the $\frac{\chi^2}{N\text{dof}}$ of each muon is required to be less than 3, as depicted by the red vertical
 255 line in Fig. 10 (left);

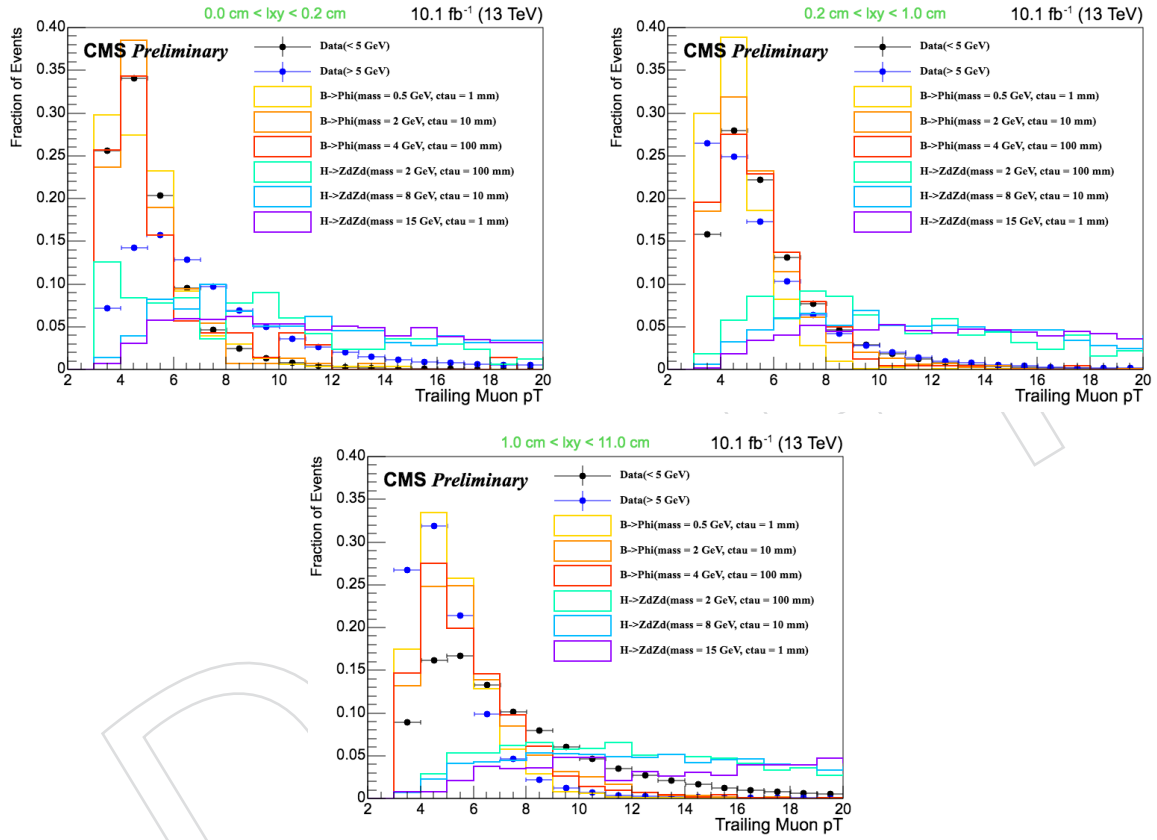


Figure 8: Distribution of trailing muon p_T for data and selected signal models in three different l_{xy} ranges. All events collected with DST paths and L1T seeds detailed in Section 3.1 are displayed.

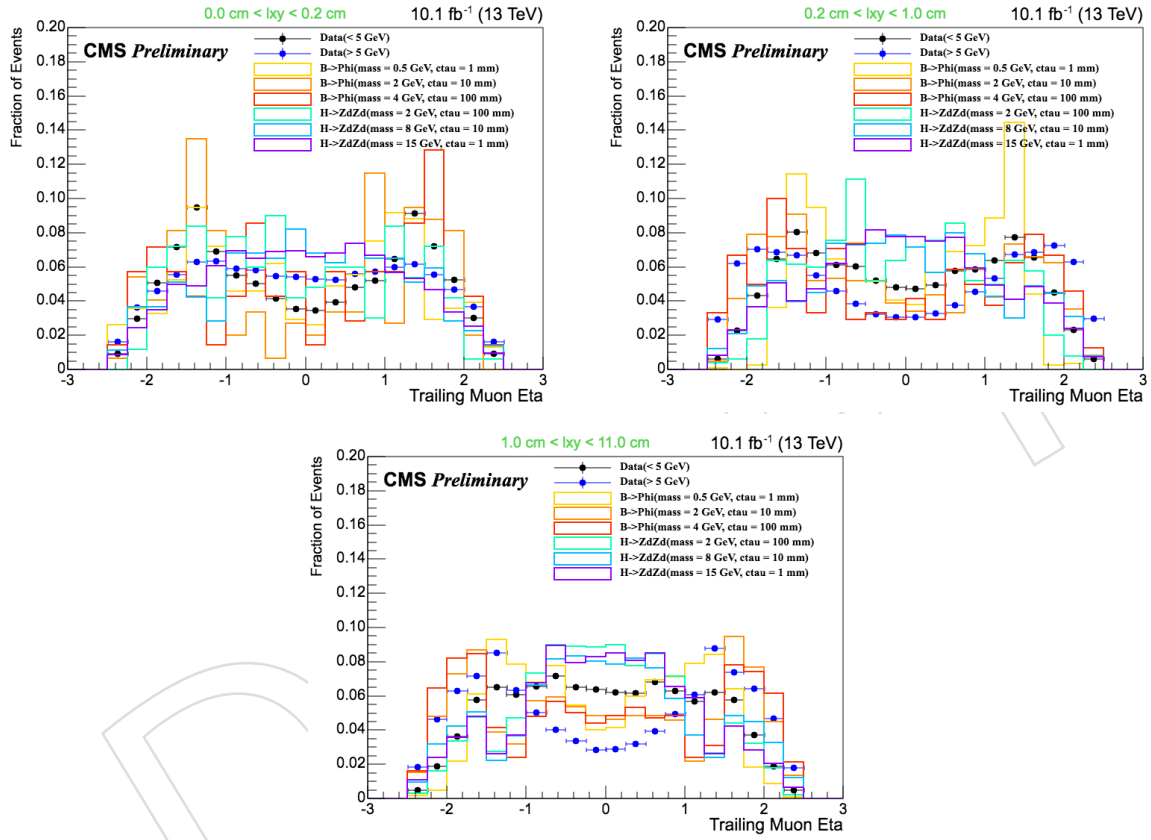


Figure 9: Distribution of trailing muon η for data and selected signal models in three different l_{xy} ranges. All events collected with DST paths and L1T seeds detailed in Section 3.1 are displayed.

- 256 • the number of tracker layers with a measurement is required to be larger than 5, as
 257 depicted by the red vertical line in Fig. 10 (right).

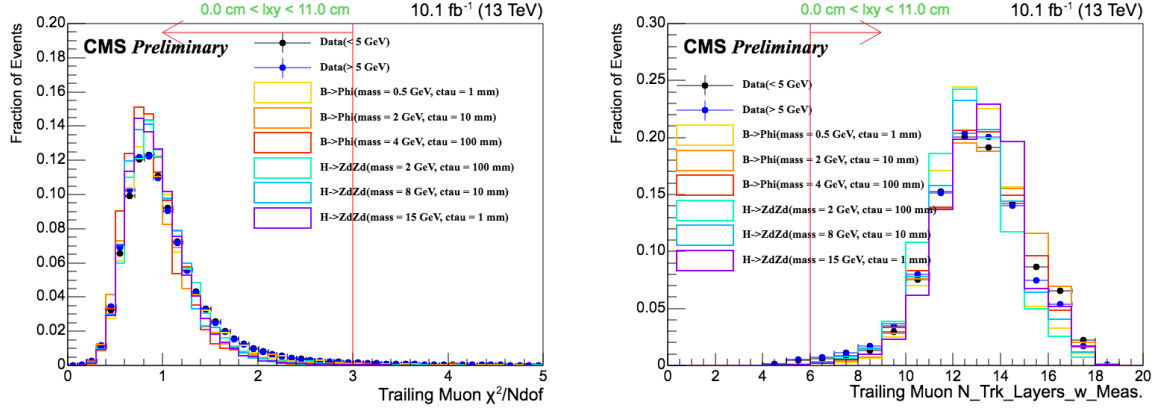


Figure 10: Illustration of additional muon quality cuts (depicted as red vertical lines): (left) $\frac{\chi^2}{N_{dof}}$ is required to be less than 3; (right) the number of tracker layers with a measurement is required to be larger than 5. All events collected with DST paths and L1T seeds detailed in Section 3.1 are displayed.

258 **5.1.2 Displaced vertex selection**

259 The displaced vertex associated to the muon pair is also required to satisfy quality criteria:

- 260 • x error < 0.05 cm;
- 261 • y error < 0.05 cm;
- 262 • z error < 0.10 cm;
- 263 • $\chi^2/\text{ndof} < 5$;
- 264 • $l_{xy} < 11$ cm.

265 Distributions of all selection variables are shown in Fig. 11, overlaying data and one benchmark
266 signal model, for all events collected using DST paths and L1T seeds detailed in Section 3.1.

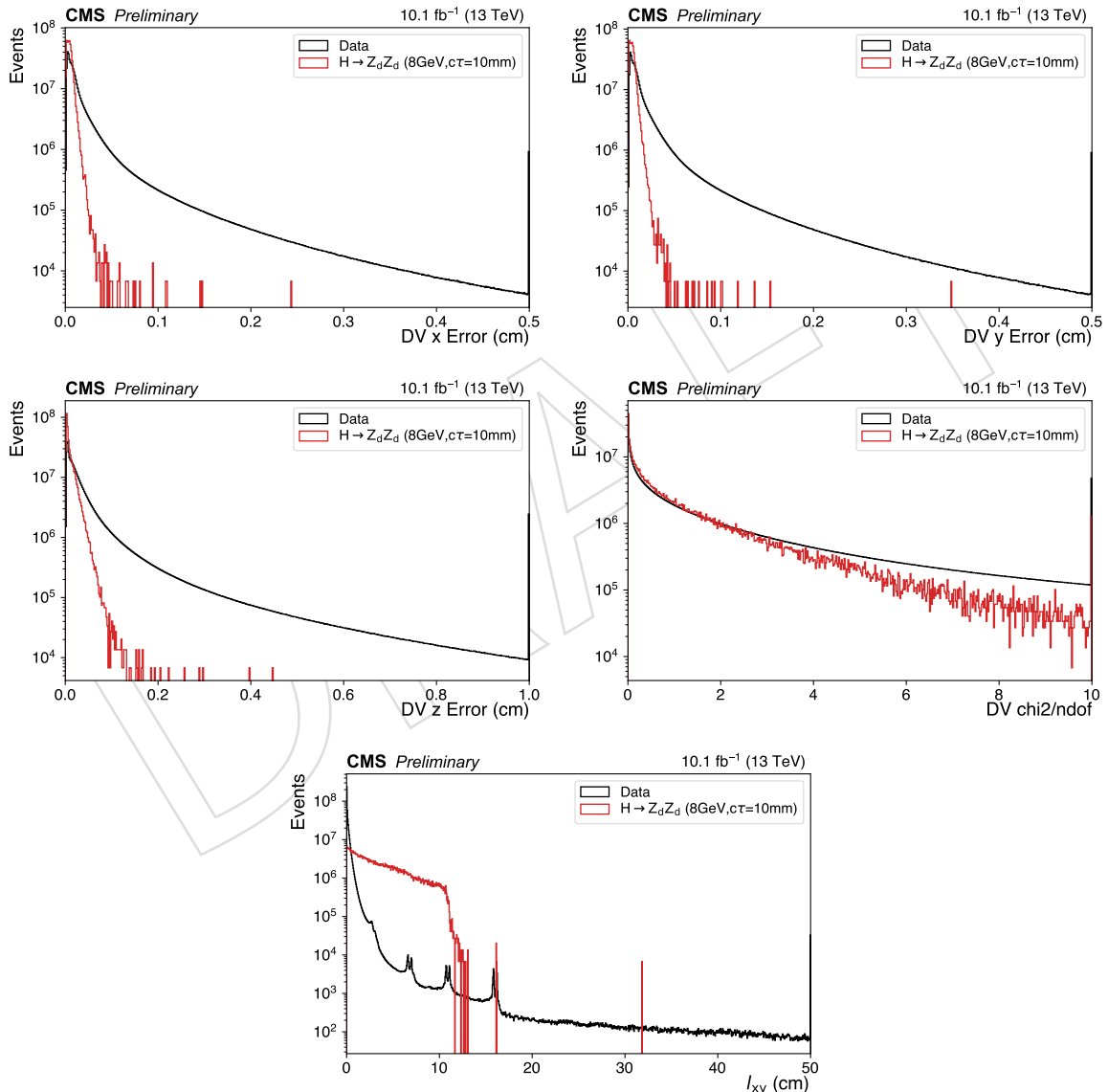


Figure 11: Distribution of DV x error, y error, z error, χ^2/ndof , and l_{xy} for data (10.1fb^{-1}) and a benchmark signal model. All events collected with DST paths and L1T seeds detailed in Section 3.1 are displayed.

²⁶⁷ **5.1.3 Dimuon kinematics: $\Delta\phi(\mu, \mu)$ and $\Delta\phi(\mu, \overrightarrow{DV})$**

²⁶⁸ Figure 12 illustrates the decay of a long-lived particle into a muon pair along with the associated
²⁶⁹ DV.

²⁷⁰ For BSM signal, we expect the dimuon system vector to be collinear with the DV vector, which
²⁷¹ is defined as the vector connecting DV and PV. On the other hand, this does not necessarily
²⁷² apply to muon pairs wrongly associated to the same DV. The $\Delta\phi(\mu, \overrightarrow{DV})$ distribution is
²⁷³ shown in Fig. 13 for data (10.1fb^{-1}) and for illustrative signal models: in this search, we require
²⁷⁴ $\Delta\phi(\mu, \overrightarrow{DV}) < 0.02$.

²⁷⁵ The distribution of $\Delta\phi(\mu, \mu)$ is shown in Fig. 14, for the same data and signal models. While
²⁷⁶ the value of $\Delta\phi(\mu, \mu)$ strongly depends on the boost of the dimuon system, it tends to be very
²⁷⁷ large for muon pairs which are wrongly associated to the same DV. For this reason, in order to
²⁷⁸ reject such pairs, we require $\Delta\phi(\mu, \mu) < 2.8$.

²⁷⁹ In Figs. 13-14, all selections described in Sections 3.1, 5.1.1, and 5.1.2 are applied.

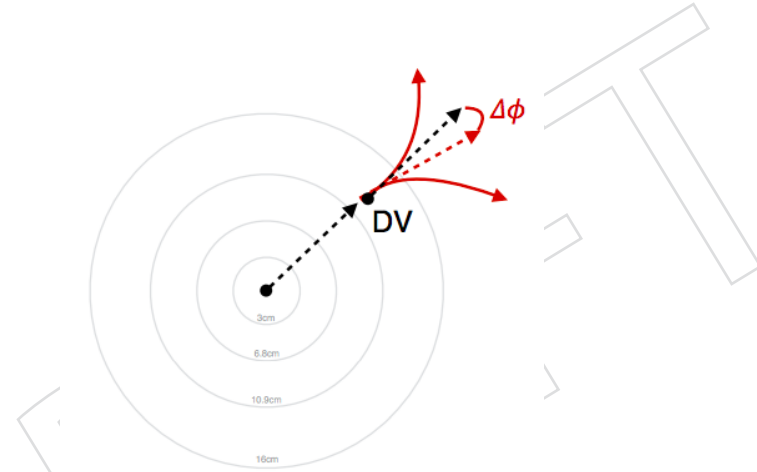


Figure 12: An illustration of a long-lived particle decay into a pair of muons.

²⁸⁰ We note that, in order to improve the dimuon invariant mass ($m_{\mu\mu}$) resolution, the ϕ component
²⁸¹ of each muon is recomputed to account for its displacement with respect to the beamspot. Each
²⁸² muon is propagated (via simple helix propagation) from its reference point (nominally defined
²⁸³ as the point of closest approach to the center of CMS) to the position of the associated DV, and
²⁸⁴ the ϕ component of the muon vector is updated accordingly. Because of the absence of bending
²⁸⁵ in the $\rho - z$ plane, no correction is required for the η component of the muon itself. The effect
²⁸⁶ of the correction is mainly relevant at large displacements. This procedure and its effect are
²⁸⁷ described in detail in Appendix B.

²⁸⁸ The correction of the muon ϕ component is not applied for the computation of $\Delta\phi(\mu, \mu)$ and
²⁸⁹ $\Delta\phi(\mu, \overrightarrow{DV})$: the main goal of such selections is to suppress background where “fake” displaced
²⁹⁰ vertices are formed from cosmic muons, or from muons from different vertices. Therefore, in
²⁹¹ this case the ϕ correction would be applied with respect to a “fake” DV, making the correction
²⁹² itself not meaningful and the selections less effective.

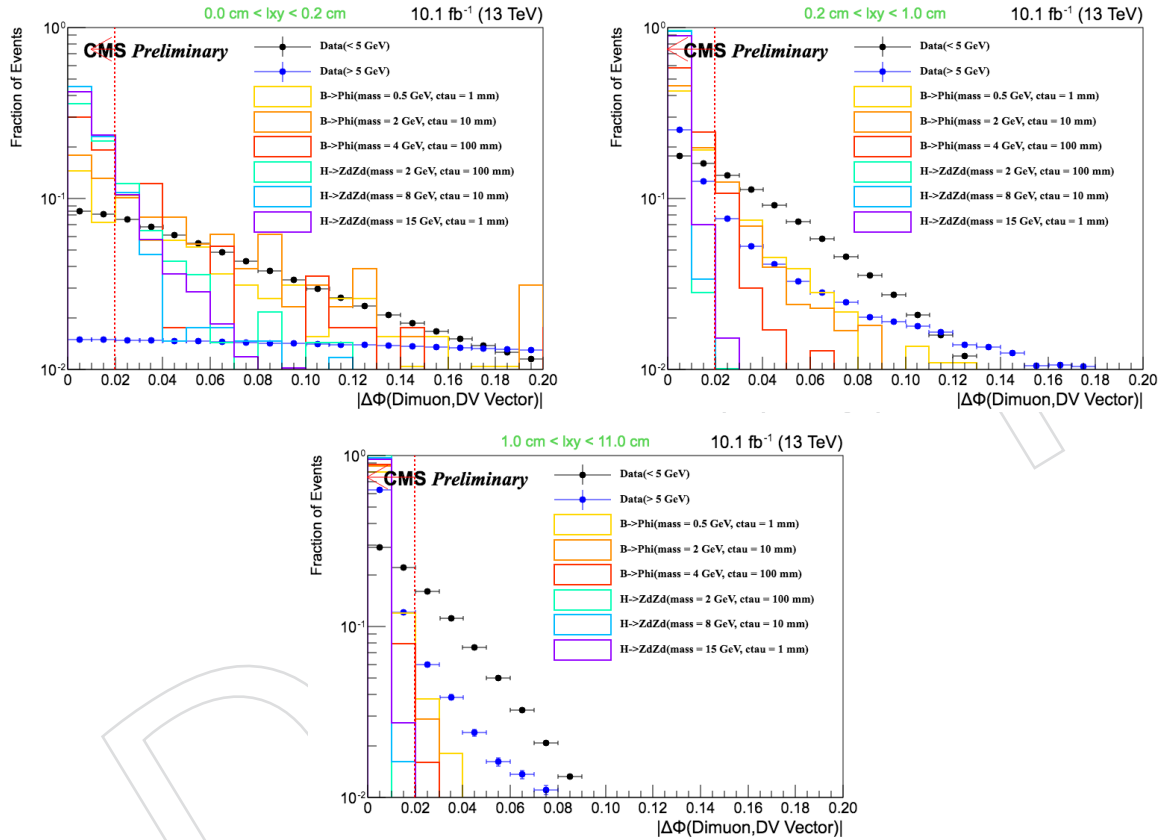


Figure 13: Distribution of $\Delta\phi(\mu, \bar{D}\bar{V})$ in data (10.1fb^{-1}) and illustrative signal models in three different l_{xy} ranges. The cut value is indicated by the red vertical dashed line. All selections described in Sections 3.1, 5.1.1, and 5.1.2 are applied.

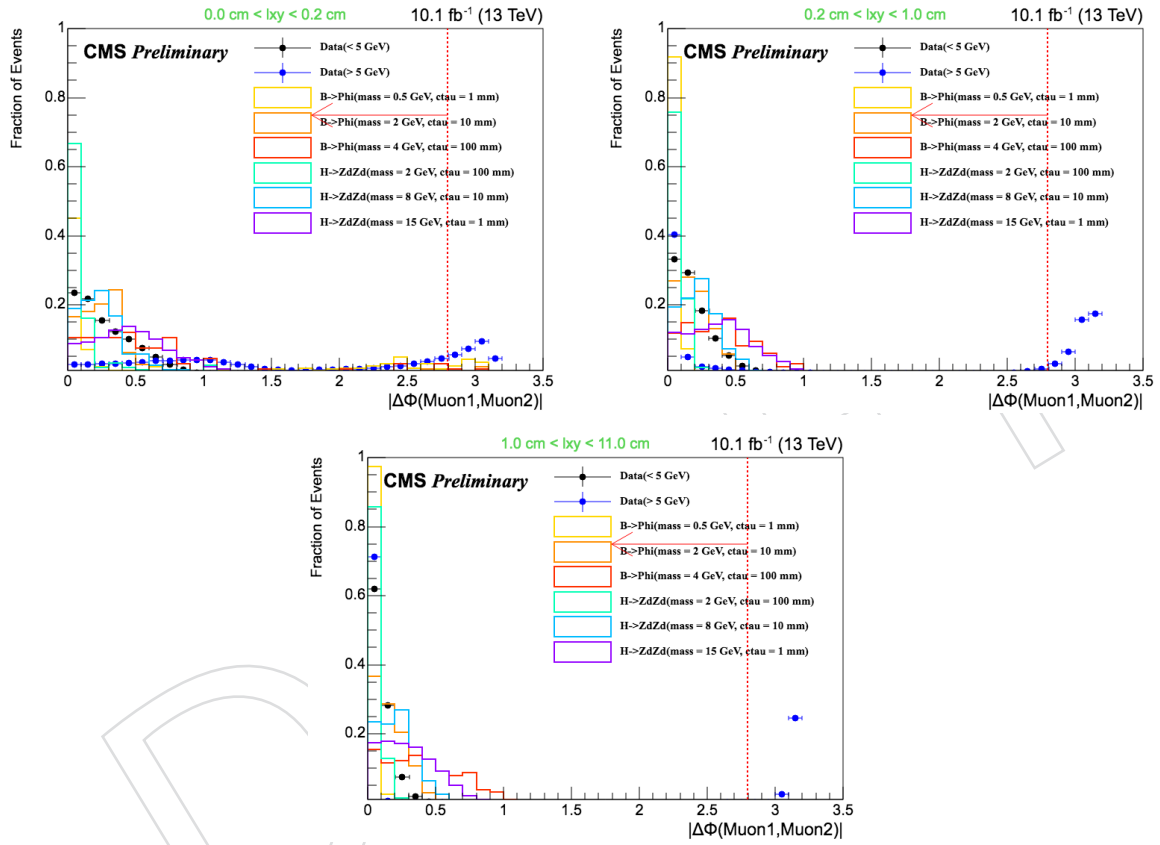


Figure 14: Distribution of $\Delta\phi(\mu, \mu)$ in data (10.1fb^{-1}) and illustrative signal models in three different l_{xy} ranges. The cut value is indicated by the red vertical dashed line. All selections described in Sections 3.1, 5.1.1, and 5.1.2 are applied.

293 **5.1.4 Muon isolation**

294 Muon isolation in the scouting data set is evaluated by means of:

- 295 • relative track isolation;
 296 • minimum $\Delta R(\mu, \text{jet})$.

297 The muon relative track isolation is computed as the p_T sum of tracks within $\Delta R(\mu, \text{track}) <$
 298 0.3, divided by p_T^μ . Tracks from the “hltIter2L3MuonMergedNoVtx” track collection are used,
 299 with $p_T > 0.05 \text{ GeV}$, if they are within $|d_z| < 0.2$ and $|d_{xy}| < 0.1$ of the muon vertex; a veto for
 300 tracks within $\Delta R(\mu, \text{track}) < 0.01$ is applied, while the leading track is always vetoed if it has
 301 $p_T > 2 \text{ GeV}$ and is within $\Delta R(\mu, \text{track}) < 0.025$. The muon relative track isolation distribution
 302 is shown in Fig. 15, for data (10.1 fb^{-1}) and illustrative signal models, after applying all selection
 303 criteria described in Sections 3.1, 5.1.1, 5.1.2, and 5.1.3.

304 The minimum $\Delta R(\mu, \text{jet})$ is calculated considering all jets (“hltAK4CaloJetsIDPassed”) with
 305 $p_T > 20 \text{ GeV}$ and $|\eta| < 3.0$. Its distribution is shown in Fig. 16, for data (10.1 fb^{-1}) and illus-
 306 trative signal models, after applying all selection criteria described in Sections 3.1, 5.1.1, 5.1.2,
 307 and 5.1.3.

308 A muon is considered to be isolated if the following criteria are satisfied:

- 309 • relative track isolation < 0.1 ;
 310 • minimum $\Delta R(\mu, \text{jet}) > 0.3$.

311 As described in Section 4, in this search we explore both isolated and non-isolated topologies.
 312 Isolated topologies consist of events where both muons are isolated; non-isolated topologies
 313 consist of events where exactly one of the two muons fails the isolation criteria.

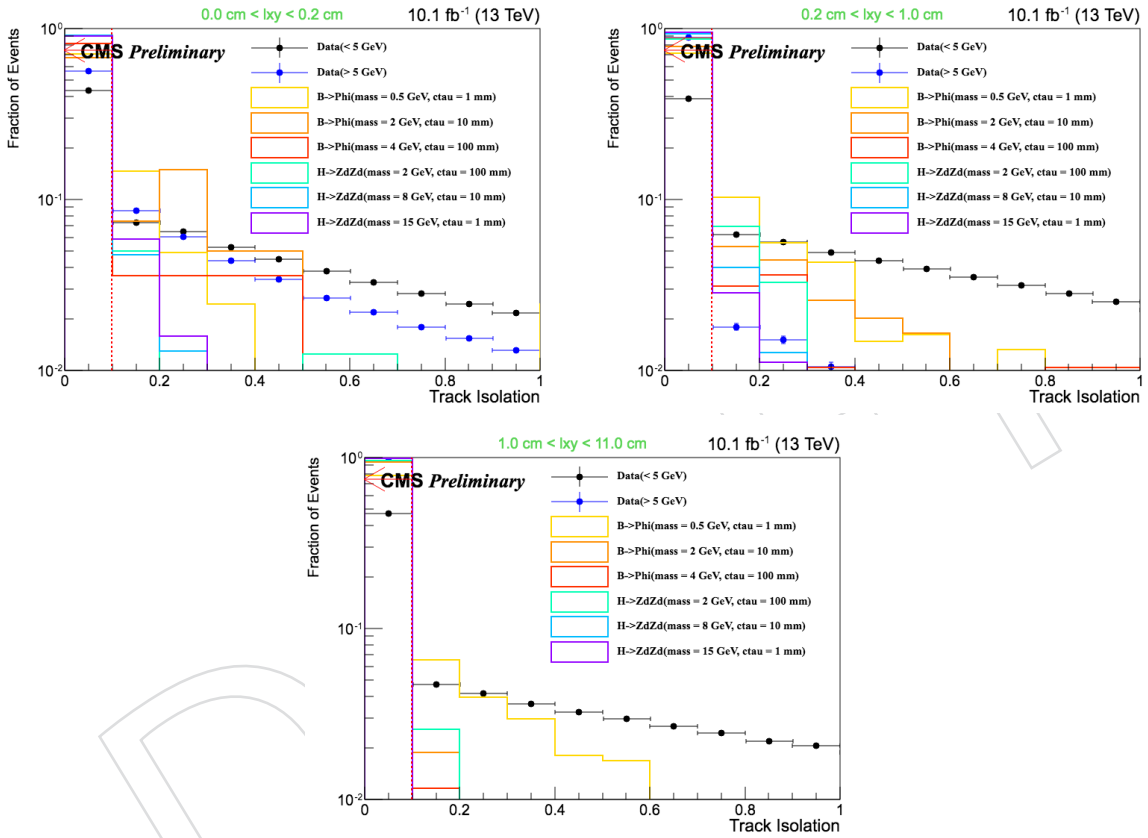


Figure 15: Distribution of the muon relative track isolation in data (10.1fb^{-1}) and illustrative signal models, in three different l_{xy} ranges. The cut value is indicated by the red vertical dashed line. All selections described in Sections 3.1, 5.1.1, 5.1.2 and 5.1.3 are applied.

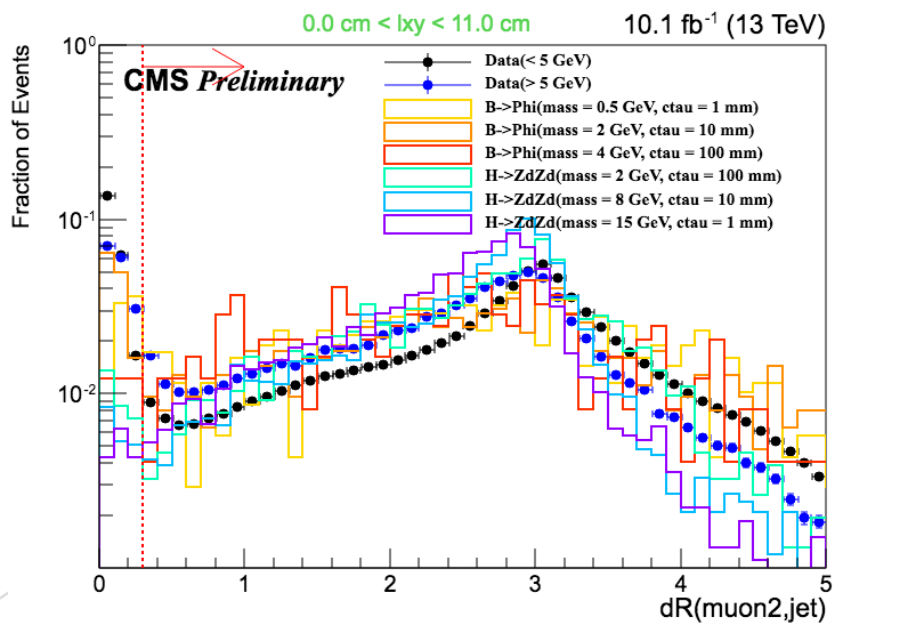


Figure 16: Distribution of the minimum $\Delta R(\mu, \text{jet})$, for the trailing muon, in data (10.1 fb^{-1}) and illustrative signal models, in three different l_{xy} ranges. The cut value is indicated by the red vertical dashed line. All selections described in Sections 3.1, 5.1.1, 5.1.2 and 5.1.3 are applied.

314 **5.2 Additional selections**

315 On top of the baseline selection criteria described in Section 5.1, we define additional criteria
 316 to further suppress the background. Potential background sources include material vertices,
 317 “fake” vertices from pileup, and prompt muons.

318 **5.2.1 Excess pixel hits**

319 We expect truly displaced muons not to leave any hits on the tracker layers between the beamspot
 320 and the displaced vertex (DV). While the observed muon pixel hit multiplicity is directly ac-
 321 cessible in the scouting data format, the expected multiplicity is calculated in multiple steps:

- 322 • first, the muon trajectory is propagated from its reference point to the DV posi-
 323 tion [39];
- 324 • from the DV position, the trajectory is further propagated outwards [39];
- 325 • then, the compatibility of the propagated trajectory with pixel tracker layers is veri-
 326 fied [40];
- 327 • finally, the expected pixel hit multiplicity is defined as the number of valid hits on
 328 pixel tracker layers which are found to be compatible with the muon trajectory, after
 329 the latter is propagated outwards starting from the DV position.

330 The number of excess pixel hits is defined as the difference between observed and expected
 331 hits for each μ -track. Fig. 17 shows excess pixel hits calculated after applying all selection cri-
 332 teria described in Sections 3.1 and 5.1, except for isolation: especially at large l_{xy} , a significant
 333 fraction of muons in data events is found to be characterized by a non-zero number of excess
 334 hits, while this is not the case for signal. We require the number of excess pixel hits to be ≤ 0 ,
 335 for all muons that are associated to a DV at $l_{xy} > 3.5$ cm. Such requirement is only applied at
 336 $l_{xy} > 3.5$ cm to ensure that the DV is located beyond the first pixel tracker layer (see Fig. 5).

337 **5.2.2 Pileup muon veto**

338 As illustrated in Fig. 18, muons from pileup vertices could overlap in the $\rho - \phi$ plane de-
 339 spite being apart in $\rho - z$; as a consequence, they could be wrongly associated to a com-
 340 mon “fake” DV. The involved muon pairs are characterized by a large $\Delta\eta(\mu, \mu)$ and a small
 341 $\Delta\phi(\mu, \mu)$. We exploit this feature to suppress such background contribution, by requiring
 342 $\log_{10}(|\Delta\eta_{\mu\mu}| / |\Delta\phi_{\mu\mu}|) < 1.25$, as shown in Fig. 19 for data and illustrative signal models af-
 343 ter all selection criteria in Sections 3.1, 5.1, and 5.2.1 are applied, except for isolation.

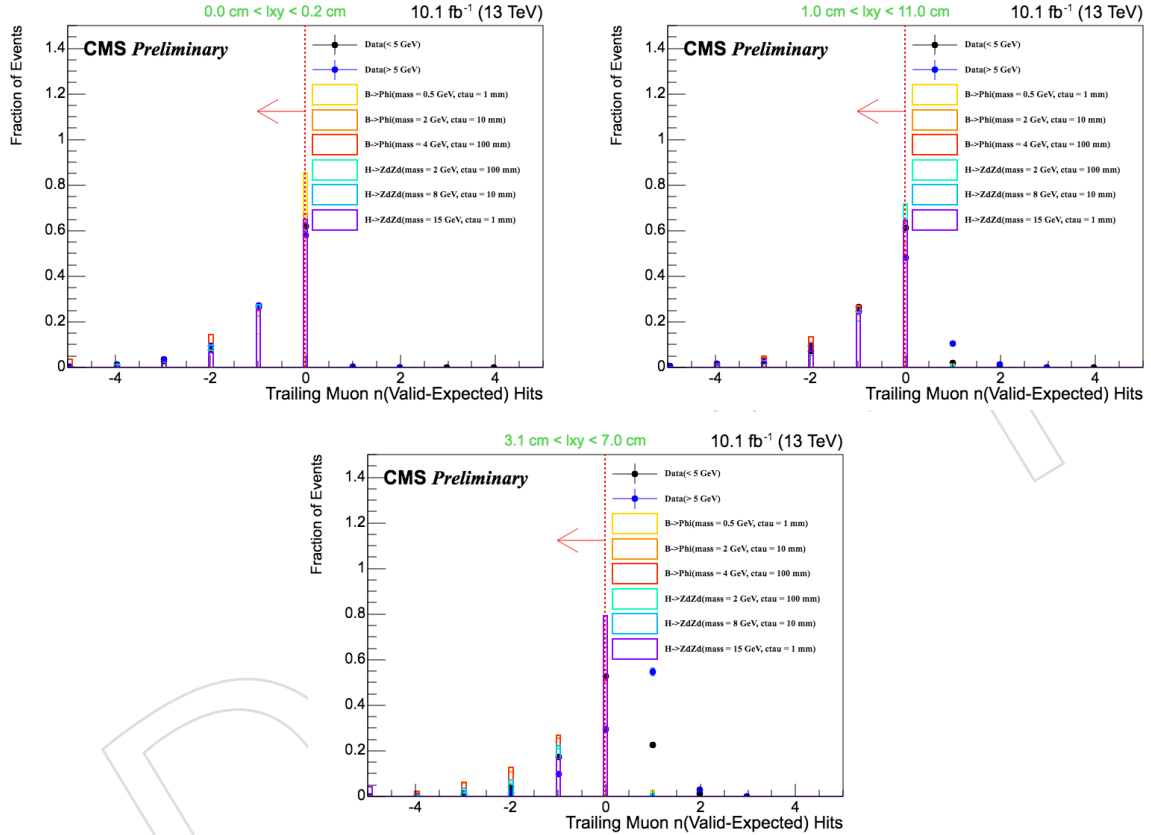


Figure 17: Distribution of number of excess pixel hits in data and illustrative signal models, in three different l_{xy} ranges. The cut value is indicated by the red vertical dashed line (the cut is only applied at $l_{xy} > 3.5 \text{ cm}$). All selections described in Sections 3.1 and 5.1 are applied, except for isolation.

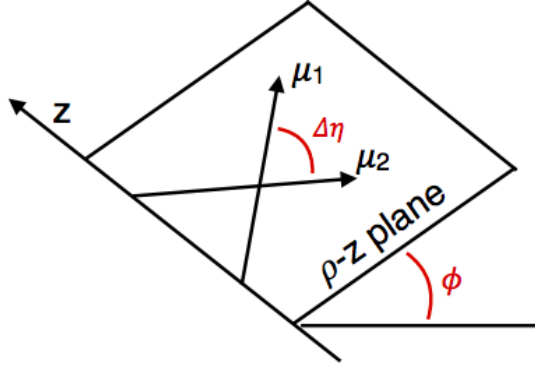


Figure 18: Illustration: muons from pileup vertices could overlap in the $\rho - \phi$ plane despite being apart in $\rho - z$; as a consequence, they could be wrongly associated to a common “fake” DV.

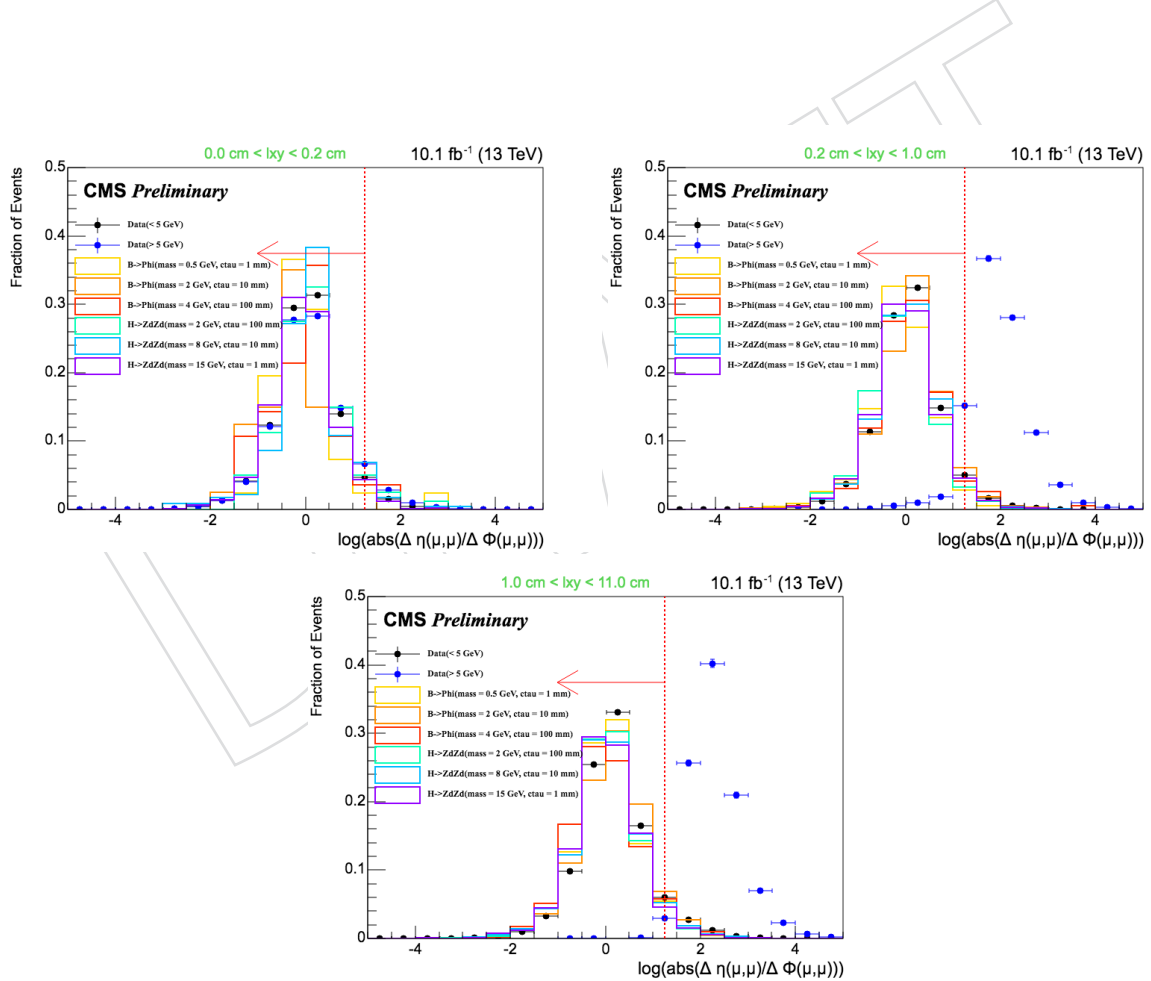


Figure 19: Distribution of $\log_{10}(|\Delta\eta_{\mu\mu}|/|\Delta\phi_{\mu\mu}|)$ in data (10.1fb^{-1}) and illustrative signal models in three different l_{xy} ranges. The cut value is indicated by the red vertical dashed line. All selections described in Sections 3.1, 5.1, and 5.2.1 are applied, except for isolation.

344 **5.2.3 Material vertex veto**

345 A non-negligible contribution to background for this search arises from displaced “material
346 vertices”, i.e., vertices that are due to hadrons undergoing nuclear interactions in the tracker
347 material. In order to suppress such background contribution, we veto events with a DV lo-
348 cated within 0.5 mm of a pixel tracker module plane. Figure 20 shows the DV transverse (xy)
349 position distribution in data (10.1fb^{-1}), after requiring L1T selections (see Section 3.1), before
350 and after the veto is applied. Before the veto is applied, displaced material vertices are clearly
351 visible along pixel tracker modules (see also Fig. 5), while applying the veto allows to recover a
352 smoothly falling distribution as a function of l_{xy} . Figures 21 and 22 show the same DV position
353 distribution projected in the $\rho - z$ plane and along l_{xy} , respectively.

354 The effect of the material vertex veto in signal is expected to be minor, as shown in Fig. 23 for a
355 representative signal model: after requiring L1T selections (see Section 3.1), applying such veto
356 causes an overall $\sim 2\%$ loss of signal events.

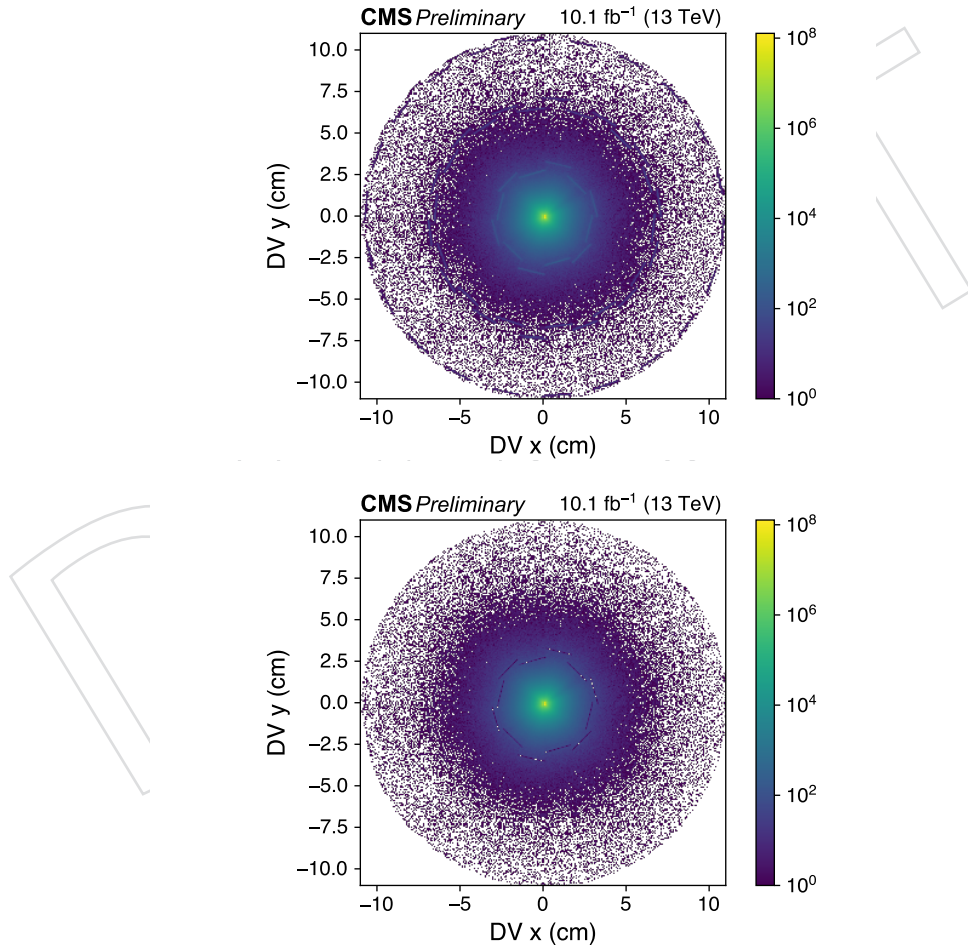


Figure 20: Distribution of DV position in the $x - y$ plane in data events (10.1fb^{-1}) passing L1T selections (see Section 3.1) before (top) and after (bottom) a pixel tracker material veto is applied.

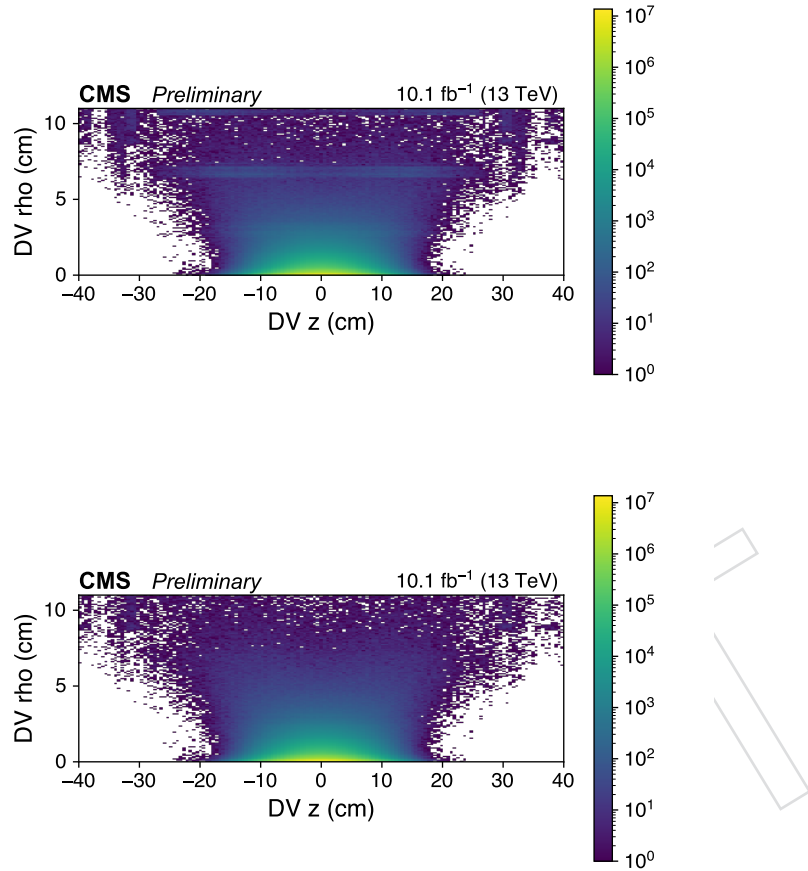


Figure 21: Distribution of DV position in the $\rho - z$ plane in data events (10.1fb^{-1}) passing L1T selections (see Section 3.1) before (top) and after (bottom) a pixel tracker material veto is applied.

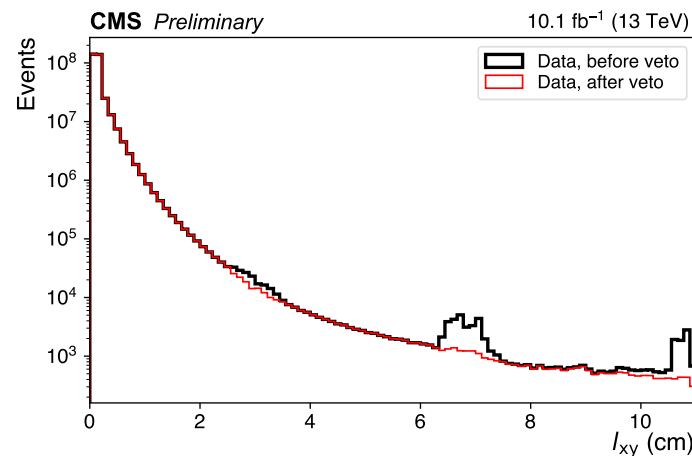


Figure 22: Distribution of l_{xy} in data events (10.1fb^{-1}) passing L1T selections (see Section 3.1) before (black) and after (red) a pixel tracker material veto is applied.

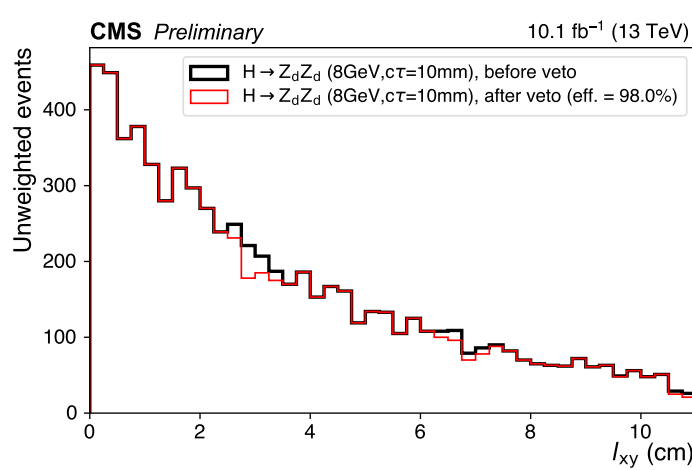


Figure 23: Distribution of l_{xy} in a representative signal model, after L1T selections are applied (see Section 3.1), before (black) and after (red) a pixel tracker material veto is applied.

357 **5.2.4 Prompt muon veto**

358 This search targets displaced signature. In order to identify truly displaced vertices, we also
 359 exploit the μ -track transverse impact parameter, d_{xy} , after d_{xy} is corrected to account for the
 360 beamspot position. However, because we target a range of displacements, we can not directly
 361 select events based on $|d_{xy}|$: selecting events based on $|d_{xy}|$ would imply a selection on l_{xy}
 362 too, and would therefore require different selection criteria as a function of the potential signal
 363 lifetime. The mutual dependency of $|d_{xy}|$ and l_{xy} is clearly shown in Fig. 24.

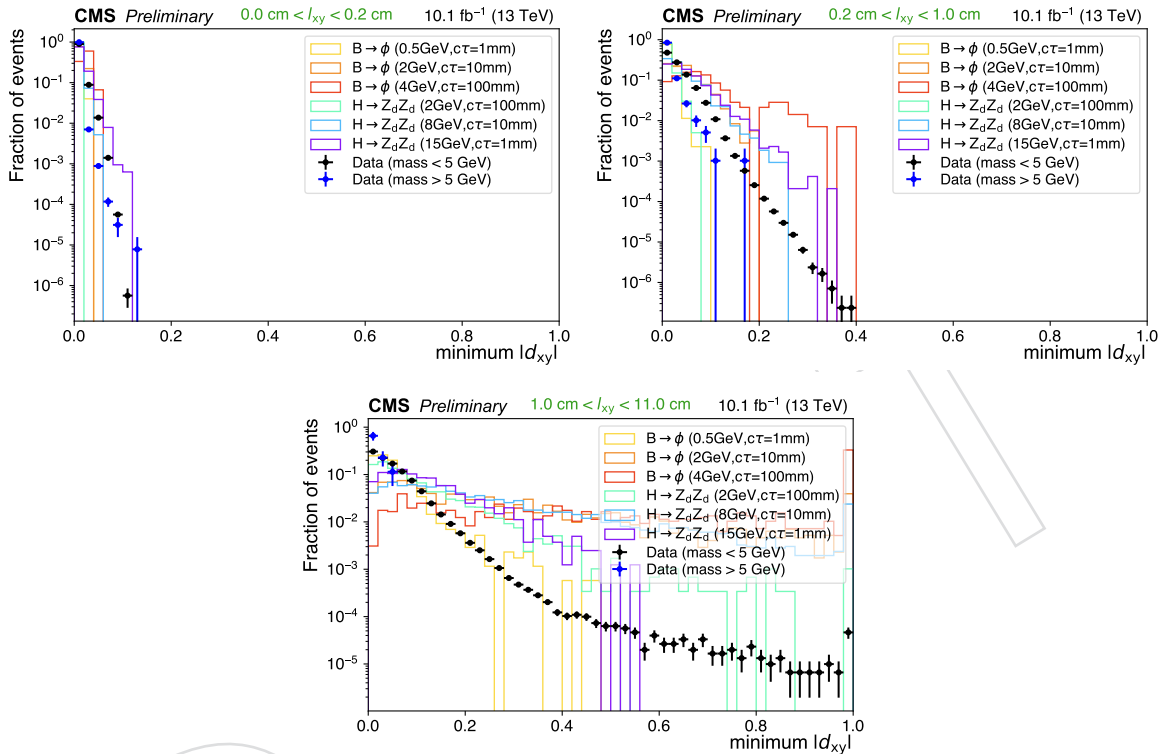


Figure 24: Distribution of the minimum $|d_{xy}|$ for the two selected muons, in data (10.1fb^{-1}) and illustrative signal models, in three different l_{xy} ranges. All selections described in Sections 3.1, 5.1, 5.2.1, 5.2.2 and 5.2.3 are applied.

364 Since selecting events directly based on d_{xy} appears to be suboptimal, we instead use two re-
 365 lated variables: the d_{xy} significance ($|d_{xy}|/\sigma_{d_{xy}}$) and the lifetime-scaled d_{xy} ($|d_{xy}|/(l_{xy}m_{\mu\mu}/p_T^{\mu\mu})$).
 366 The first normalizes d_{xy} against its measurement error, while the second normalizes d_{xy} against
 367 the lifetime corresponding to the observed DV transverse displacement. This allows for single
 368 cut values to be used for all bins of l_{xy} , giving similar signal efficiencies for all considered sig-
 369 nals models. The distributions of $|d_{xy}|/\sigma_{d_{xy}}$ and $|d_{xy}|/(l_{xy}m_{\mu\mu}/p_T^{\mu\mu})$ are shown in Fig. 25 and in
 370 Fig. 26, respectively, in data (10.1fb^{-1}) as well as in illustrative signal models, after all selections
 371 described in Sections 3.1, 5.1, 5.2.1, 5.2.2 and 5.2.3 are applied. We require each muon to satisfy:

- 372 • $|d_{xy}|/\sigma_{d_{xy}} > 2$;
- 373 • $|d_{xy}|/(l_{xy}m_{\mu\mu}/p_T^{\mu\mu}) > 0.1$.

374 **NOTE: inclusive distributions for the main selection variables are available in Appendix I.**

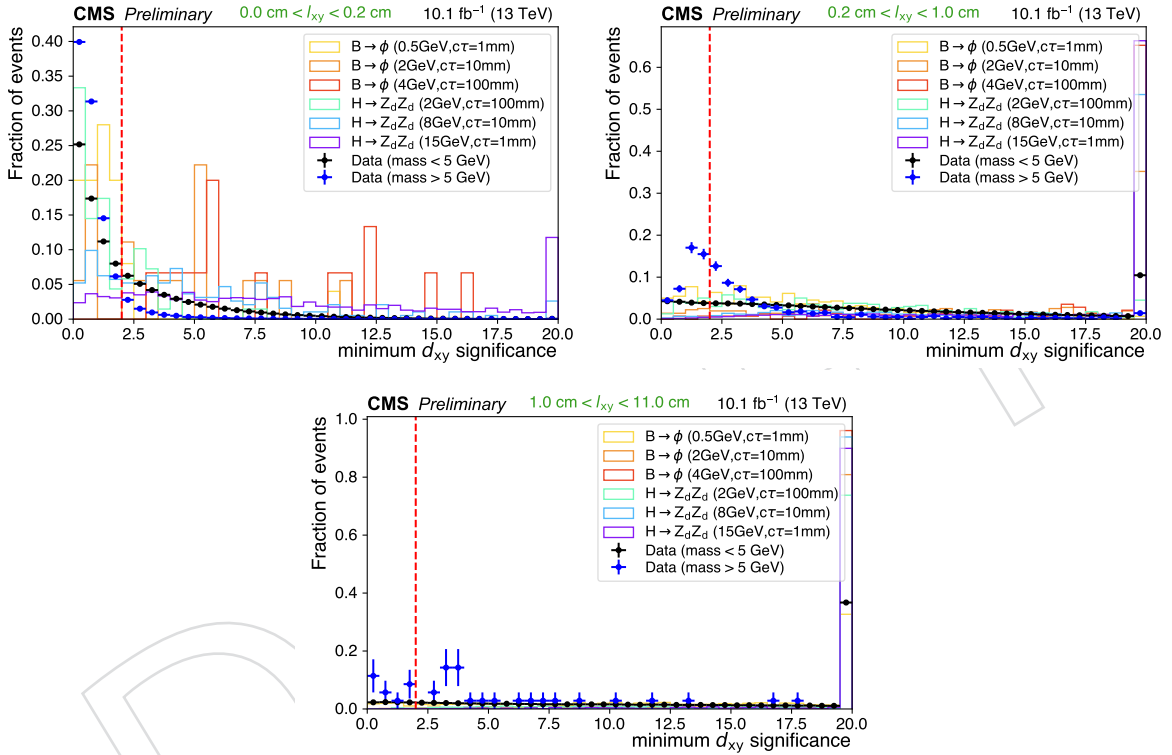


Figure 25: Distribution of $d_{xy}/\sigma_{d_{xy}}$ in data (10.1fb^{-1}) and illustrative signal models, in three different l_{xy} ranges. The cut value is indicated by the red vertical dashed line. All selections described in Sections 3.1, 5.1, 5.2.1, 5.2.2 and 5.2.3 are applied.

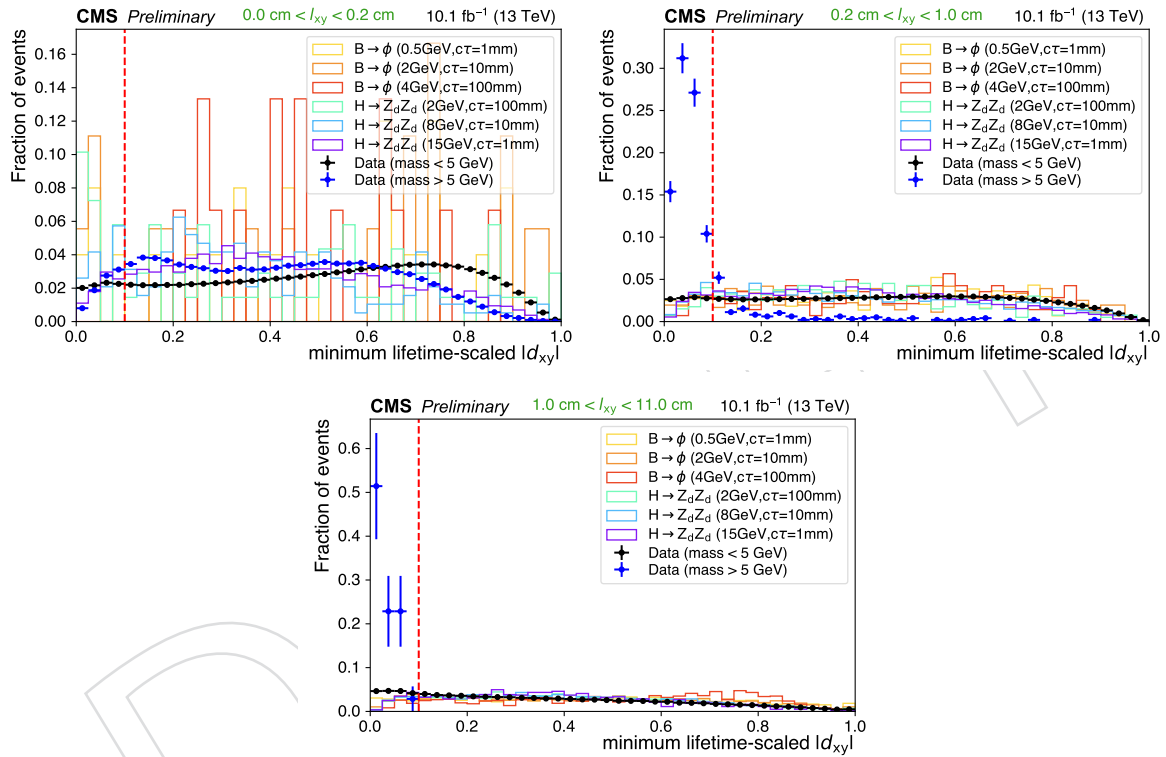


Figure 26: Distribution of $|d_{xy}| / (l_{xy} m_{\mu\mu} / p_T^{\mu\mu})$ in data (10.1 fb^{-1}) and illustrative signal models, in three different l_{xy} ranges. The cut value is indicated by the red vertical dashed line. All selections described in Sections 3.1, 5.1, 5.2.1, 5.2.2 and 5.2.3 are applied.

375 6 Trigger scale factors

376 The data and simulation samples used to determine the trigger efficiencies and scale factors
 377 for this search are listed in Table 1 and Table 2, respectively. The method relies on looking for
 378 quality dimuon pairs consistent with the J/ψ resonance in orthogonally-triggered datasets (i.e.,
 379 SingleElectron/DoubleEG/EGamma). In order to determine the dimuon pair displacement, a
 380 common vertex is fitted (via KalmanVertexFitter in CMSSW [41]) from the associated tracks.

381 For the determination of trigger efficiencies, the event-level denominator selection consists of
 382 the following requirements:

- 383 • exactly 2 OS muons from the “slimmedMuons” collection with $p_T^\mu > 3\text{ GeV}$ and
 384 $|\eta^\mu| < 2.4$ passing medium muon POG ID criteria [42];
- 385 • a good quality refitted vertex associated to the two muons (see Section 5.1.2):
 - 386 • (x, y, z) errors $< (0.05, 0.05, 0.1)\text{ cm}$;
 - 387 • $\chi^2/\text{ndof} < 5$;
 - 388 • $l_{xy} < 11\text{ cm}$;
 - 389 • material veto, as described in Section 5.2.3;
- 390 • $3.0 < m_{\mu\mu} < 3.2\text{ GeV}$.

391 The numerator further requires the trigger selections described in Section 3.1. To mitigate ef-
 392 fects from kinematic differences between the denominator dimuon pairs selected in data and
 393 in simulation, the trailing muon p_T distribution of each MC sample is reweighted to match the
 394 distribution in the appropriate sample of data.

Table 1: List of data samples used to determine the trigger efficiency.

Year	Dataset
2017	/DoubleEG/Run2017C-31Mar2018-v1/MINIAOD
	/DoubleEG/Run2017D-31Mar2018-v1/MINIAOD
	/DoubleEG/Run2017E-31Mar2018-v1/MINIAOD
	/DoubleEG/Run2017F-31Mar2018-v1/MINIAOD
	/SingleElectron/Run2017C-31Mar2018-v1/MINIAOD
	/SingleElectron/Run2017D-31Mar2018-v1/MINIAOD
	/SingleElectron/Run2017E-31Mar2018-v1/MINIAOD
	/SingleElectron/Run2017F-31Mar2018-v1/MINIAOD
2018	/EGamma/Run2018A-17Sep2018-v2/MINIAOD
	/EGamma/Run2018B-17Sep2018-v1/MINIAOD
	/EGamma/Run2018C-17Sep2018-v1/MINIAOD
	/EGamma/Run2018D-22Jan2019-v2/MINIAOD

Table 2: List of SM MC samples used to determine the trigger efficiency.

Year	Dataset
2017	/BdToJpsiKSPhi_JpsiToMuMu_BMuonFilter_DGamma0_TuneCP5_13TeV-pythia8-evtgen/ RunIIFall17MiniAODv2-PU2017_12Apr2018_94X_mc2017_realistic_v14-v1/MINIAODSIM
2018	/BdToJpsiKSPhi_JpsiToMuMu_BMuonFilter_DGamma0_TuneCP5_13TeV-pythia8-evtgen/ RunIIAutumn18MiniAOD-102X_upgrade2018_realistic_v15-v1/MINIAODSIM

395 Figure 27 shows that non-resonant contamination of the efficiency calculations (counts within
 396 bins of l_{xy} and trailing muon p_T) is at the level of 10-15%. Consequently, efficiencies calculated
 397 in the $3.0 < m_{\mu\mu} < 3.2\text{ GeV}$ window are corrected with sideband denominator and numerator
 398 counts from $2.6 < m_{\mu\mu} < 3.0\text{ GeV}$ and $3.2 < m_{\mu\mu} < 3.4\text{ GeV}$.

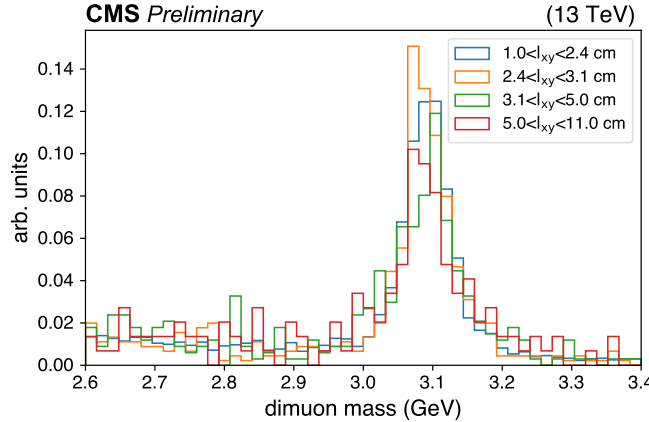


Figure 27: Normalized mass distributions with the denominator selection and a wider mass window of $2.6 < m_{\mu\mu} < 3.4$ GeV, in ranges of l_{xy} .

399 Figures 28, 29, 30, 31, and 32 show the trigger efficiencies in data and MC samples, as well as
 400 their ratios (i.e., data/MC scale factors), as a function of trailing muon p_T , reconstructed l_{xy} ,
 401 dimuon η , $\Delta R(\mu, \mu)$, and minimum impact parameter magnitude of the two muons, respec-
 402 tively. The l_{xy} binning corresponds to that used for the nominal analysis strategy, except that
 403 the three highest l_{xy} bins have been merged to help reduce statistical uncertainty (after ver-
 404 ifying their scale factors were consistent with each other within statistics). As a function of
 405 trailing muon p_T , the scale factors are observed to be consistent between both years (2017 and
 406 2018) and consistent with unity within approximately 6%. As a function of l_{xy} , at high values of
 407 l_{xy} , the scale factors have large statistical uncertainty, but are still consistent between the years
 408 and with unity.

409 For final determination of scale factors, samples are combined across years to further reduce
 410 the statistical uncertainty. Consequently, the strategy we adopt for application of trigger scale
 411 factors is as follows:

- 412 • for events with $l_{xy} < 1.0$ cm, the event-level trigger scale factor is a function of the
 413 trailing muon p_T and l_{xy} , and the uncertainty is the statistical uncertainty added in
 414 quadrature with the difference from unity.
- 415 • for events with $l_{xy} > 1.0$ cm, the event-level trigger scale factor is only a function of
 416 l_{xy} , and the uncertainty is determined as for $l_{xy} < 1.0$ cm, with the central values of
 417 the scale factors being set to 1.

418 Following this prescription, the trigger scale factors are summarized in Figure 33.

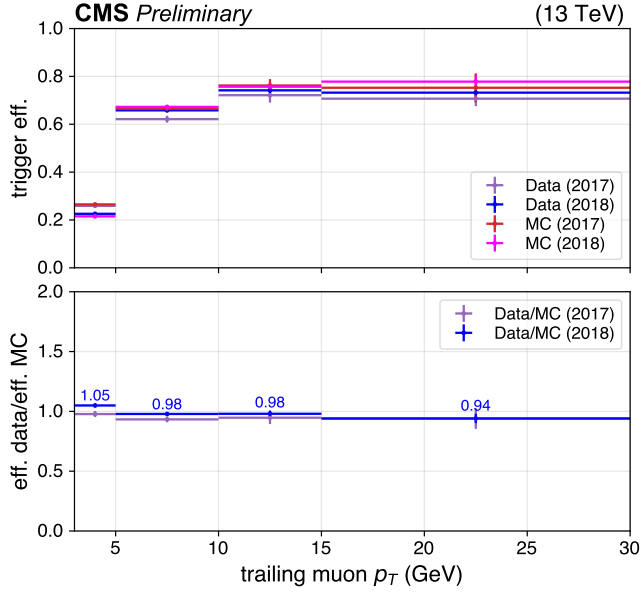


Figure 28: Trigger efficiencies in data and MC samples (upper panel) and corresponding data/MC scale factors (lower panel) as a function of the trailing muon p_T .

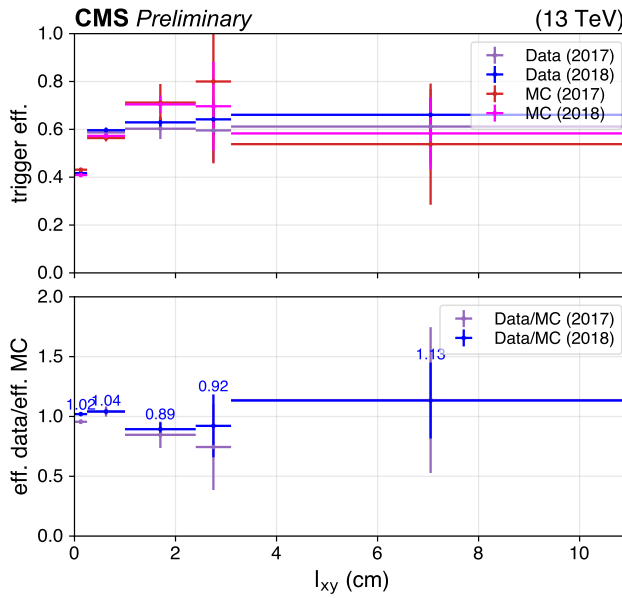


Figure 29: Trigger efficiencies in data and MC samples (upper panel) and corresponding data/MC scale factors (lower panel) as a function of the reconstructed l_{xy} .

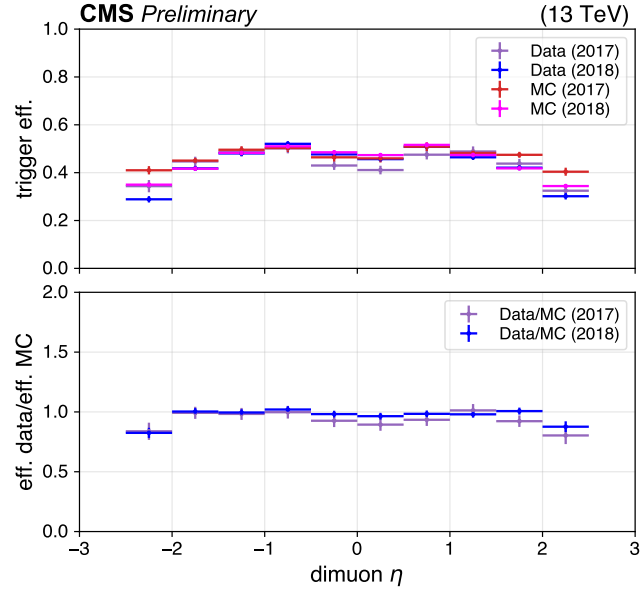


Figure 30: Trigger efficiencies in data and MC samples (upper panel) and corresponding data/MC scale factors (lower panel) as a function of the dimuon system η .

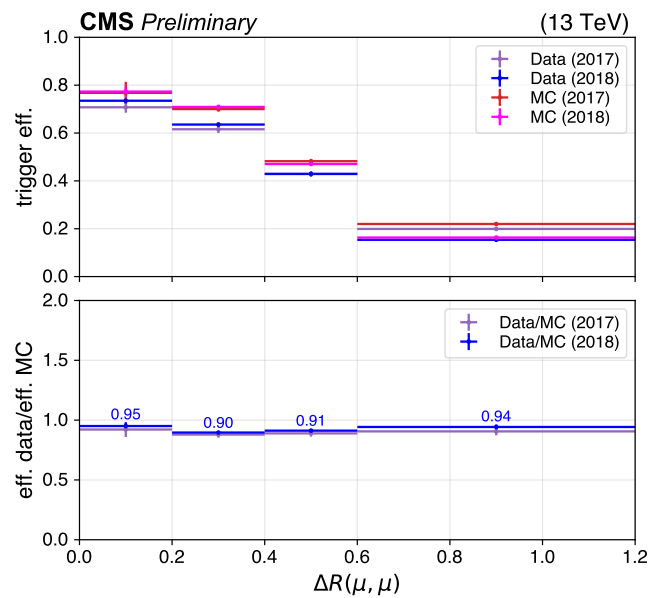


Figure 31: Trigger efficiencies in data and MC samples (upper panel) and corresponding data/MC scale factors (lower panel) as a function of the $\Delta R(\mu, \mu)$.

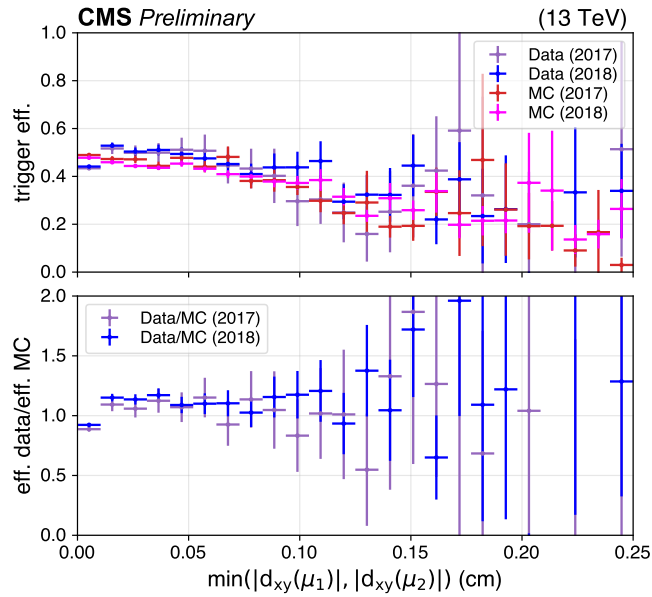
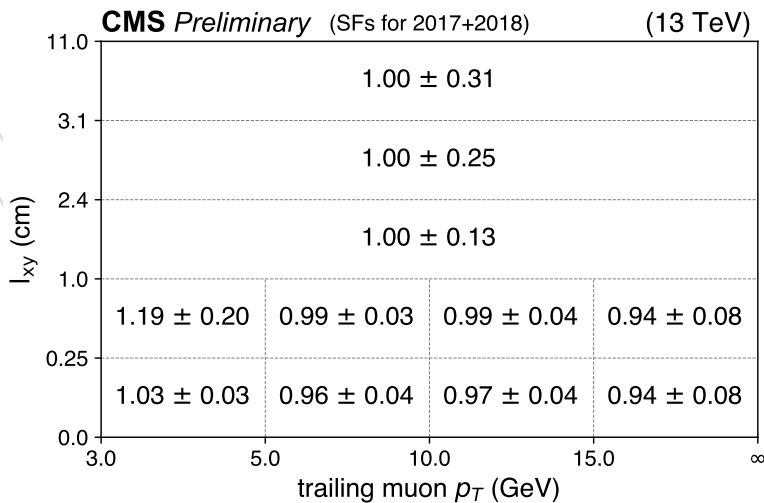


Figure 32: Trigger efficiencies in data and MC samples (upper panel) and corresponding data/MC scale factors (lower panel) as a function of the minimum absolute value of the transverse impact parameters of the two muons.



419 7 Signal lifetime reweighting

420 A fixed grid of $(m_{\phi/Z_D}, c\tau_0^{\phi/Z_D})$ (in the following: $(m, c\tau_0)$) signal points for each model is
 421 generated. Then, we perform a lifetime-based reweighting as well as a parametrization of
 422 the signal resonance width as a function of its mass. Finally, in order to determine the signal
 423 acceptance in a finer $(m, c\tau_0)$ grid, a two-dimensional interpolation method is used that com-
 424 bines the previous procedures, in bins of l_{xy} , as described in Appendix D. In the following, the
 425 lifetime-based reweighting procedure is described in detail.

426 The reweighting factor $w(t)$ as defined in Equation 1 is used to get a sample with lifetime $c\tau_1$
 427 from a generated sample of lifetime τ_0 :

$$w(t) = \frac{c\tau_0}{c\tau_1} e^{(\frac{ct}{c\tau_0} - \frac{ct}{c\tau_1})} \quad (1)$$

428 In Equation 1, ct is the generator-level event lifetime defined in Equation 2:

$$ct = c(\vec{l}_{xy} \cdot \vec{p}_T) \frac{m}{p_T^2} \quad (2)$$

429 The $w(t)$ factor is defined as a multiplicative factor: if more than a long-lived particle de-
 430 caying into a pair of muons is found in the event, the event-level weight results from the
 431 multiplication of the corresponding $w(t)$ factors.

432 However, in order to allow for simpler interpretation (and reinterpretation) of the results,
 433 only signal events with a single long-lived particle decaying into a pair of muons are selected
 434 at generator-level, for all signal models used in this search.

435 We reweight a sample of higher lifetime to lower lifetime, in order to ensure that the full recon-
 436 structed displacement span is covered. In fact, reweighting lower lifetime samples to higher
 437 lifetime may suffer from lack of statistics at large reconstructed displacement.

438 Figures 34-36 aims at validating the lifetime reweighting procedure in use, showing that the l_{xy}
 439 distribution of reweighted samples is in agreement with that of samples generated using the
 440 target lifetime. The $H \rightarrow Z_D Z_D$ signal model is shown in Figs. 34-36; results are fully consistent
 441 for other models under study.

442 If any disagreement larger than statistical uncertainty is found, it is accounted for as a system-
 443 atic uncertainty.

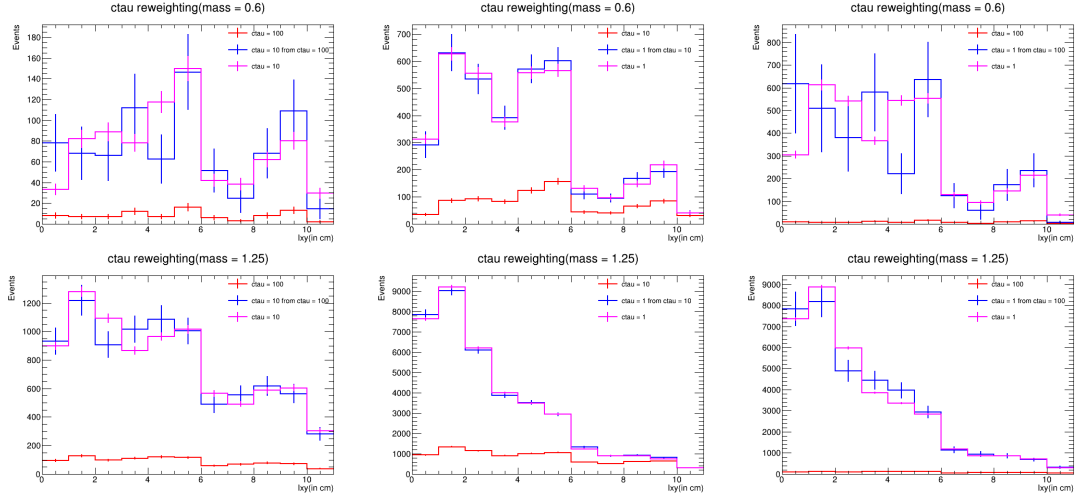


Figure 34: Lifetime reweighting for representative $H \rightarrow Z_D Z_D$ signal models with (upper) $m_{Z_D} = 0.6 \text{ GeV}$ and (lower) $m_{Z_D} = 1.25 \text{ GeV}$.

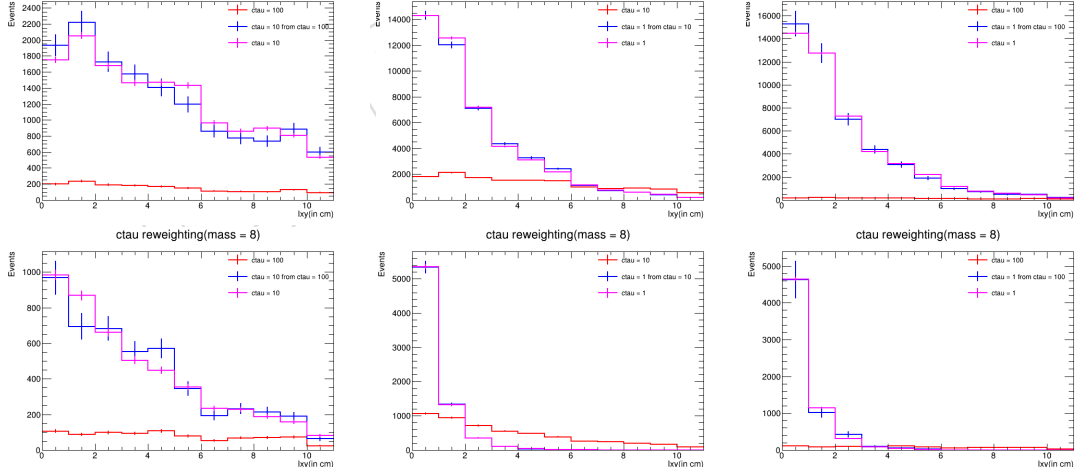


Figure 35: Lifetime reweighting for representative $H \rightarrow Z_D Z_D$ signal models with (upper) $m_{Z_D} = 2.0 \text{ GeV}$ and (lower) $m_{Z_D} = 8.0 \text{ GeV}$.

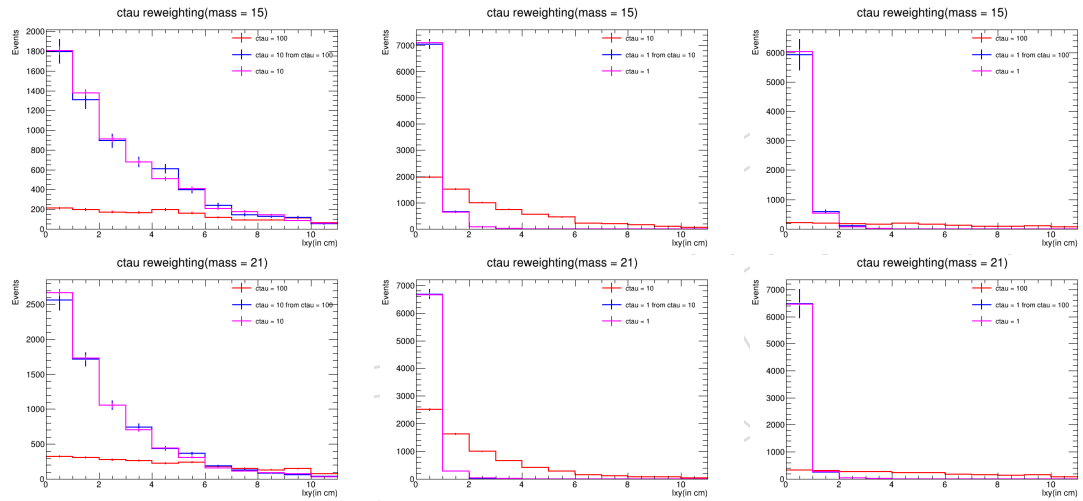


Figure 36: Lifetime reweighting for representative $H \rightarrow Z_D Z_D$ signal models with (upper) $m_{Z_D} = 15.0 \text{ GeV}$ and (lower) $m_{Z_D} = 21.0 \text{ GeV}$.

444 8 Parametrization of the signal resonance width

445 A fixed grid of $(m_{\phi/Z_D}, c\tau_0^{\phi/Z_D})$ (in the following: $(m, c\tau_0)$) signal points for each model is
 446 generated. Then, we perform a lifetime-based reweighting as well as a parametrization of the
 447 signal resonance width as a function of its mass. Finally, in order to determine the signal accep-
 448 tance in a finer $(m, c\tau_0)$ grid, a two-dimensional interpolation method is used that combines
 449 the previous procedures, in bins of l_{xy} , as described in Appendix D. In the following, the pro-
 450 cedure used to parametrize the signal resonance width as a function of its mass is described in
 451 detail.

452 We use a probability density function resulting from the sum of a double Crystal Ball and a
 453 Gaussian function in order to fit the signal dimuon mass distribution, freezing all parameters
 454 but mean and σ . The fits are performed separately for each signal mass and lifetime hypothesis.
 455 Representative examples are shown in Figs. 37-38 and Figs. 39-40, for $B \rightarrow \phi X$ and $H \rightarrow Z_D Z_D$
 456 signal models respectively.

457 The resulting relative resonance σ is shown as a function of the mean mass in Fig.41, for dif-
 458 ferent $(m, c\tau)$ hypotheses, and is found to be consistent with a constant value of 0.011, with
 459 negligible variations as a function of the lifetime. A systematic uncertainty is assessed in order
 460 to cover for such variations.

461 We note that an alternative choice for the probability density function is also evaluated, as
 462 summarized in Appendix C.

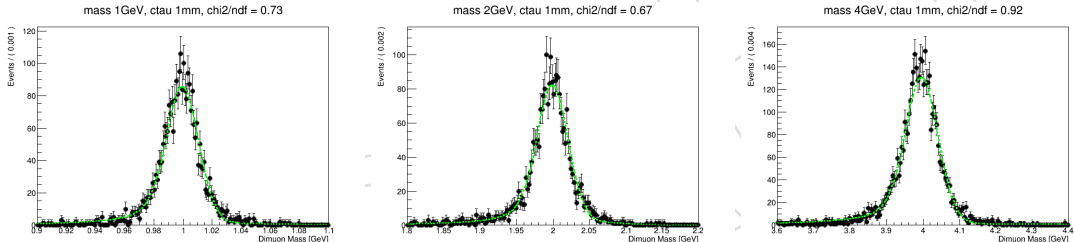


Figure 37: Fit of signal mass distribution for representative $B \rightarrow \phi X$ signal mass hypotheses and $c\tau_0 = 1$ mm. The χ^2/ndof of each fit is also shown.

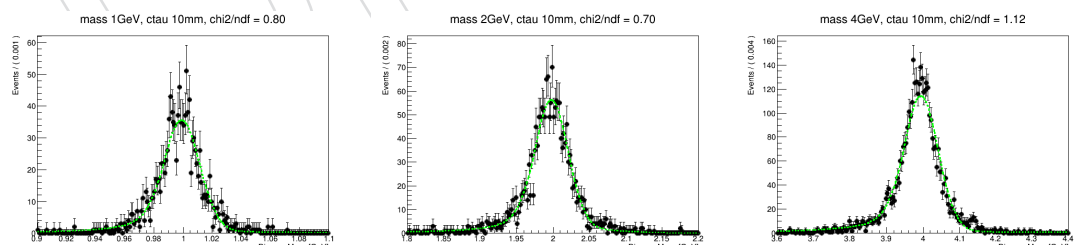


Figure 38: Fit of signal mass distribution for representative $B \rightarrow \phi X$ signal mass hypotheses and $c\tau_0 = 10$ mm. The χ^2/ndof of each fit is also shown.

463 8.0.1 Dependency of signal resonance width on l_{xy}

464 The potential dependency of the signal resonance width on l_{xy} is evaluated. Figure 42 shows
 465 the relative resonance width for $B \rightarrow \phi X$ and $H \rightarrow Z_D Z_D$ representative signal models in dif-
 466 ferent l_{xy} ranges. A slight dependency is found, where the relative resonance width tends to
 467 increase at larger l_{xy} , and a systematic uncertainty is assessed in order to cover for the assump-
 468 tion of a constant width.

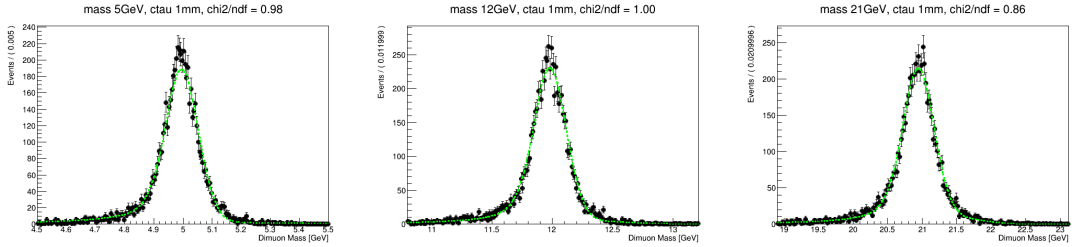


Figure 39: Fit of signal mass distribution for representative $H \rightarrow Z_D Z_D$ signal mass hypotheses and $c\tau_0 = 1 \text{ mm}$. The χ^2/ndof of each fit is also shown.

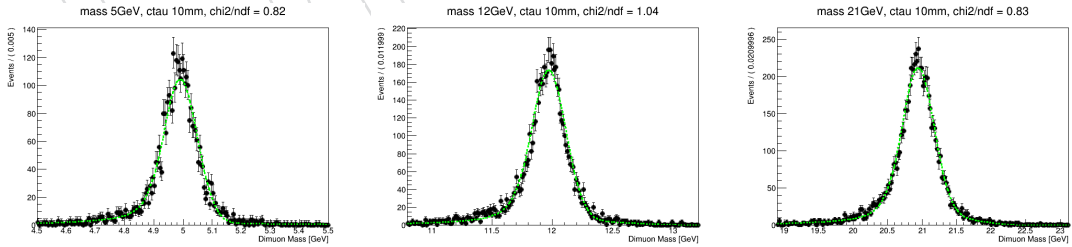


Figure 40: Fit of signal mass distribution for representative $H \rightarrow Z_D Z_D$ signal mass hypotheses and $c\tau_0 = 10 \text{ mm}$. The χ^2/ndof of each fit is also shown.

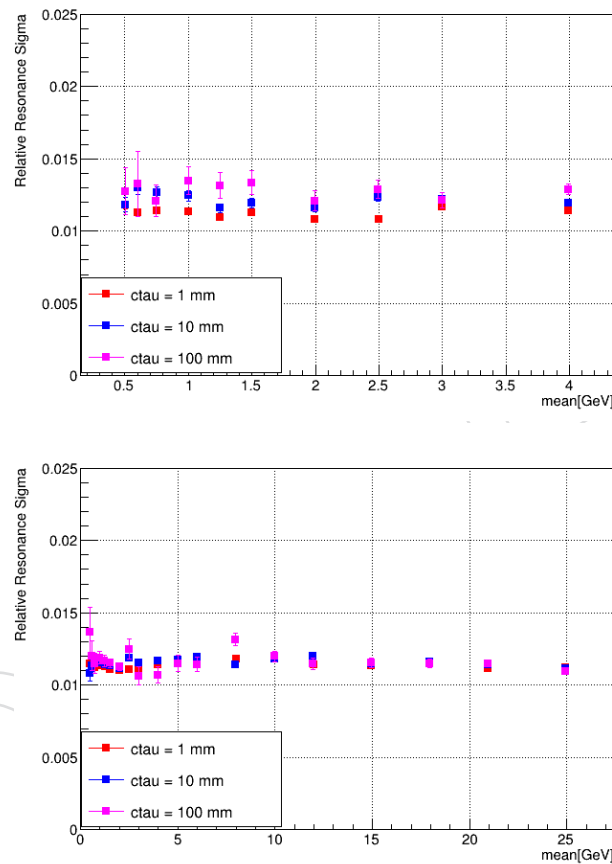


Figure 41: Relative resonance width (σ) as a function of the mean mass (as determined from a fit of the signal dimuon mass distribution), for (upper) $B \rightarrow \phi X$ and (lower) $H \rightarrow Z_D Z_D$ signal models.

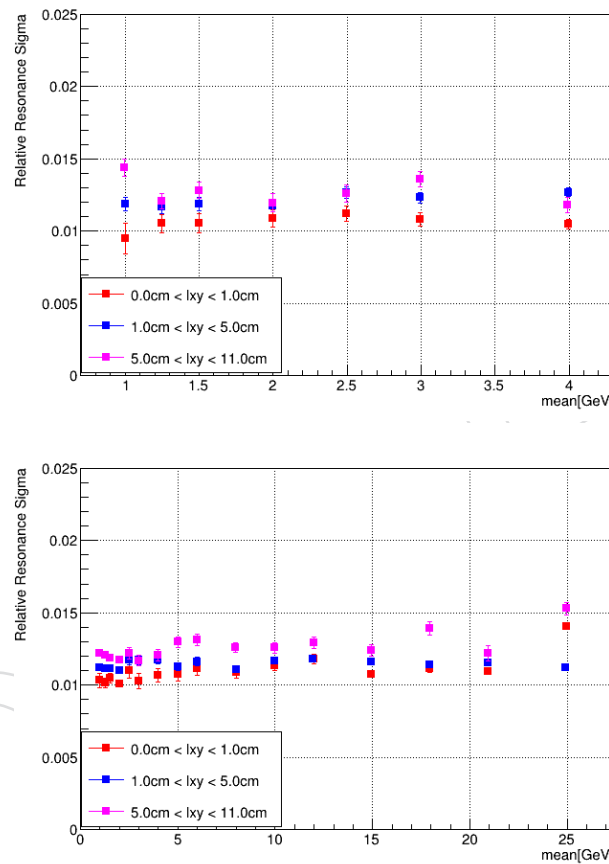


Figure 42: Relative resonance width as a function of the mean mass (as determined from a fit of the signal dimuon mass distribution), in different l_{xy} ranges, for (upper) $B \rightarrow \phi X$ ($c\tau = 10$ mm) and (lower) $H \rightarrow Z_D Z_D$ ($c\tau = 10$ mm) signal models.

469 9 Background estimation in dimuon mass windows

470 For a given signal mass hypothesis, we perform shape analysis in bins of (l_{xy} , $p_T^{\mu\mu}$, isolation),
 471 as described in Section 4. In bins with low statistics, we use counting experiments for cross-
 472 validation.

473 For the shape analysis, we parametrize the background in a mass window of $\pm 5\sigma$ around the
 474 signal mass hypothesis, using a polynomial functional form as probability density function. In
 475 the case of counting experiments, we define a signal mass window of $\pm 2\sigma$ around the signal
 476 mass hypothesis, and use sidebands ($[-5\sigma, -2\sigma] + [+2\sigma, +5\sigma]$) to estimate the background in
 477 the signal window itself.

478 We perform a shape analysis in all bins regardless of number of data events in sidebands.
 479 Counting experiments are performed as a cross-check only in the case where the number of
 480 data events in sidebands is < 20 . The choice of such threshold (i.e., < 20 or ≥ 20 events in
 481 sidebands) is justified in Appendix E.

482 The full mass window ($\pm 5\sigma$ around the signal mass hypothesis) is required to not overlap
 483 with any of the known (SM) resonances, as well as with potential “fake” dimuon resonances
 484 where pions are wrongly identified as muons (e.g., K_S). To this purpose, we define a number
 485 of “masked” regions, based on the position and the width of such resonances, as detailed in
 486 Appendix F.

487 The dimuon mass distribution within each mass window is treated as binned. The number of
 488 bins in the $\pm 5\sigma$ window around the signal mass hypothesis is set to be constant and equal to
 489 100: while such binning is not really relevant in the context of this search, a large number of bins
 490 (such as 100) in the case of a dimuon mass fit allows to use a binned approach while limiting
 491 the loss of precision with respect to an unbinned likelihood fit. If statistics is particularly low
 492 in a (l_{xy} , $p_T^{\mu\mu}$, isolation) search bin, then a counting experiment is performed instead of a fit.

493 For each of the search bins where a shape analysis or a counting experiment is performed, as
 494 well as for the combination of all bins, we perform bias tests using toy data sets after injecting
 495 signals of strength $r = 2$ and $r = 5$. For bins where a shape analysis is performed, we also
 496 perform goodness-of-fit (GOF) tests. All of the tests are described in detail in Appendix G, and
 497 results are found to be satisfactory.

498 **499 500 For analysis R&D, using only 10.1fb^{-1} of data (roughly equal to 10% of the full scouting
 data set), the background is estimated inclusively in $p_T^{\mu\mu}$ and isolation, to compensate for
 the lack of statistics.**

501 9.1 Shape analysis: fit of the dimuon mass spectrum

502 For the shape analysis, we use a polynomial functional form to parametrize the background
 503 dimuon mass spectrum in windows of $\pm 5\sigma$ around the signal mass hypothesis.

504 Different polynomial functional forms have been tested, including simple polynomials, Bern-
 505 stein polynomials, and Chebyshev polynomials. Bernstein and Chebyshev polynomials have
 506 been found to be stable across all of the search bins. In fact, polynomial functional forms are
 507 expected to be equivalent to each other, except for potential numerical instabilities (see Ap-
 508 pendix H). Therefore, in the following we use Bernstein polynomials as a default choice.

509 The order of the polynomial in each search bin is selected by means of a Fisher test [43], in
 510 the following referred to as “F-test”. In particular, the order is increased till the F-test com-
 511 paring a polynomial of order “N+1” to one of order “N” for the fit to data shows no signif-

512 icant improvement, and the function of order “N” is retained. First, the lowest order poly-
 513 nomial is used to fit the data. Then, the next-order polynomial is used, and the difference
 514 $2\Delta NLL_{N+1} = 2(NLL_{N+1} - NLL_N)$ is evaluated to determine whether the data support the
 515 hypothesis of the higher order function. This is quantitatively expressed based on the fact that
 516 $2\Delta NLL_{N+1}$ should be distributed as a χ^2 with M degrees of freedom, where M is the difference
 517 in the number of free parameters in the $(N + 1)^{\text{th}}$ order function and the N^{th} order function: for
 518 polynomials, $M = 1$. A p -value is then calculated as $p(2\Delta NLL > 2\Delta NLL_{N+1} | \chi^2(M))$. If the
 519 p -value is less than 0.05, the higher order function is retained, since it is determined to signifi-
 520 cantly improve the description of the data. Once the maximum order “N” has been determined,
 521 we use the best order “N” polynomial alongwith orders “N-1” and “N+1” as list of suitable
 522 functions for “discrete profiling” method [44] where the choice of the background function is
 523 treated as a discrete nuisance parameter in the fit, to account for the uncertainty associated with
 524 the arbitrary choice of the function. We use an additional goodness-of-fit (GOF) constraint to
 525 remove the polynomials that may not describe the data appropriately. A goodness-of-fit (GOF)
 526 test is performed using a χ^2 test statistic, then converted into a p -value, where the number
 527 of degrees of freedom is taken to be equal to the difference between number of bins in the fit
 528 window (i.e., 100) and number of fit parameters (except for the normalization term): a total
 529 of 500 toy data sets are generated each time, and the fraction of toys where the test statistic is
 530 larger than the one obtained for the fit to the data is computed. A polynomial of a given order
 531 is removed from the list of suitable functions if the corresponding p -value is found to be less
 532 than 0.01.

533 The procedure described above reflects the one adopted in Ref. [45].

534 A number of representative background fits to data (10.1fb^{-1}) are collected in Figs. 44-50. All
 535 of the fits to data (10.1fb^{-1}) are available in Ref. [46].

536 9.2 Counting experiments

537 In bins where the number of events in sidebands is less than 20, counting experiments are
 538 performed for cross-validation.

539 The background in the signal mass window ($\pm 2\sigma$ around the signal mass hypothesis) is esti-
 540 mated from the sidebands, by means of a transfer factor. Supported by the low statistics regime,
 541 we assume that the background is linear across the full mass window ($\pm 5\sigma$ around the signal
 542 mass hypothesis), and determine the trasnfer factor to reflect the size of sidebands and signal
 543 window:

$$R = \frac{4\sigma}{10\sigma - 4\sigma} = \frac{2}{3}. \quad (3)$$

544 In order to cover for the assumption of linearity of the background, we assess a systematic un-
 545 certainty on R equal to 50%. The potential signal contamination of the sidebands is accounted
 546 for: if signal is found in the sidebands, the signal yield in the signal mass window is reduced
 547 accordingly:

$$S'(\text{signal window}) = S(\text{signal window}) - R S(\text{sidebands}), \quad (4)$$

548 where R is defined in Equation 3.

549 An example of counting experiment search bin is shown in Fig. 43.

Counting Experiment Illustration

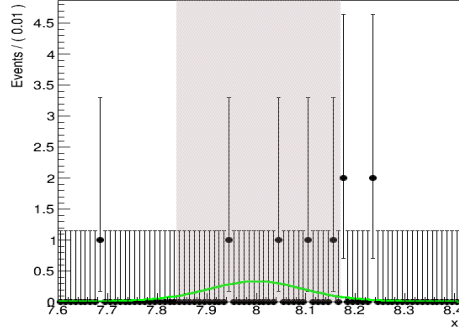


Figure 43: Example of a counting experiment search bin, using 10.1fb^{-1} of data. The green line illustrates the expected dimuon mass distribution for a potential BSM signal.

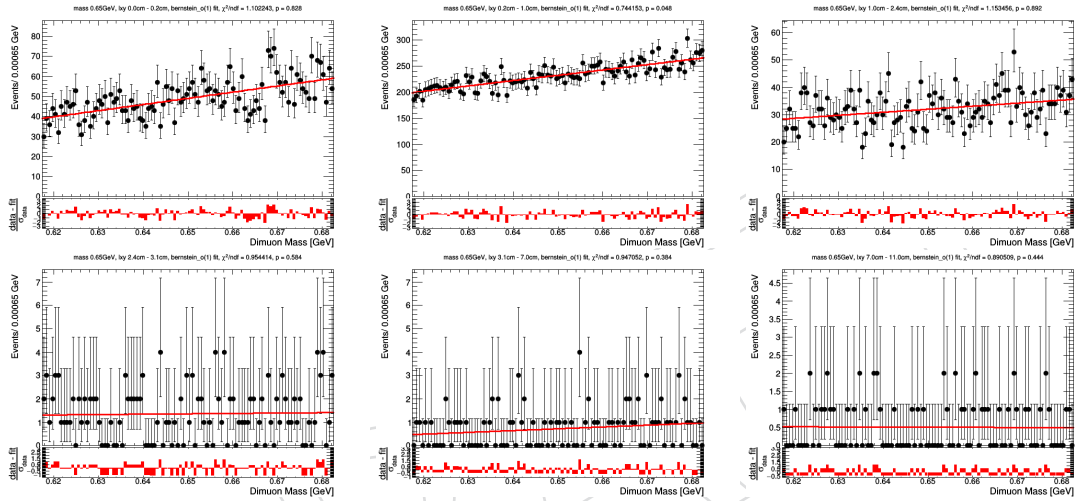


Figure 44: Background fits to data (10.1fb^{-1}) for a signal mass hypothesis of 0.65 GeV . Pulls are shown in the lower panel.

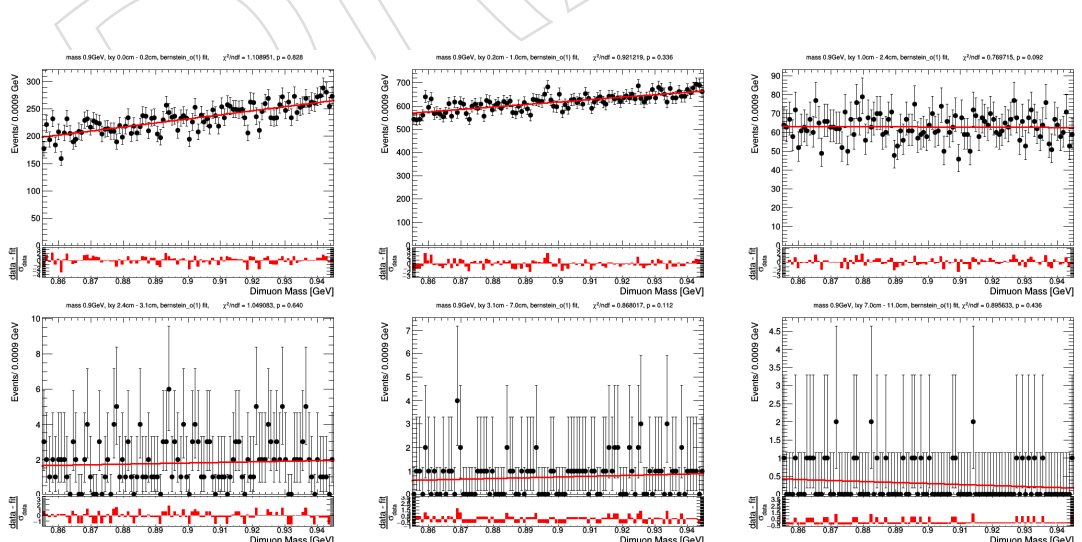


Figure 45: Background fits to data (10.1fb^{-1}) for a signal mass hypothesis of 0.9 GeV . Pulls are shown in the lower panel.

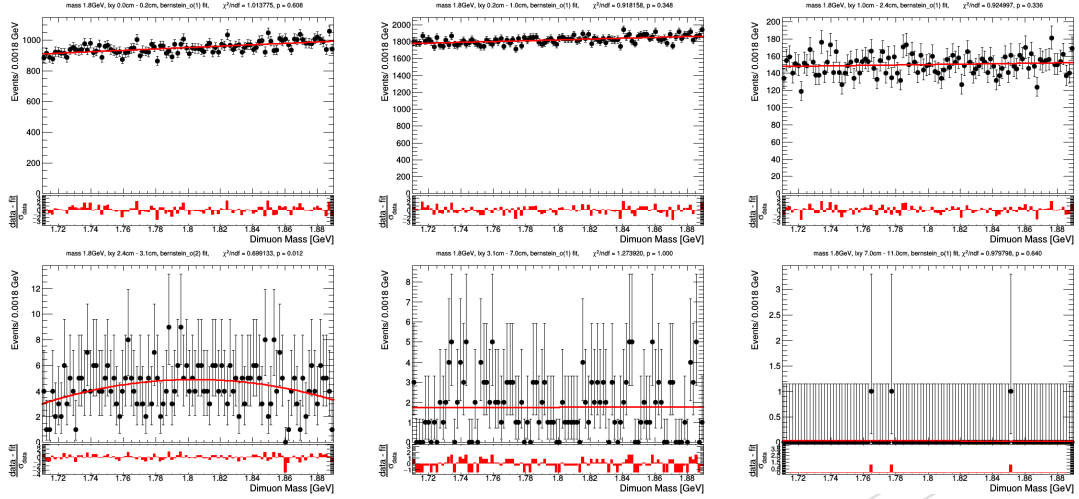


Figure 46: Background fits to data (10.1fb^{-1}) for a signal mass hypothesis of 1.8 GeV . Pulls are shown in the lower panel.

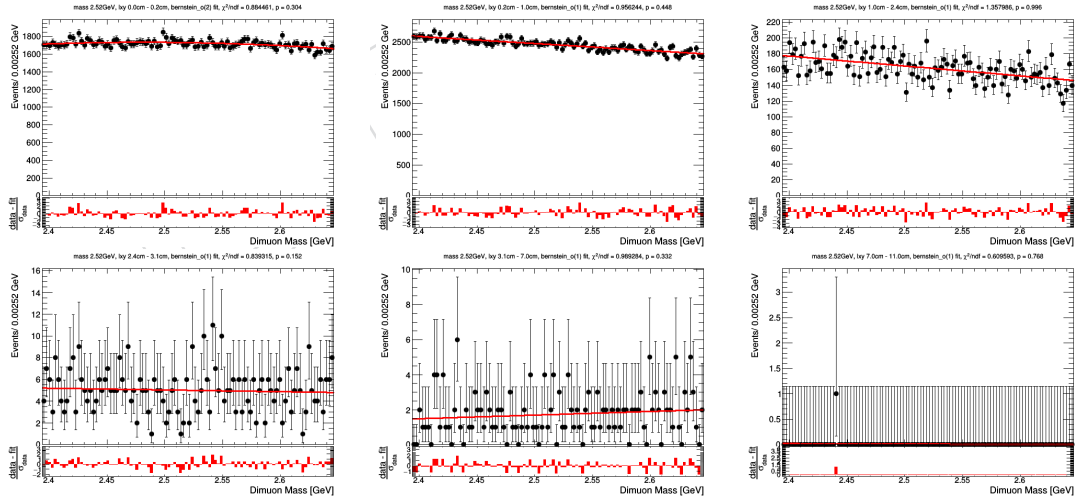


Figure 47: Background fits to data (10.1fb^{-1}) for a signal mass hypothesis of 2.52 GeV . Pulls are shown in the lower panel.

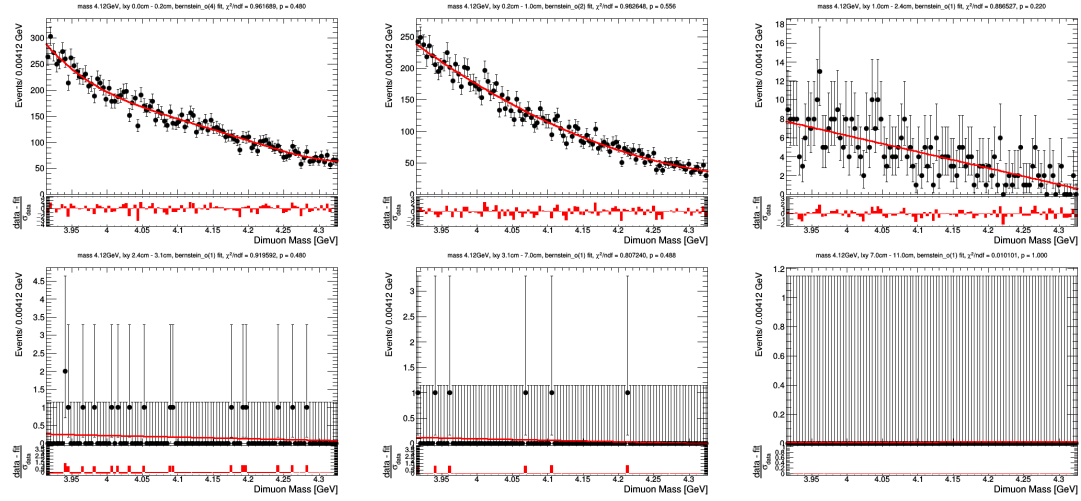


Figure 48: Background fits to data (10.1fb^{-1}) for a signal mass hypothesis of 4.12 GeV . Pulls are shown in the lower panel.

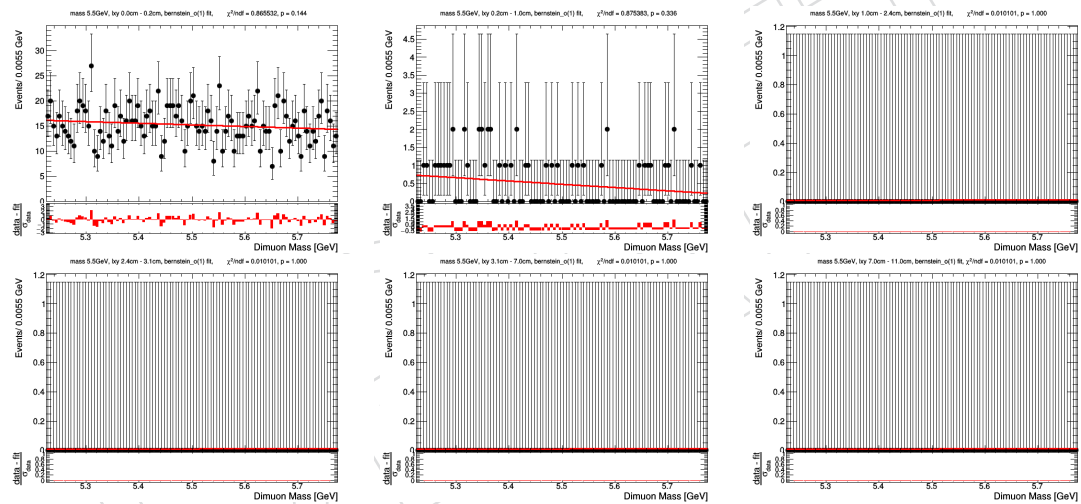


Figure 49: Background fits to data (10.1fb^{-1}) for a signal mass hypothesis of 5.5 GeV . Pulls are shown in the lower panel.

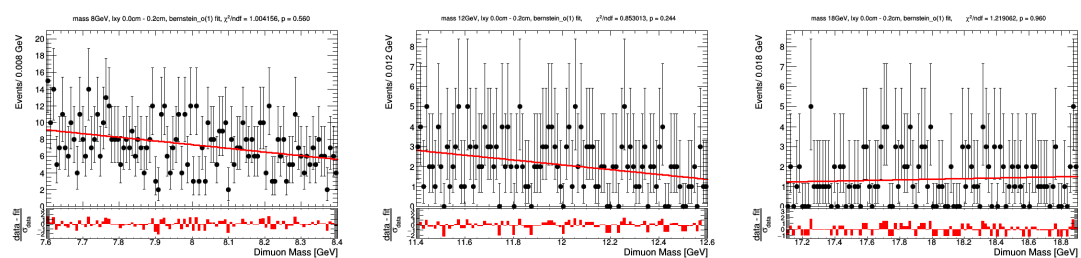


Figure 50: Background fits to data (10.1fb^{-1}) for a signal mass hypothesis of (left) 8.0 GeV and (right) 12.0 GeV . Pulls are shown in the lower panel.

550 10 Results and interpretation

551 As a proof of principle experiment, in the attempt to demonstrate the achievable search sen-
552 sitivity, we apply the full search strategy and selection using known resonances as “standard
553 candles”. This is described in Appendix A.

554 In the following, we use the full search results (**using 10.1fb^{-1} of data**) in order to constrain
555 models of BSM physics.

556 Maximum likelihood fits to the data are carried out simultaneously in all search bins, under
557 either background-only or background+signal hypotheses. The uncertainties in the modeling
558 of the background, described in Section 9, are inputs to the fitting procedure. For search bins
559 where a counting experiment is performed, the likelihoods are constructed as the product of
560 Poisson probability density functions, one for each search bin. For search bins where a shape
561 analysis is performed, the shapes obtained in each search bin, as described in Section 9 for back-
562 ground and in Section 8 for signal, are directly used as input likelihoods to the simultaneous
563 fits to data. Additional log-normal constraint terms are used to account for the uncertainties in
564 the background estimate and, if considered, in the signal yields (see Section 10.1). The back-
565 ground+signal fits are used to set 95% confidence level (CL) upper limits on the branching
566 ratios for the signal models under consideration. Limits are set using a modified frequentist
567 approach, employing the CL_s criterion and relying on asymptotic approximations to calculate
568 the distribution of the profile likelihood test-statistic used [47–50]. These limits are then used, in
569 conjunction with the theoretical cross section calculations, to exclude ranges of masses and/or
570 lifetimes for the BSM particles of the signal models.

571 10.1 Systematic uncertainties in the signal yields

572 In order to account for potential mismodeling of the simulation, a systematic uncertainty is
573 assessed in the signal yields equal to $1 - \epsilon_{\text{selection}}$, where $\epsilon_{\text{selection}}$ is defined as the total selection
574 efficiency (see Section 5) on top of the trigger selections (see Section 3.1). The selection cut-flow
575 efficiencies are listed in Appendix J for few representative signal models: the total selection
576 efficiency on top of the trigger selections typically ranges from about 55% to about 75%, thus
577 resulting in a systematic uncertainty ranging between 25% and 45%, depending on the signal
578 model as well as on the search bin.

579 As for the trigger selections, we consider a systematic uncertainty in the trigger scale factor
580 which equals the sum in quadrature of statistical uncertainty and difference of the scale factor
581 itself from unity, as described in Section 6.

582 Additionally, we assess a systematic uncertainty arising from the uncertainty in the luminosity
583 measurement, amounting to 2.3% for 2017 and to 2.5% for 2018 [51, 52].

584 Finally, we account for the limited size of the simulated signal samples.

585 Uncertainties arising from the choice of the PDF and of the renormalization (μ_R) and factoriza-
586 tion (μ_F) scales used in the event generator are negligible compared to others.

587 Uncertainties in the luminosity measurement and trigger scale factors are treated as correlated
588 across search bins. Other uncertainties are taken as uncorrelated. Because there is no signif-
589 icant difference between 2017 and 2018 data and simulations, all uncertainties are treated as
590 correlated across data taking periods.

591 10.2 Constraints on models of BSM physics

592 As a result of an **end-to-end search performed on about 10% of the full data set, correspond-**
593 **ing to an integrated luminosity of 10.1 fb^{-1} , we set upper limits at 95% CL on the branching**
594 **ratios for the $B \rightarrow \phi X$ and $H \rightarrow Z_D Z_D$ signal models.** Figure 51 and Fig. 52 show the up-
595 **per limits as a function of the signal mass hypothesis for a number of representative lifetime**
596 **hypotheses, for the $B \rightarrow \phi X$ and $H \rightarrow Z_D Z_D$ signal models, respectively.** On the contrary,
597 **Fig. 53 shows the upper limits as a function of $c\tau_0^{Z_D}$ for a number of representative signal mass**
598 **hypotheses, for the $H \rightarrow Z_D Z_D$ signal model.**

599 Constraints tend to be less stringent at lower signal mass and at larger lifetime. On the one
600 hand, at large lifetimes it is more likely that BSM long-lived particles decay beyond the CMS
601 pixel tracker (i.e., outside of our acceptance). On the other hand, while at large masses (es-
602 pecially in search bins with non-zero displacement) we are able to suppress the background
603 almost completely, this is not the case at very low masses ($m_{\mu\mu} \lesssim 5 \text{ GeV}$).



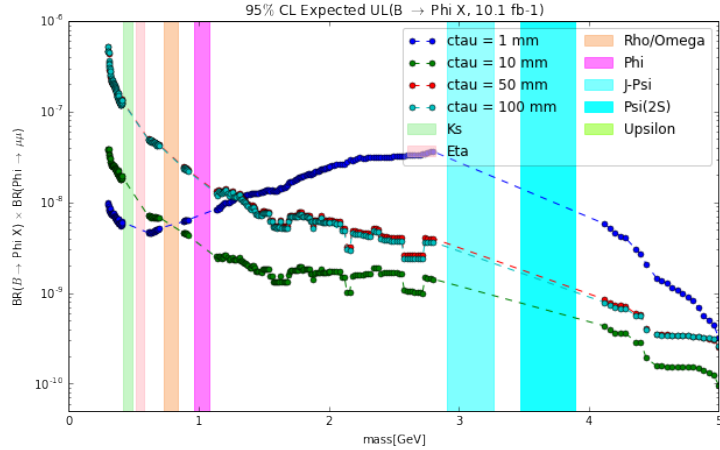


Figure 51: Exclusion limits at 95% CL on the branching ratio ($\text{BR}(B \rightarrow \phi X) \times \text{BR}(\phi \rightarrow \mu\mu)$) as a function of the signal mass (m_ϕ) hypothesis for a number of representative lifetime ($c\tau_0^\phi$) hypotheses, for the $B \rightarrow \phi X$ signal model.

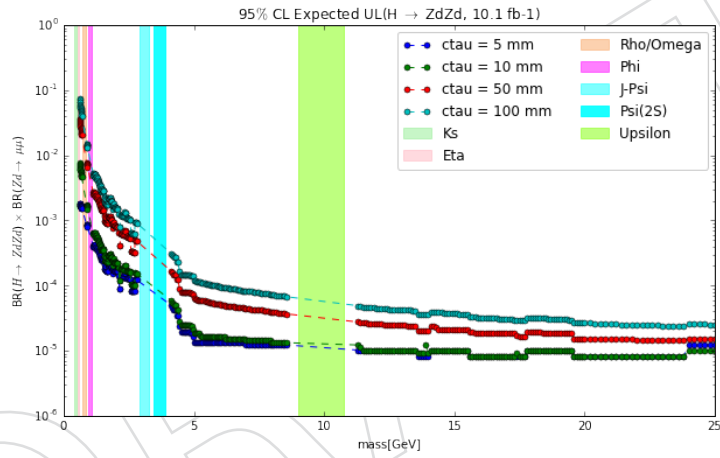


Figure 52: Exclusion limits at 95% CL on the branching ratio ($\text{BR}(H \rightarrow Z_D Z_D) \times \text{BR}(Z_D \rightarrow \mu\mu)$) as a function of the signal mass (m_{Z_D}) hypothesis for a number of representative lifetime ($c\tau_0^{Z_D}$) hypotheses, for the $H \rightarrow Z_D Z_D$ signal model.

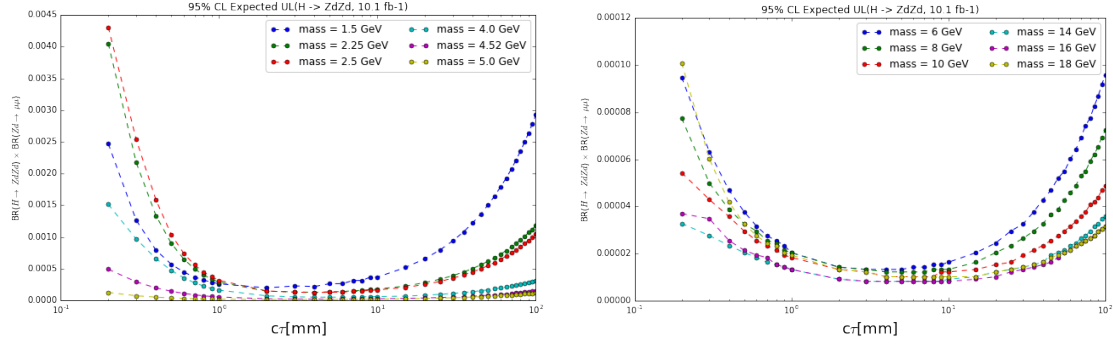


Figure 53: Exclusion limits at 95% CL on the branching ratio ($\text{BR}(H \rightarrow Z_D Z_D) \times \text{BR}(Z_D \rightarrow \mu\mu)$) as a function of the lifetime $c\tau_0^{Z_D}$ for a number of representative signal mass (m_{Z_D}) hypotheses, for the $H \rightarrow Z_D Z_D$ signal model.

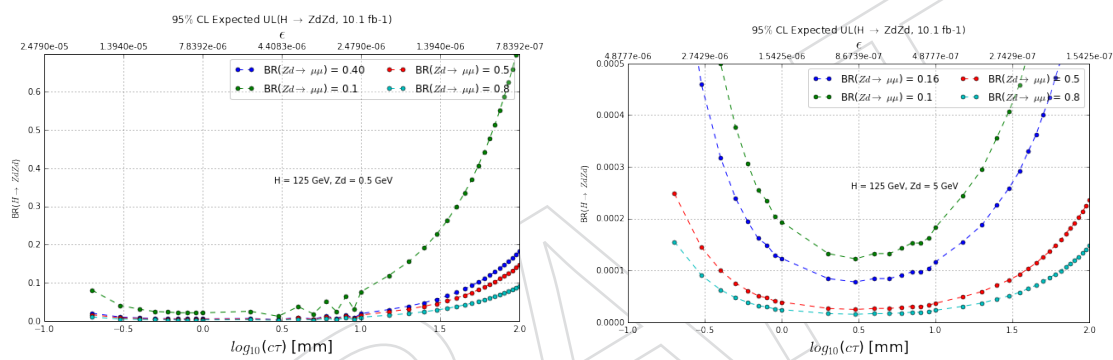


Figure 54: Exclusion limits at 95% CL on the branching ratio $\text{BR}(H \rightarrow Z_D Z_D)$ as a function of the lifetime $c\tau_0^{Z_D}$ (bottom x-axis) and ϵ (top x-axis) for representative signal mass (m_{Z_D}) hypotheses 0.5 GeV(left) and 5 GeV(right), for the $H \rightarrow Z_D Z_D$ signal model.

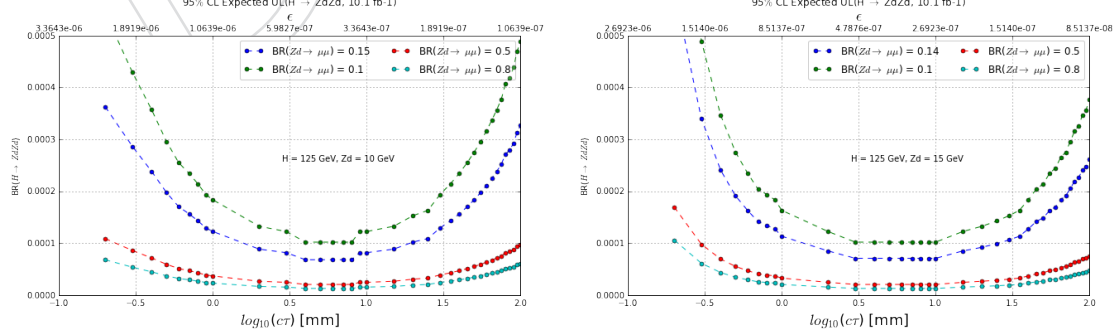


Figure 55: Exclusion limits at 95% CL on the branching ratio $\text{BR}(H \rightarrow Z_D Z_D)$ as a function of the lifetime $c\tau_0^{Z_D}$ (bottom x-axis) and ϵ (top x-axis) for representative signal mass (m_{Z_D}) hypotheses 10 GeV(left) and 15 GeV(right), for the $H \rightarrow Z_D Z_D$ signal model.

604 11 Summary

605 A search is performed for displaced dimuon resonances using proton-proton collision at a
606 center-of-mass energy of 13 TeV, collected by the CMS experiment at the LHC in 2017–2018,
607 corresponding to an integrated luminosity of 101.3 fb^{-1} . The data sets used in this search were
608 collected using a dedicated dimuon scouting trigger stream, in order to explore otherwise in-
609 accessible phase space at low dimuon mass and non-zero displacement from the interaction
610 point.

611 In this note, we describe in detail the search strategy as well as the event selection in use, and
612 we present the results of an end-to-end search **using only about 10% of the full data set (2017–**
613 **2018), corresponding to an integrated luminosity of 10.1 fb^{-1} .**

DRAFT

614 References

- 615 [1] G. Bertone and J. Silk, "Particle Dark Matter: Observations, Models and Searches".
 616 Cambridge Univ. Press, Cambridge, 2010. doi:[10.1017/CBO9780511770739](https://doi.org/10.1017/CBO9780511770739),
 617 ISBN 978-1-107-65392-4.
- 618 [2] J. L. Feng, "Dark Matter Candidates from Particle Physics and Methods of Detection",
 619 *Ann. Rev. Astron. Astrophys.* **48** (2010) 495–545,
 620 doi:[10.1146/annurev-astro-082708-101659](https://doi.org/10.1146/annurev-astro-082708-101659), arXiv:[1003.0904](https://arxiv.org/abs/1003.0904).
- 621 [3] T. A. Porter, R. P. Johnson, and P. W. Graham, "Dark Matter Searches with Astroparticle
 622 Data", *Ann. Rev. Astron. Astrophys.* **49** (2011) 155–194,
 623 doi:[10.1146/annurev-astro-081710-102528](https://doi.org/10.1146/annurev-astro-081710-102528), arXiv:[1104.2836](https://arxiv.org/abs/1104.2836).
- 624 [4] Planck Collaboration, "Planck 2015 results. XIII. Cosmological parameters", *Astron.
 625 Astrophys.* **594** (2016) A13, doi:[10.1051/0004-6361/201525830](https://doi.org/10.1051/0004-6361/201525830),
 626 arXiv:[1502.01589](https://arxiv.org/abs/1502.01589).
- 627 [5] R. Essig et al., "Working Group Report: New Light Weakly Coupled Particles", in
 628 *Community Summer Study 2013: Snowmass on the Mississippi*. 10, 2013.
 629 arXiv:[1311.0029](https://arxiv.org/abs/1311.0029).
- 630 [6] D. Curtin, R. Essig, S. Gori, and J. Shelton, "Illuminating Dark Photons with High-Energy
 631 Colliders", *JHEP* **02** (2015) 157, doi:[10.1007/JHEP02\(2015\)157](https://doi.org/10.1007/JHEP02(2015)157),
 632 arXiv:[1412.0018](https://arxiv.org/abs/1412.0018).
- 633 [7] A. Konaka et al., "Search for Neutral Particles in Electron Beam Dump Experiment",
 634 *Phys. Rev. Lett.* **57** (1986) 659, doi:[10.1103/PhysRevLett.57.659](https://doi.org/10.1103/PhysRevLett.57.659).
- 635 [8] APEX Collaboration, "Search for a New Gauge Boson in Electron-Nucleus Fixed-Target
 636 Scattering by the APEX Experiment", *Phys. Rev. Lett.* **107** (2011) 191804,
 637 doi:[10.1103/PhysRevLett.107.191804](https://doi.org/10.1103/PhysRevLett.107.191804), arXiv:[1108.2750](https://arxiv.org/abs/1108.2750).
- 638 [9] BaBar Collaboration, "Search for Dimuon Decays of a Light Scalar Boson in Radiative
 639 Transitions $Y \rightarrow \gamma A^0$ ", *Phys. Rev. Lett.* **103** (2009) 081803,
 640 doi:[10.1103/PhysRevLett.103.081803](https://doi.org/10.1103/PhysRevLett.103.081803), arXiv:[0905.4539](https://arxiv.org/abs/0905.4539).
- 641 [10] SINDRUM I Collaboration, "Search for weakly interacting neutral bosons produced in
 642 $\pi^- p$ interactions at rest and decaying into $e^+ e^-$ pairs.", *Phys. Rev. Lett.* **68** (1992)
 643 3845–3848, doi:[10.1103/PhysRevLett.68.3845](https://doi.org/10.1103/PhysRevLett.68.3845).
- 644 [11] LHCb Collaboration, "Proposed Inclusive Dark Photon Search at LHCb", *Phys. Rev. Lett.*
 645 **116** (2016), no. 25, 251803, doi:[10.1103/PhysRevLett.116.251803](https://doi.org/10.1103/PhysRevLett.116.251803),
 646 arXiv:[1603.08926](https://arxiv.org/abs/1603.08926).
- 647 [12] LHCb Collaboration, "Search for Dark Photons Produced in 13 TeV pp Collisions", *Phys.
 648 Rev. Lett.* **120** (2018), no. 6, 061801, doi:[10.1103/PhysRevLett.120.061801](https://doi.org/10.1103/PhysRevLett.120.061801),
 649 arXiv:[1710.02867](https://arxiv.org/abs/1710.02867).
- 650 [13] LHCb Collaboration, "Search for $A' \rightarrow \mu^+ \mu^-$ Decays", *Phys. Rev. Lett.* **124** (2020), no. 4,
 651 041801, doi:[10.1103/PhysRevLett.124.041801](https://doi.org/10.1103/PhysRevLett.124.041801), arXiv:[1910.06926](https://arxiv.org/abs/1910.06926).
- 652 [14] CMS Collaboration, "Search for a Narrow Resonance Lighter than 200 GeV Decaying to a
 653 Pair of Muons in Proton-Proton Collisions at $\sqrt{s} = 13$ TeV", *Phys. Rev. Lett.* **124** (2020),
 654 no. 13, 131802, doi:[10.1103/PhysRevLett.124.131802](https://doi.org/10.1103/PhysRevLett.124.131802), arXiv:[1912.04776](https://arxiv.org/abs/1912.04776).

- 655 [15] J. A. Evans, A. Gadrakota, S. Knapen, and H. Routray, “Searching for exotic B meson
656 decays with the CMS L1 track trigger”, arXiv:2008.06918.
- 657 [16] CMS Collaboration, “The CMS Experiment at the CERN LHC”, *JINST* **3** (2008) S08004,
658 doi:10.1088/1748-0221/3/08/S08004.
- 659 [17] CMS Collaboration, “The CMS trigger system”, *JINST* **12** (2017), no. 01, P01020,
660 doi:10.1088/1748-0221/12/01/P01020, arXiv:1609.02366.
- 661 [18] CMS Collaboration Collaboration, “Data Parking and Data Scouting at the CMS
662 Experiment”, CMS Detector Performance Note CMS-DP-2012-022, CERN, 2012.
- 663 [19] CMS Collaboration, “Search for narrow resonances in dijet final states at $\sqrt{s} = 8$ TeV
664 with the novel CMS technique of data scouting”, *Phys. Rev. Lett.* **117** (2016), no. 3,
665 031802, doi:10.1103/PhysRevLett.117.031802, arXiv:1604.08907.
- 666 [20] CMS Collaboration, “CMS Technical Design Report for the Pixel Detector Upgrade”,
667 CMS Technical Design Report CERN-LHCC-2012-016, CMS-TDR-11, CERN, 2012.
- 668 [21] P. Nason, “A new method for combining NLO QCD with shower Monte Carlo
669 algorithms”, *JHEP* **11** (2004) 040, doi:10.1088/1126-6708/2004/11/040,
670 arXiv:hep-ph/0409146.
- 671 [22] S. Frixione, P. Nason, and C. Oleari, “Matching NLO QCD computations with parton
672 shower simulations: the POWHEG method”, *JHEP* **11** (2007) 070,
673 doi:10.1088/1126-6708/2007/11/070, arXiv:0709.2092.
- 674 [23] S. Alioli, P. Nason, C. Oleari, and E. Re, “NLO single-top production matched with
675 shower in POWHEG: s - and t -channel contributions”, *JHEP* **09** (2009) 111,
676 doi:10.1088/1126-6708/2009/09/111, arXiv:0907.4076. [Erratum:
677 doi:10.1007/JHEP02(2010)011].
- 678 [24] Y. Gao et al., “Spin Determination of Single-Produced Resonances at Hadron Colliders”,
679 *Phys. Rev. D* **81** (2010) 075022, doi:10.1103/PhysRevD.81.075022,
680 arXiv:1001.3396.
- 681 [25] S. Bolognesi et al., “On the spin and parity of a single-produced resonance at the LHC”,
682 *Phys. Rev. D* **86** (2012) 095031, doi:10.1103/PhysRevD.86.095031,
683 arXiv:1208.4018.
- 684 [26] I. Anderson et al., “Constraining Anomalous HVV Interactions at Proton and Lepton
685 Colliders”, *Phys. Rev. D* **89** (2014), no. 3, 035007,
686 doi:10.1103/PhysRevD.89.035007, arXiv:1309.4819.
- 687 [27] A. V. Gritsan, R. Rentsch, M. Schulze, and M. Xiao, “Constraining anomalous Higgs boson
688 couplings to the heavy flavor fermions using matrix element techniques”, *Phys. Rev. D*
689 **94** (2016), no. 5, 055023, doi:10.1103/PhysRevD.94.055023, arXiv:1606.03107.
- 690 [28] A. V. Gritsan et al., “New features in the JHU generator framework: constraining Higgs
691 boson properties from on-shell and off-shell production”, arXiv:2002.09888.
- 692 [29] T. Sjöstrand et al., “An Introduction to PYTHIA 8.2”, *Comput. Phys. Commun.* **191** (2015)
693 159, doi:10.1016/j.cpc.2015.01.024, arXiv:1410.3012.

- [30] M. Cepeda et al., “Report from Working Group 2: Higgs Physics at the HL-LHC and HE-LHC”, *CERN Yellow Rep. Monogr.* **7** (2019) 221–584,
 doi:[10.23731/CYRM-2019-007.221](https://doi.org/10.23731/CYRM-2019-007.221), arXiv:[1902.00134](https://arxiv.org/abs/1902.00134).
- [31] J. Alwall et al., “The automated computation of tree-level and next-to-leading order differential cross sections, and their matching to parton shower simulations”, *JHEP* **07** (2014) 079, doi:[10.1007/JHEP07\(2014\)079](https://doi.org/10.1007/JHEP07(2014)079), arXiv:[1405.0301](https://arxiv.org/abs/1405.0301).
- [32] M. Cacciari, M. Greco, and P. Nason, “The P(T) spectrum in heavy flavor hadroproduction”, *JHEP* **05** (1998) 007, doi:[10.1088/1126-6708/1998/05/007](https://doi.org/10.1088/1126-6708/1998/05/007), arXiv:[hep-ph/9803400](https://arxiv.org/abs/hep-ph/9803400).
- [33] M. Cacciari, S. Frixione, and P. Nason, “The p(T) spectrum in heavy flavor photoproduction”, *JHEP* **03** (2001) 006, doi:[10.1088/1126-6708/2001/03/006](https://doi.org/10.1088/1126-6708/2001/03/006), arXiv:[hep-ph/0102134](https://arxiv.org/abs/hep-ph/0102134).
- [34] M. Cacciari et al., “Theoretical predictions for charm and bottom production at the LHC”, *JHEP* **10** (2012) 137, doi:[10.1007/JHEP10\(2012\)137](https://doi.org/10.1007/JHEP10(2012)137), arXiv:[1205.6344](https://arxiv.org/abs/1205.6344).
- [35] M. Cacciari, M. L. Mangano, and P. Nason, “Gluon PDF constraints from the ratio of forward heavy-quark production at the LHC at $\sqrt{S} = 7$ and 13 TeV”, *Eur. Phys. J. C* **75** (2015), no. 12, 610, doi:[10.1140/epjc/s10052-015-3814-x](https://doi.org/10.1140/epjc/s10052-015-3814-x), arXiv:[1507.06197](https://arxiv.org/abs/1507.06197).
- [36] CMS Collaboration, “Extraction and validation of a new set of CMS PYTHIA8 tunes from underlying-event measurements”, *Eur. Phys. J. C* **80** (2020), no. 1, 4, doi:[10.1140/epjc/s10052-019-7499-4](https://doi.org/10.1140/epjc/s10052-019-7499-4), arXiv:[1903.12179](https://arxiv.org/abs/1903.12179).
- [37] NNPDF Collaboration, “Parton distributions from high-precision collider data”, *Eur. Phys. J. C* **77** (2017) 663, doi:[10.1140/epjc/s10052-017-5199-5](https://doi.org/10.1140/epjc/s10052-017-5199-5), arXiv:[1706.00428](https://arxiv.org/abs/1706.00428).
- [38] GEANT4 Collaboration, “GEANT4—a simulation toolkit”, *Nucl. Instrum. Meth. A* **506** (2003) 250, doi:[10.1016/S0168-9002\(03\)01368-8](https://doi.org/10.1016/S0168-9002(03)01368-8).
- [39] “<https://github.com/cms-sw/cmssw/blob/master/TrackingTools/GeomPropagators/interface/Propagator.h>”.
<https://github.com/cms-sw/cmssw/blob/master/TrackingTools/GeomPropagators/interface/Propagator.h>.
- [40] “<https://github.com/cms-sw/cmssw/blob/master/TrackingTools/DetLayers/interface/GeomDetCompatibilityChecker.h>”.
<https://github.com/cms-sw/cmssw/blob/master/TrackingTools/DetLayers/interface/GeomDetCompatibilityChecker.h>.
- [41] “<https://github.com/cms-sw/cmssw/blob/master/RecoVertex/KalmanVertexFit/interface/KalmanVertexFitter.h>”.
<https://github.com/cms-sw/cmssw/blob/master/RecoVertex/KalmanVertexFit/interface/KalmanVertexFitter.h>.
- [42] “<https://twiki.cern.ch/twiki/bin/viewauth/CMS/SWGuideMuonIdRun2>”.
<https://twiki.cern.ch/twiki/bin/viewauth/CMS/SWGuideMuonIdRun2>.
- [43] R. A. Fisher, “On the Interpretation of χ^2 from Contingency Tables, and the Calculation of P”, *Journal of the Royal Statistical Society* **85** (1922), no. 1, 87–94.

- 735 [44] P. Dauncey, M. Kenzie, N. Wardle, and G. Davies, “Handling uncertainties in background
736 shapes: the discrete profiling method”, *JINST* **10** (2015), no. 04, P04015,
737 doi:10.1088/1748-0221/10/04/P04015, arXiv:1408.6865.
- 738 [45] CMS Collaboration, “A measurement of the Higgs boson mass in the diphoton decay
739 channel”, *Phys. Lett. B* **805** (2020) 135425, doi:10.1016/j.physletb.2020.135425,
740 arXiv:2002.06398.
- 741 [46] “<https://gitlab.cern.ch/tdr/notes/AN-19-196/-/tree/master/Figures/background/5sigma/fits>”. <https://gitlab.cern.ch/tdr/notes/AN-19-196/-/tree/master/Figures/background/5sigma/fits>.
- 744 [47] T. Junk, “Confidence level computation for combining searches with small statistics”,
745 *Nucl. Instrum. Meth. A* **434** (1999) 435, doi:10.1016/S0168-9002(99)00498-2,
746 arXiv:hep-ex/9902006.
- 747 [48] A. L. Read, “Presentation of search results: The CL_s technique”, *J. Phys. G* **28** (2002) 2693,
748 doi:10.1088/0954-3899/28/10/313.
- 749 [49] G. Cowan, K. Cranmer, E. Gross, and O. Vitells, “Asymptotic formulae for
750 likelihood-based tests of new physics”, *Eur. Phys. J. C* **71** (2011) 1554,
751 doi:10.1140/epjc/s10052-011-1554-0, arXiv:1007.1727. [Erratum:
752 doi:10.1140/epjc/s10052-013-2501-z].
- 753 [50] ATLAS and CMS Collaborations, “Procedure for the LHC Higgs boson search
754 combination in summer 2011”, ATLAS/CMS joint note ATL-PHYS-PUB-2011-011,
755 CMS-NOTE-2011-005, 2011.
- 756 [51] CMS Collaboration, “CMS luminosity measurement for the 2017 data-taking period at
757 $\sqrt{s} = 13 \text{ TeV}$ ”, CMS Physics Analysis Summary CMS-PAS-LUM-17-004, 2018.
- 758 [52] CMS Collaboration, “CMS luminosity measurement for the 2018 data-taking period at
759 $\sqrt{s} = 13 \text{ TeV}$ ”, CMS Physics Analysis Summary CMS-PAS-LUM-18-002, 2019.
- 760 [53] “https://gitlab.cern.ch/tdr/notes/AN-19-196/-/tree/master/Figures/app_biasoftests/biastest”. https://gitlab.cern.ch/tdr/notes/AN-19-196/-/tree/master/Figures/app_biasoftests/biastest.
- 763 [54] “<https://cms-analysis.github.io/HiggsAnalysis-CombinedLimit/part3/commonstatsmethods/#goodness-of-fit-tests>”.
764 <https://cms-analysis.github.io/HiggsAnalysis-CombinedLimit/part3/commonstatsmethods/#goodness-of-fit-tests>.
- 767 [55] “https://gitlab.cern.ch/tdr/notes/AN-19-196/-/tree/master/Figures/app_biasoftests/goftest”. https://gitlab.cern.ch/tdr/notes/AN-19-196/-/tree/master/Figures/app_biasoftests/goftest.

770 A Proof of principle: observation of known resonances

771 As a proof of principle experiment, in the attempt to demonstrate the achievable search sen-
 772 sitivity, we apply the full search strategy and selection using the known J/ψ resonance as a
 773 “standard candle”. As shown in Fig. 56, the J/ψ resonant peak is clearly visible across l_{xy} bins.

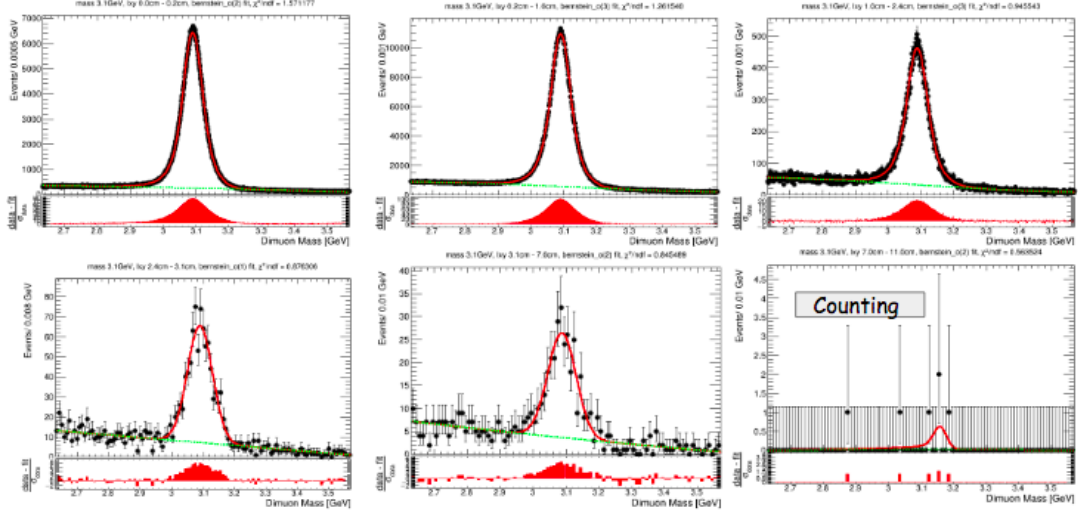


Figure 56: Proof of principle: J/ψ resonance in bins of l_{xy} .

774 Similarly, we use the known K_S resonance as an additional “standard candle”: as shown in
 775 Fig. 57, the K_S resonant peak is clearly visible across l_{xy} bins. In this case, because the lifetime
 776 of K_S is not negligible, the peak is mostly visible at larger l_{xy} . We note that K_S actually decays
 777 into a pair of pions, which are here mis-identified as muons originating from the same DV,
 778 causing a shift of the reconstructed mass from the nominal one ($m_{K_S}^{\text{nominal}} = 497.6 \text{ MeV}$).

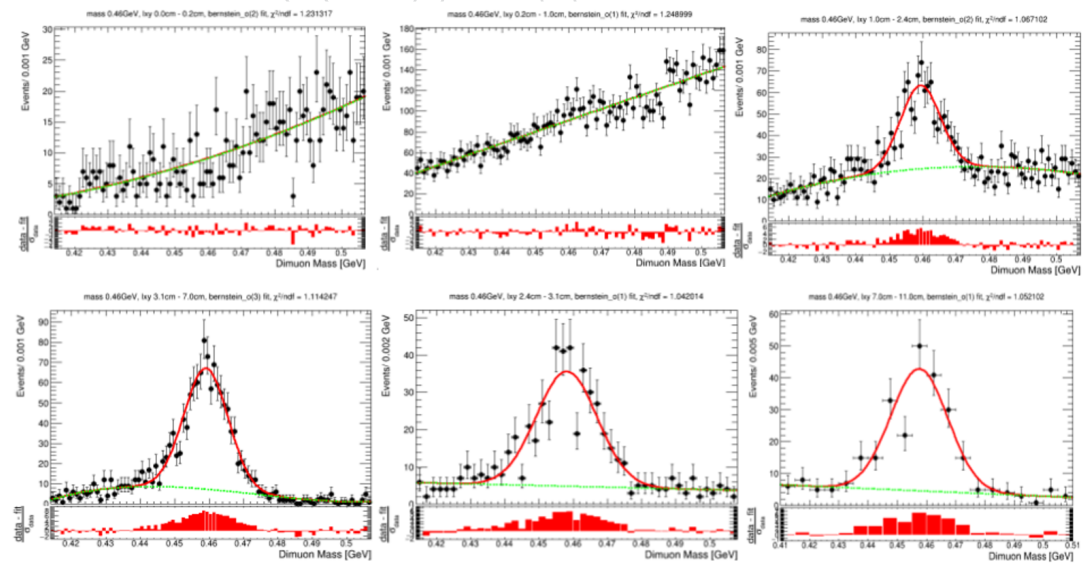


Figure 57: Proof of principle: K_S resonance in bins of l_{xy} .

779 B Invariant mass: on the correction of muon ϕ

780 In order to improve the dimuon invariant mass ($m_{\mu\mu}$) resolution, the ϕ component of each
 781 muon is recomputed to account for its displacement with respect to the beamspot. Each muon
 782 is propagated (via simple helix propagation) from its reference point (nominally defined as the
 783 point of closest approach to the center of CMS) to the position of the associated DV, and the ϕ
 784 component of the muon vector is updated accordingly. Because of the absence of bending in
 785 the $\rho - z$ plane, no correction is required for the η component of the muon itself.

786 The effect of the correction is mainly relevant at large displacements, where the dimuon invari-
 787 ant mass otherwise suffers from poor resolution at the point that a bimodal structure of the
 788 mass peak is observed, as shown in Fig. 58 for representative signal models.

789 The effect of the correction is as well visible in data, as shown in Fig. 59, where the improvement
 790 in mass resolution appears significant for all the known low-mass dimuon resonances.

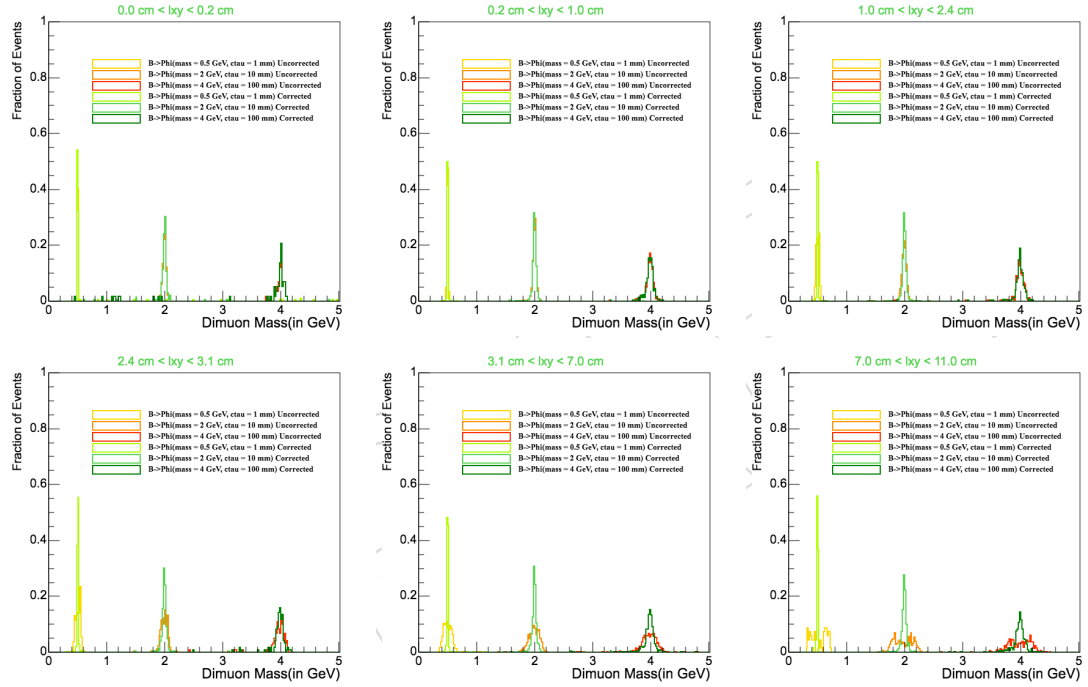


Figure 58: Effect of muon ϕ correction on dimuon invariant mass, in bins of l_{xy} , for representa-
 tive ($B \rightarrow \phi X$) signal models.

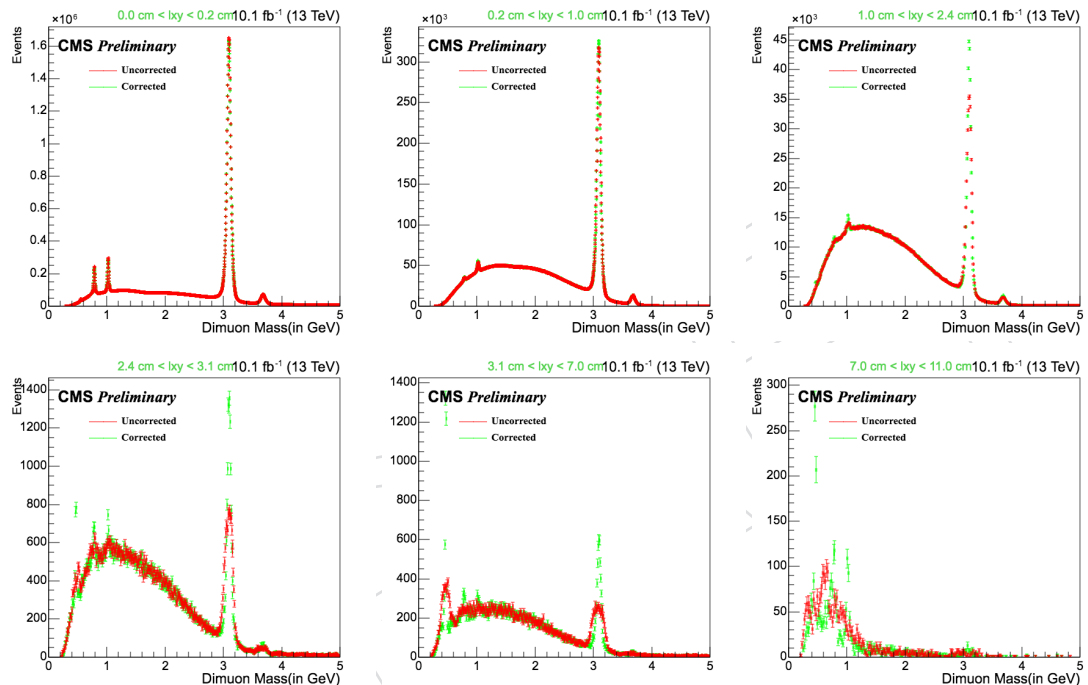


Figure 59: Effect of muon ϕ correction on dimuon invariant mass, in bins of l_{xy} , for data (10.1fb^{-1}).

791 C Alternative signal mass interpolation

792 As an alternative choice for signal mass interpolation with respect to the primary choice de-
 793 scribed in Section 8 is presented, using a Voigtian probability density function instead of a sum
 794 of a double Crystal Ball and a Gaussian function.

795 The Voigtian probability density function results from the convolution of a Breit-Wigner and
 796 a Gaussian function, and is here used to model the signal dimuon mass distribution for the
 797 signal models explored in this search (see Section 3).

798 A Breit-Wigner function is characterized by two parameters, Γ and σ . Fits of the dimuon mass
 799 distribution for different signal mass and lifetime hypotheses are performed. A selection of
 800 such fits is shown in Figs. 60-63. The resulting relative Γ and σ parameters are evaluated and
 801 compared across signal mass and lifetime (Figs. 64-65), and both parameters are found to be
 802 consistent with a constant value of 0.01, to be used for signal mass shape interpolation. A
 803 systematic uncertainty is assessed in order to cover for all observed disagreements from such
 804 constant value.

805 We note that the primary approach (see Section 8) is preferred since a Voigtian probability
 806 density function is considered a less suitable option than the sum of a double Crystal Ball and
 807 a Gaussian function in order to fit a resonance whose generator-level width is ~ 0 .

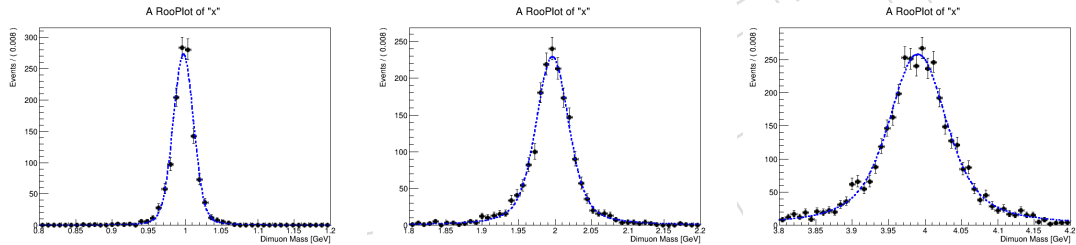


Figure 60: Fit of signal mass distribution for representative $B \rightarrow \phi X$ signal mass hypotheses and $c\tau_0 = 10$ mm.

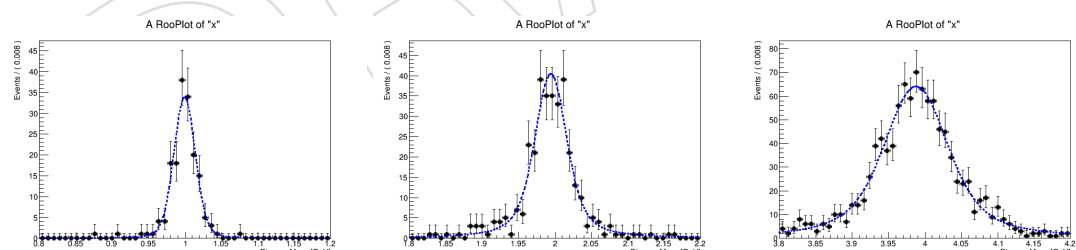


Figure 61: Fit of signal mass distribution for representative $B \rightarrow \phi X$ signal mass hypotheses and $c\tau_0 = 100$ mm.

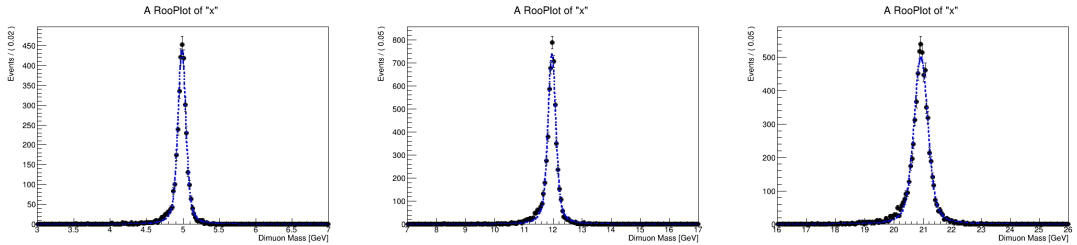


Figure 62: Fit of signal mass distribution for representative $H \rightarrow Z_D Z_D$ signal mass hypotheses and $c\tau_0 = 10$ mm.

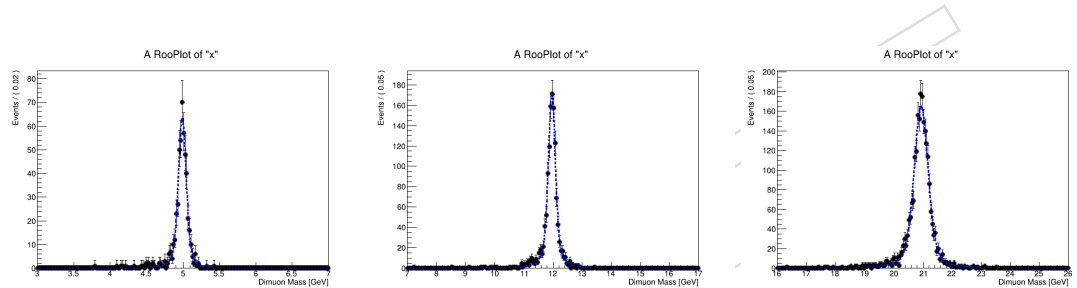


Figure 63: Fit of signal mass distribution for representative $H \rightarrow Z_D Z_D$ signal mass hypotheses and $c\tau_0 = 100$ mm.

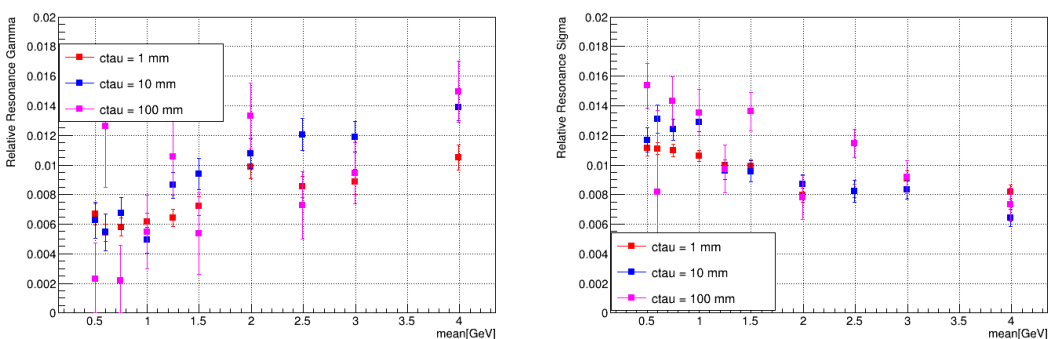


Figure 64: Relative resonance width (Γ and σ) as a function of the mean m_ϕ (as determined from a fit of the signal dimuon mass distribution) for representative $B \rightarrow \phi X$ signal models with different $c\tau_0^\phi$.

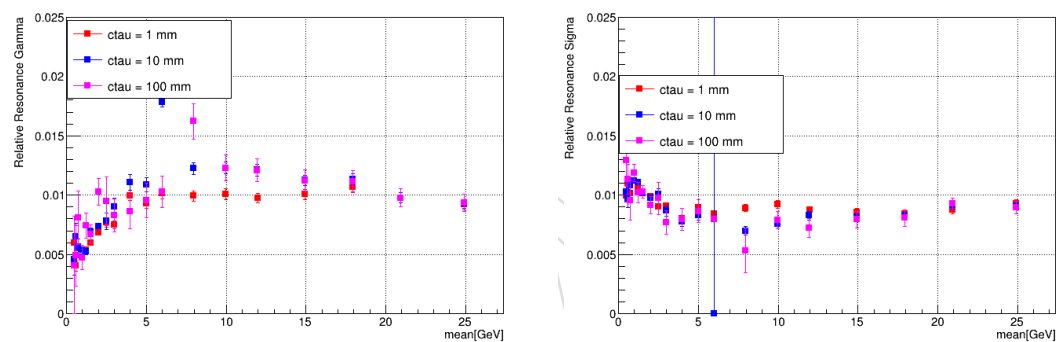


Figure 65: Relative resonance width (Γ and σ) as a function of the mean m_{Z_D} (as determined from a fit of the signal dimuon mass distribution) for representative $H \rightarrow Z_D \bar{Z}_D$ signal models with different $c\tau_0^{Z_D}$

808 D Two-dimensional signal acceptance interpolation

809 A fixed coarse grid of $(m_{\phi/Z_D}, c\tau_0^{\phi/Z_D})$ signal points for each model is generated, then we
 810 perform a lifetime-based reweighting (Section 7) as well as a parametrization of the signal
 811 resonance width as a function of its mass (Section 8). Finally, in order to determine the signal
 812 acceptance in a finer $(m_{\phi/Z_D}, c\tau_0^{\phi/Z_D})$ grid, a two-dimensional interpolation method is used
 813 that combines the previous procedures, in bins of l_{xy} .

814 In particular, a two-dimensional spline-based interpolation is used, as shown in Fig. 66 and in
 815 Fig. 67 for $B \rightarrow \phi X$ and $H \rightarrow Z_D Z_D$, respectively.

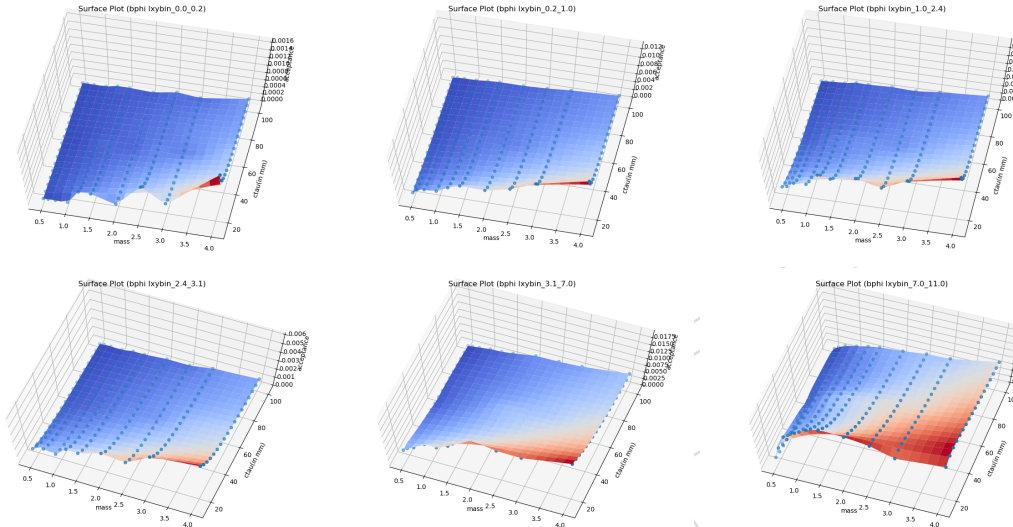


Figure 66: Acceptance two-dimensional ($m, c\tau_0$) interpolation in bins of l_{xy} for $B \rightarrow \phi X$ signal.

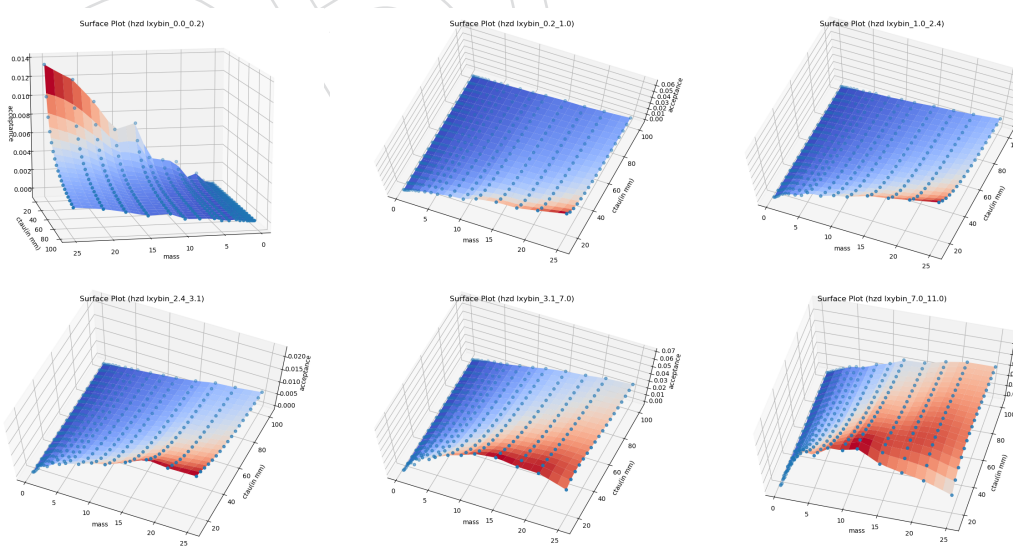


Figure 67: Acceptance two-dimensional ($m, c\tau_0$) interpolation in bins of l_{xy} for $H \rightarrow Z_D Z_D$ signal.

816 E Fit vs. counting experiment

- 817 For a given signal mass hypothesis, we either perform a shape analysis or a counting exper-
818 iment in bins of (l_{xy} , $p_T^{\mu\mu}$, isolation), as described in Section 4, depending on the available statis-
819 tics.
- 820 In each (l_{xy} , $p_T^{\mu\mu}$, isolation) bin, we define mass windows sliding along the dimuon invariant
821 mass spectrum, and we perform a search for a resonant dimuon peak in each mass window.
- 822 For the shape analysis, we parametrize the background in a mass window of $\pm 5\sigma$ around the
823 signal mass hypothesis, using a polynomial functional form as probability density function. In
824 the case of counting experiments, we define a signal mass window of $\pm 2\sigma$ around the signal
825 mass hypothesis, and use sidebands ($[-5\sigma, -2\sigma] + [+2\sigma, +5\sigma]$) to estimate the background in
826 the signal window itself.
- 827 Counting experiments are performed in the case where the number of data events in sidebands
828 is < 20 . If the number of data events in sidebands is ≥ 20 , we instead perform a shape analysis.
829 The choice of such threshold (i.e., < 20 or ≥ 20 events in sidebands) is justified in the following.
- 830 We expect constraints obtained from a counting experiment and a shape analysis to converge
831 in the case of low statistics bins, while the shape analysis is expected to perform better and
832 better at increasing statistics.
- 833 In the attempt to confirm such expectation as well as to determine a threshold on the number
834 of events in sidebands to be used in order to decide whether a shape analysis or a counting
835 experiment should be performed, we compare upper limits on the number of signal events ob-
836 tained with one and the other approach in individual (l_{xy} , $p_T^{\mu\mu}$, isolation) search bins, scanning
837 over mass windows with varying statistics, using 10.1fb^{-1} of data.
- 838 Upper limits are obtained as described in Section 10. For shape analyses, a 1st order polynomial
839 is used to parametrize the background: this choice, driven by simplicity, allows for a direct
840 comparison of the two approaches under test, and is anyways a suitable choice in low statistics
841 regimes. A systematic uncertainty equal to 5% is assessed on background predictions for both
842 shape analyses and counting experiments, in addition to the uncertainty arising from statistics.
- 843 Figure 68 shows the ratio of the upper limits obtained with a shape analysis approach and with
844 a counting experiment, as a function of the number of events in sidebands. As expected, the
845 ratio appears to converge (at $\sim 93\%$) when the low statistics regime is approached, i.e., for a
846 number of events in sidebands $\lesssim 20$. When the number of events in sidebands is larger, shape
847 analyses are found to perform better.
- 848 The ratio of upper limits is found to converge at $\sim 93\%$ rather than unity, due to the additional
849 information on the signal line shape which on the one hand is provided as input to a shape
850 analysis, and on the other hand is not used in counting experiments.
- 851 Supported by these results, we set the threhsold on the number of events in sidebands to be
852 used in order to decide whether a shape analysis or a counting experiment should be per-
853 formed to 20.

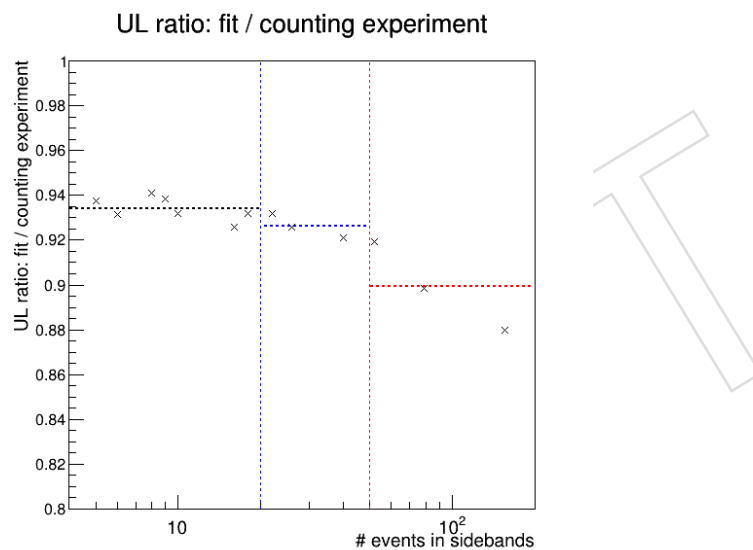


Figure 68: Ratio of upper limits on the number of signal events as obtained from a shape analysis and from a counting experiments, in individual search bins with varying number of events in mass window sidebands. The vertical blue dashed line indicates number of events in sidebands = 20; the vertical red dashed line indicates number of events in sidebands = 50. The horizontal black, blue and red dashed lines indicate the results of a constant fit to the ratio in the ranges [0, 20], [20, 50] and [50, 200] for the number of events in sidebands, respectively.

854 F On the definition of “masked” mass windows

855 For a given signal mass hypothesis, we either perform a shape analysis or a counting exper-
 856 iment in bins of (l_{xy} , $p_T^{\mu\mu}$, isolation), as described in Section 4, depending on the available statis-
 857 tics. For the shape analysis, we parametrize the background in a mass window of $\pm 5\sigma$ around
 858 the signal mass hypothesis, using a polynomial functional form as probability density function.
 859 In the case of counting experiments, we define a signal mass window of $\pm 2\sigma$ around the signal
 860 mass hypothesis, and use sidebands ($[-5\sigma, -2\sigma] + [+2\sigma, +5\sigma]$) to estimate the background in
 861 the signal window itself.

862 The full mass window ($\pm 5\sigma$ around the signal mass hypothesis) is required to not overlap
 863 with any of the known (SM) resonances, as well as with potential “fake” dimuon resonances
 864 where pions are wrongly identified as muons (e.g., K_S). To this purpose, we define a number
 865 of “masked” regions, based on the position and the width of such resonances.

866 In order to define the position and size of the “masked” regions, we fit the known resonances in
 867 data (10.1fb^{-1}) using a probability density function resulting from the sum of a double Crystal
 868 Ball and a Gaussian function, as for signal (see Section 8), freezing all parameters but mean and
 869 σ , while the background is parametrized using polynomial functional forms, as for the actual
 870 search (see Section 9).

871 Because some of the resonances decay promptly, in those case we relax our selection on the
 872 muon transverse impact parameter (see Section 5.2.4) to allow for a better fit and avoid issues
 873 related to lack of statistics.

874 We use the results of the fits to data in order to define the position and the size of the “masked”
 875 regions, which are centered around the mean resonance mass and whose size is as large as $\pm 5\sigma$
 876 (mean and σ are obtained from the fits to data).

877 The “masked” regions are listed in Table 3. Figures 69-70 show the results of the fits.

Table 3: List of known resonances and corresponding “masked” mass windows.

Resonance	Mean mass [GeV]	σ [MeV]	Lower bound [GeV] (mean -5σ)	Upper bound [GeV] (mean $+5\sigma$)
K_S	0.46	6.30	0.43	0.49
η	0.55	6.05	0.52	0.58
ρ/ω	0.78	11.20	0.73	0.84
ϕ	1.02	12.60	0.96	1.08
J/ψ	3.09	36.00	2.91	3.27
$\Psi(2S)$	3.68	42.00	3.47	3.89
$\Upsilon(1S)$	9.43	87.60	8.99	9.87
$\Upsilon(2S)$	10.00	77.80	9.61	10.39
$\Upsilon(3S)$	10.32	89.40	9.87	10.77

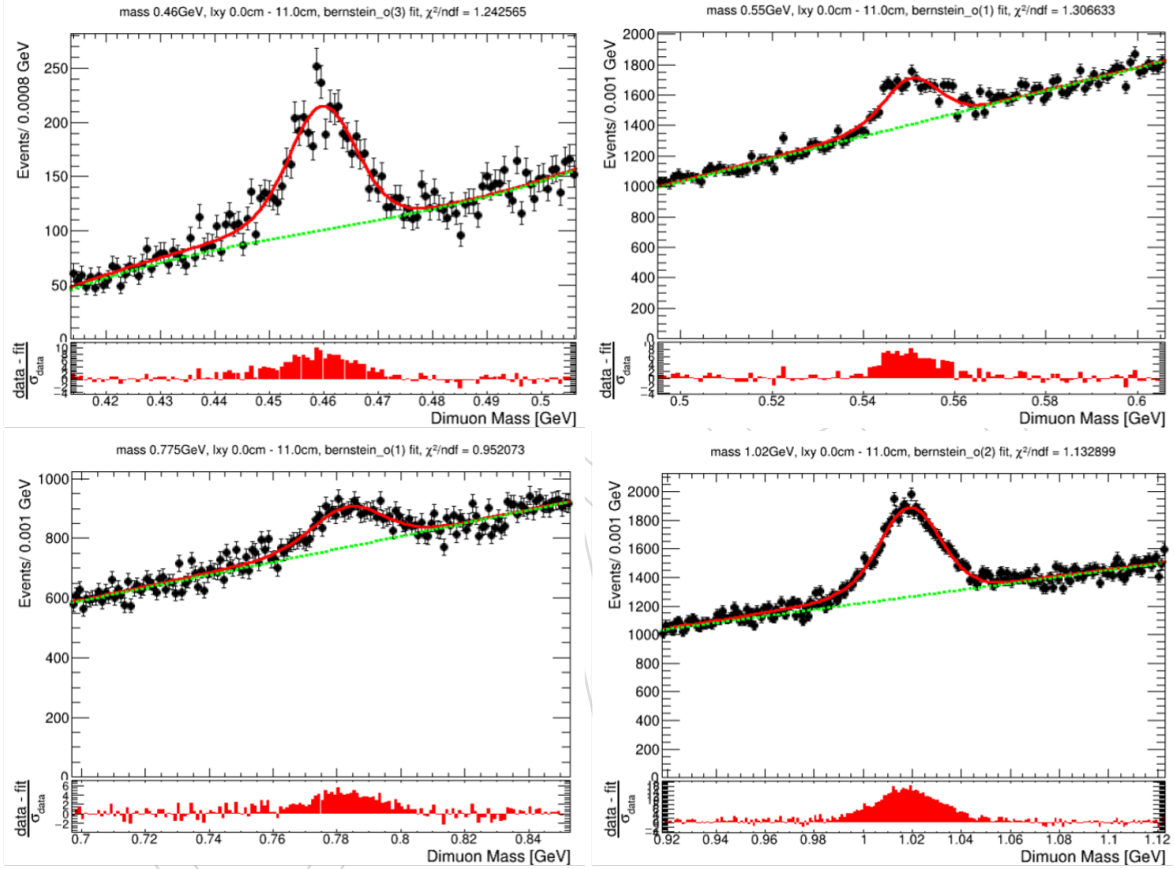


Figure 69: Fits to data (10.1fb^{-1}) of known resonances at low dimuon invariant mass. (Upper left) Fit to data of K_S . (Upper right) Fit to data of η (after relaxing selections on muon transverse impact parameter). (Lower left) Fit to data of ρ/ω . (Lower right) Fit to data of ϕ .

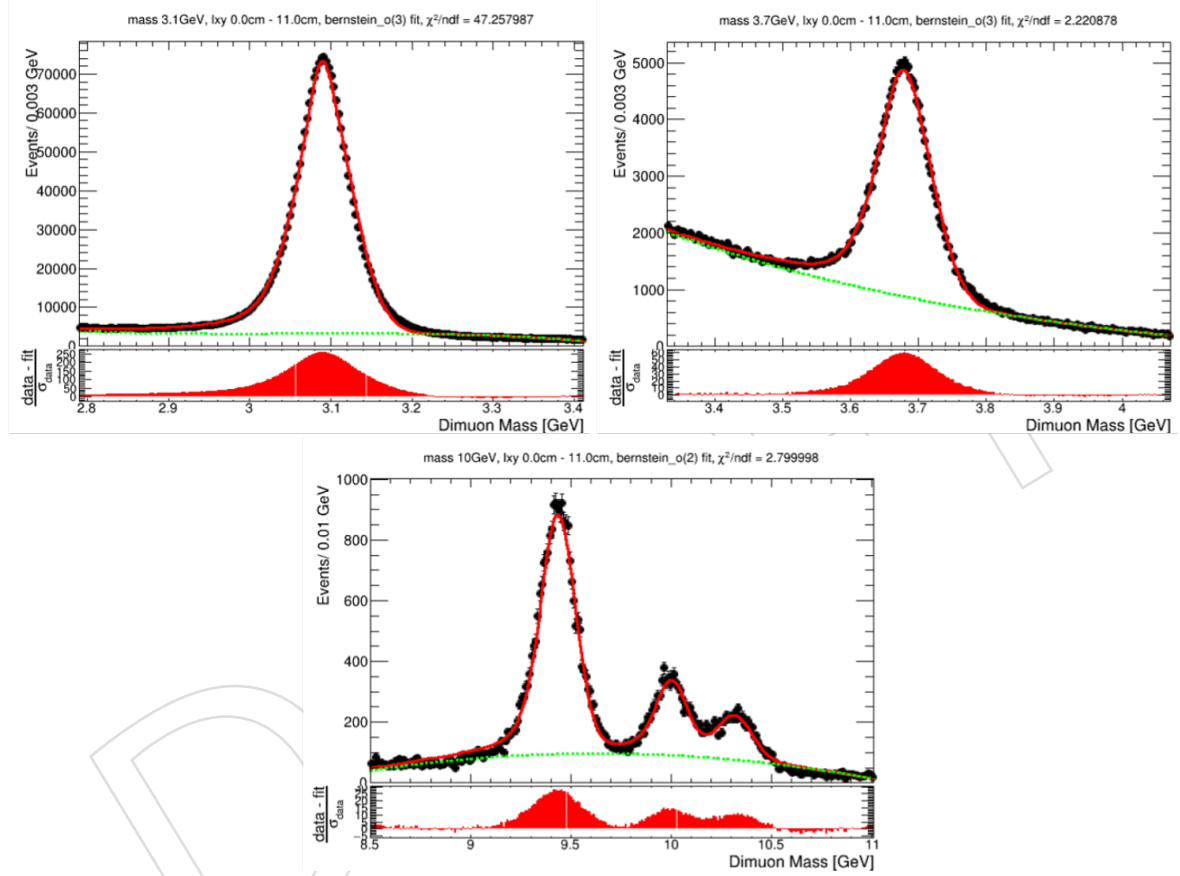


Figure 70: Fits to data (10.1fb^{-1}) of known resonances at larger dimuon invariant mass. (Upper left) Fit to data of J/ψ . (Upper right) Fit to data of $\Psi(2S)$. (Lower) Fit to data of $Y(1S)$, $Y(2S)$ and $Y(3S)$ (after relaxing selections on muon transverse impact parameter).

878 G Bias and goodness-of-fit tests

879 For each of the bins where a shape analysis or a counting experiment is performed, we perform
 880 bias tests using toy data sets after injecting signals of strength $r = 2$ and $r = 5$. We then proceed
 881 to the evaluation of $\frac{r_{\text{measured}} - r_{\text{injected}}}{\sigma_r}$, observing that biases are under control for all of the bins, i.e.,
 882 observing no significant deviation from zero for $\frac{r_{\text{measured}} - r_{\text{injected}}}{\sigma_r}$. This is shown in Figs. 71-76 for a
 883 number of representative signal mass hypotheses, for the case of $r_{\text{injected}} = 2$. Analogous results
 884 are obtained for $r_{\text{injected}} = 5$, as well as for other signal mass hypotheses. All distributions are
 885 collected in Ref. [53].

886 Bias tests are also performed on the combined datacards which result from the combination of
 887 all fit and count bins. The mean bias (expressed in %) is shown in Fig. 77 for a range of signal
 888 mass and lifetime hypotheses: no significant bias is observed.

889 Finally, for bins where a shape analysis is performed, goodness-of-fit (GOF) tests are performed
 890 using the saturated model method, as prescribed by the Statistics Committee [54]. As shown
 891 in Figs. 78-82, where the results of GOF test are displayed for a number of representative signal
 892 mass hypotheses, we observe that the p -value for all of the performed fits lies within the distri-
 893 bution expected from toy data sets. All distributions are collected in Ref. [55]. As an additional
 894 figure of merit to evaluate the goodness of the fits, we also use the overall χ^2/ndof in bins of
 895 l_{xy} as a function of the signal mass hypothesis under test. This is shown in Fig. 83: as expected
 896 in the case of good fits, χ^2/ndof is found to be close to unity.

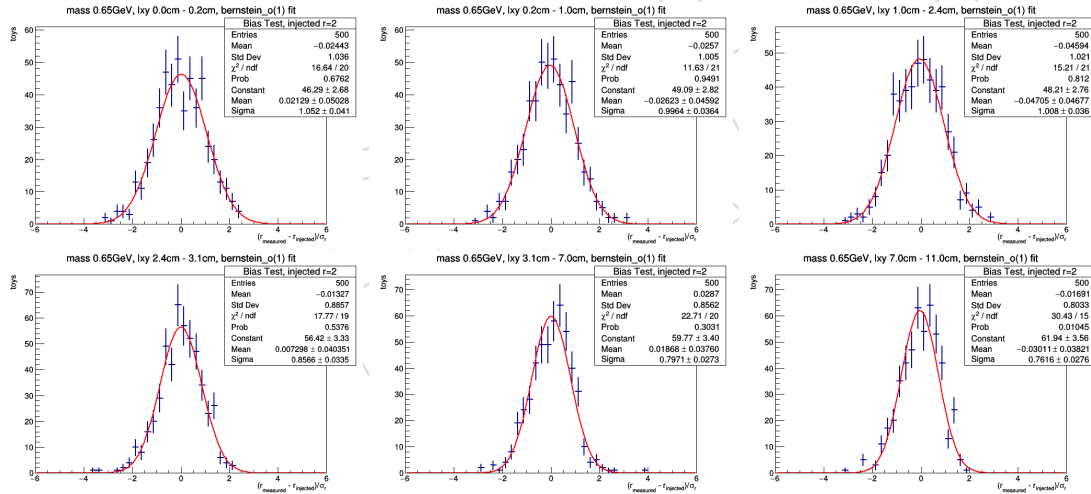
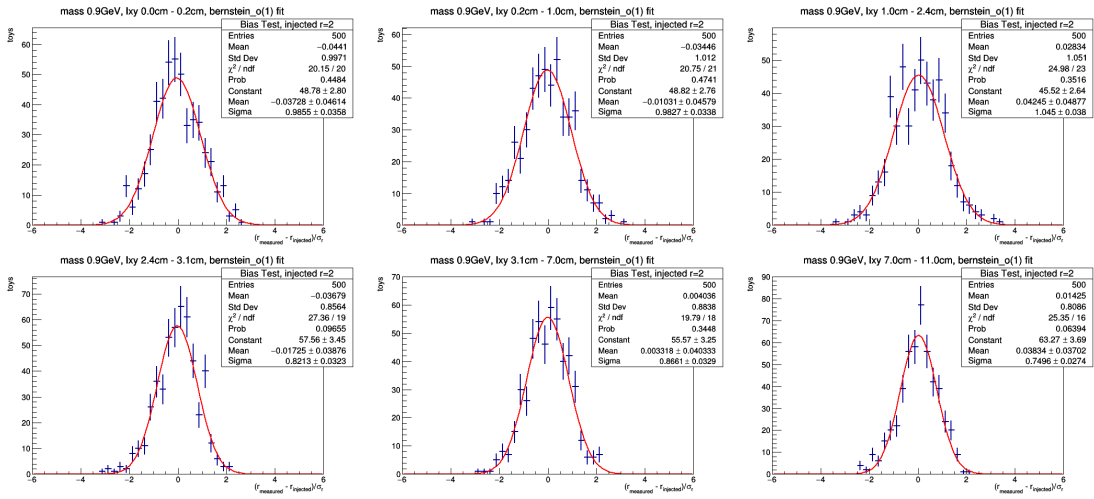
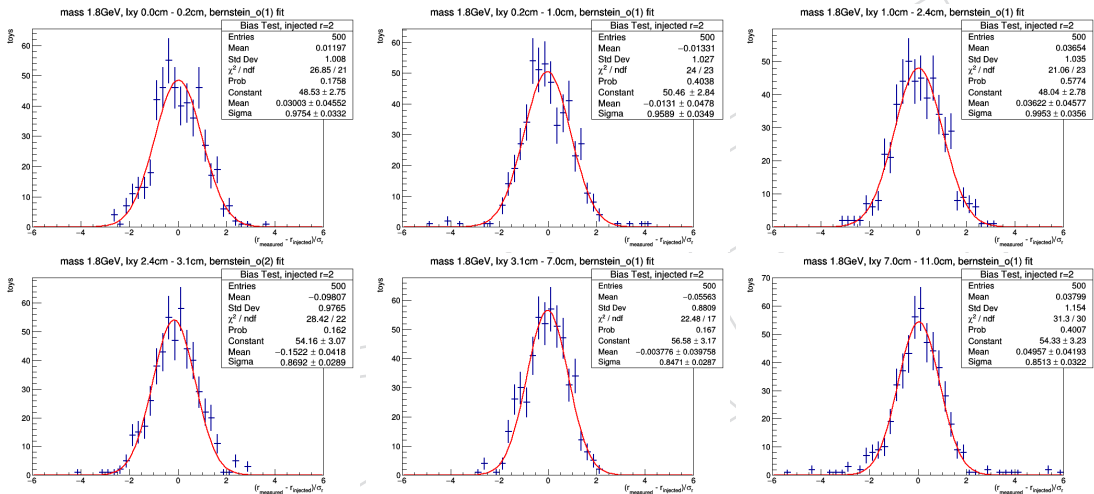
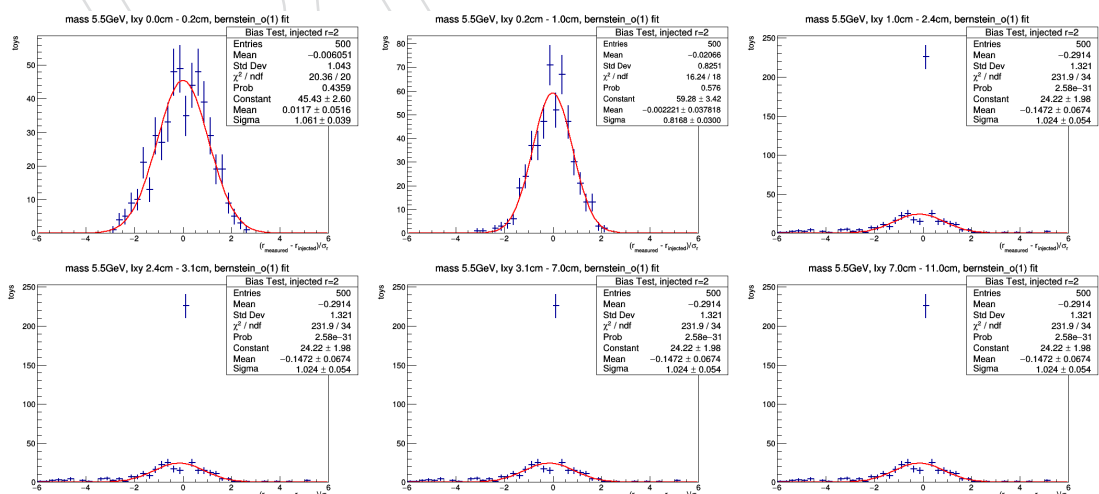


Figure 71: Bias test results in for $r_{\text{injected}} = 2$, for a signal mass hypothesis of 0.65 GeV.

Figure 72: Bias test results in for $r_{\text{injected}} = 2$, for a signal mass hypothesis of 0.9 GeV.Figure 73: Bias test results in for $r_{\text{injected}} = 2$, for a signal mass hypothesis of 1.8 GeV.Figure 74: Bias test results in for $r_{\text{injected}} = 2$, for a signal mass hypothesis of 5.5 GeV.

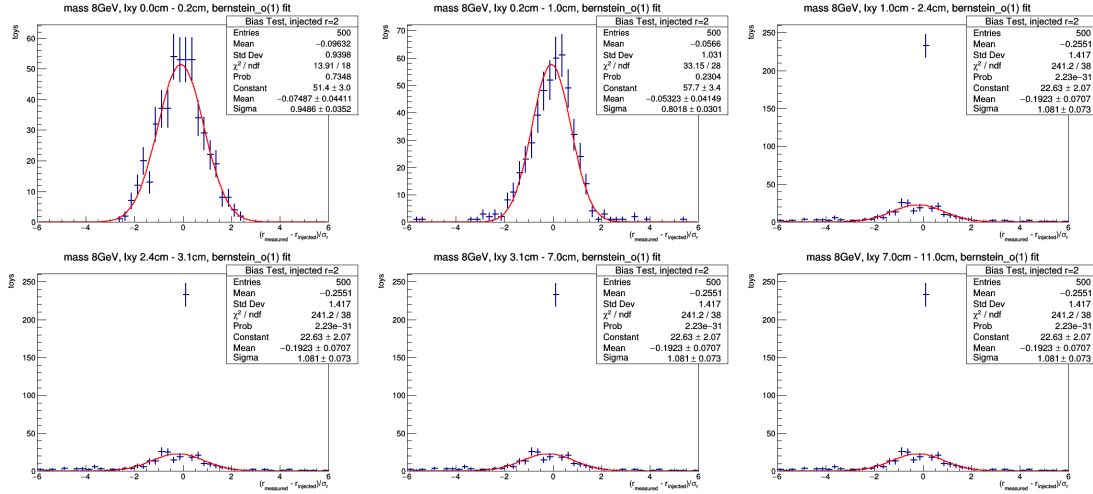


Figure 75: Bias test results in for $r_{\text{injected}} = 2$, for a signal mass hypothesis of 8.0 GeV.

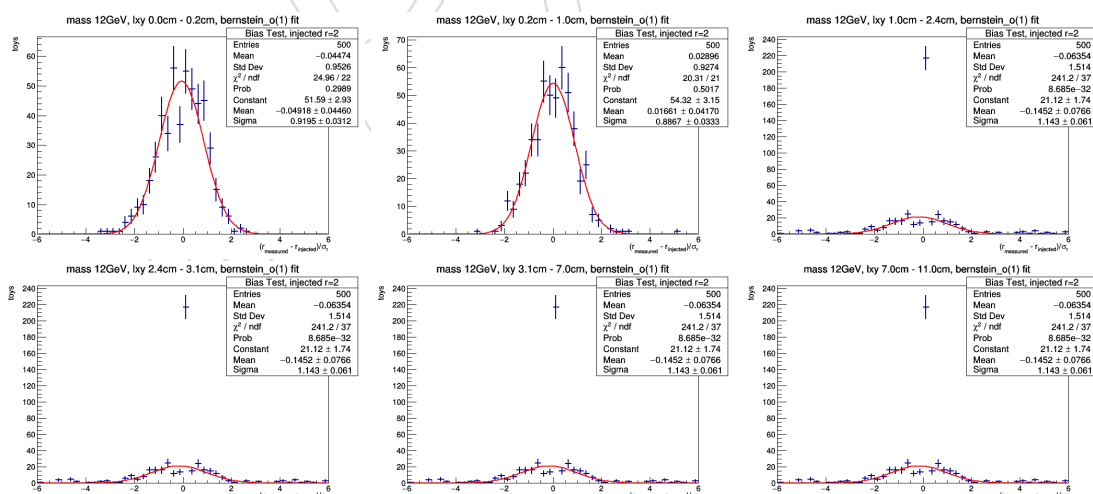


Figure 76: Bias test results in for $r_{\text{injected}} = 2$, for a signal mass hypothesis of 12.0 GeV.

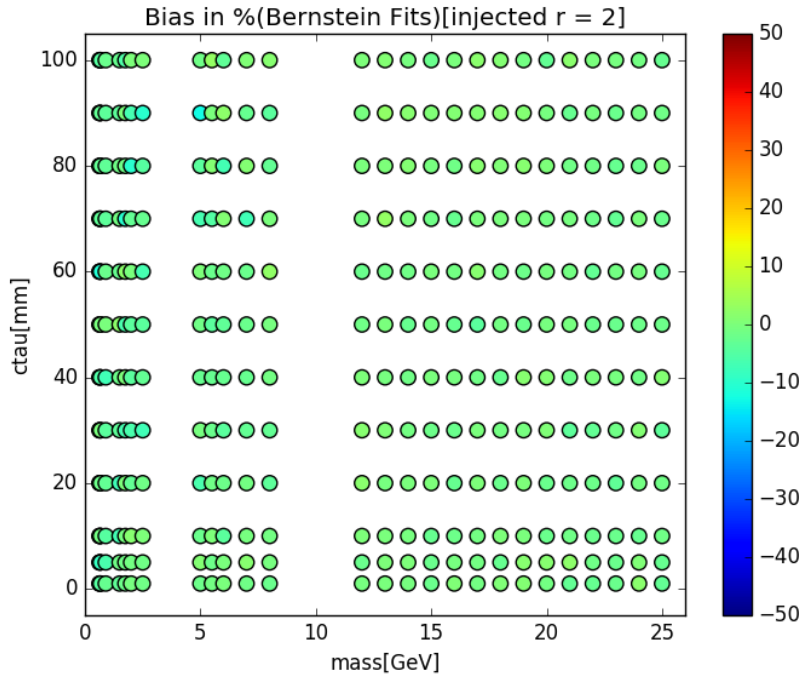


Figure 77: Mean bias (%) as a function of $(m, c\tau)$, for $r_{\text{injected}} = 2$.

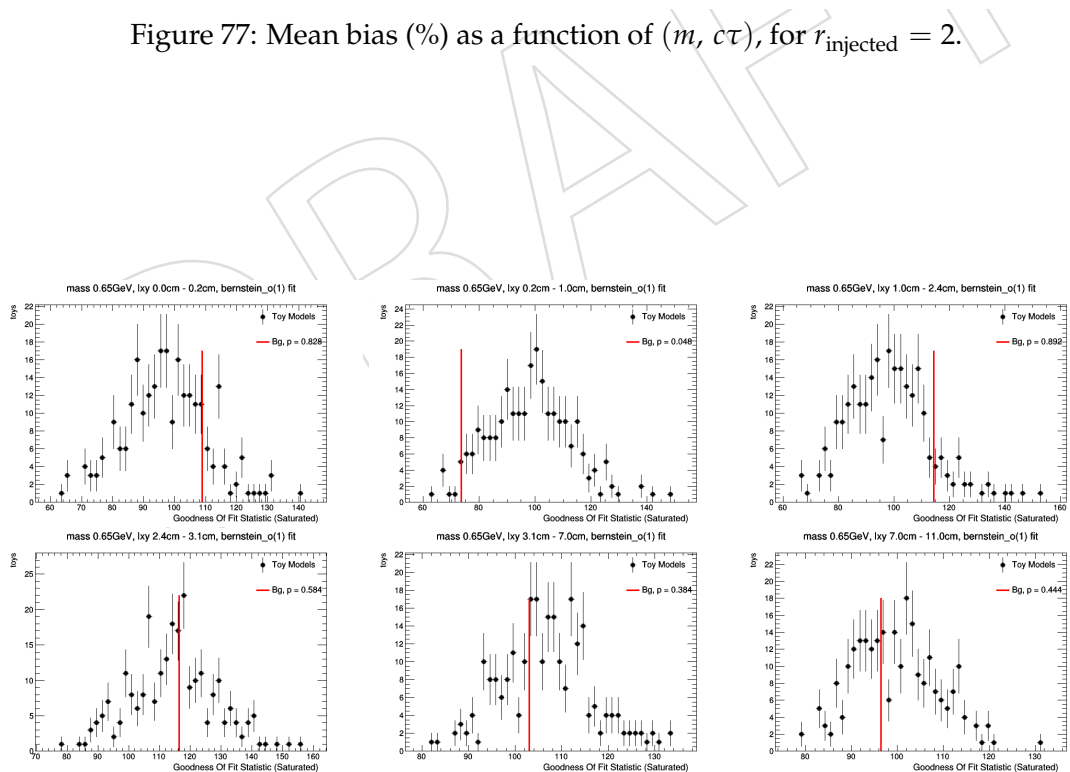


Figure 78: Goodness-of-fit test (saturated model) [54] results for a signal mass hypothesis of 0.65 GeV .

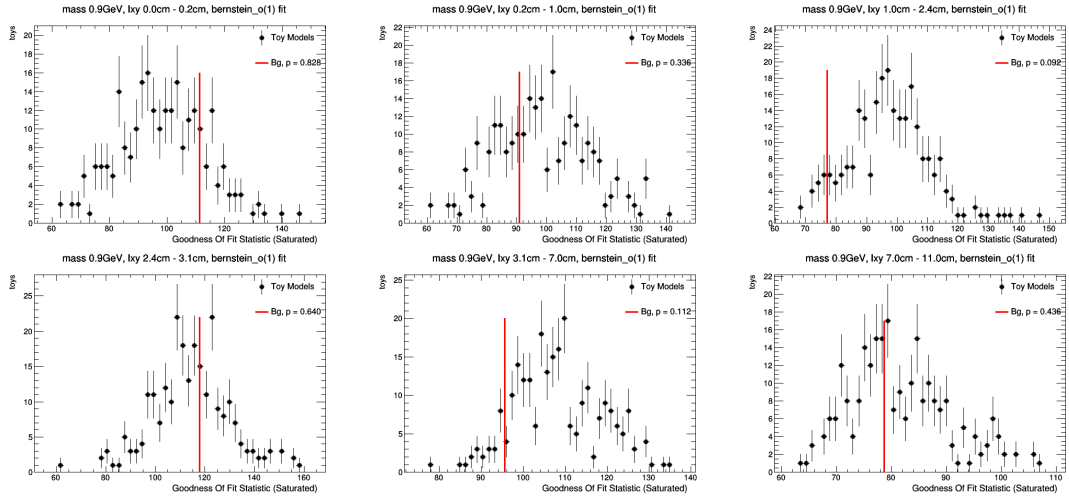


Figure 79: Goodness-of-fit test (saturated model) [54] results for a signal mass hypothesis of 0.9 GeV.

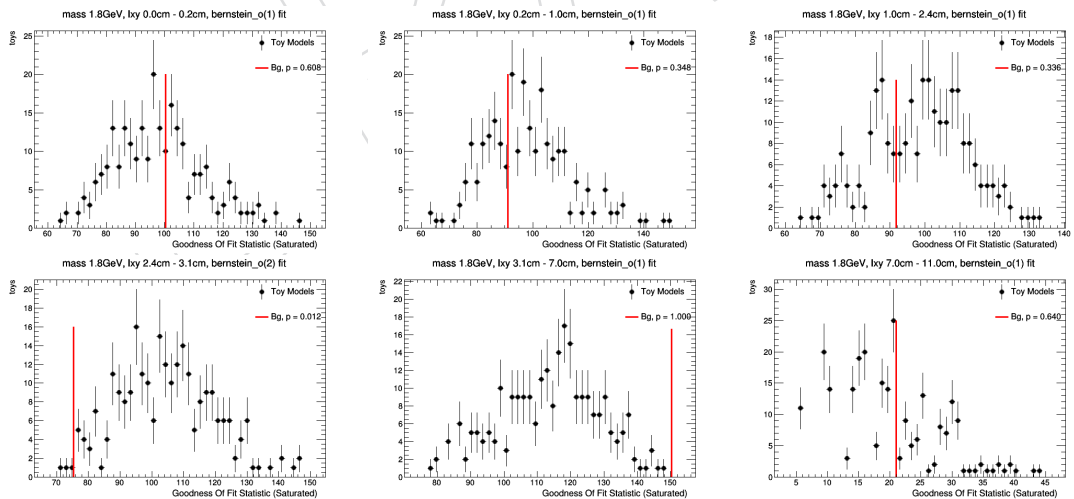


Figure 80: Goodness-of-fit test (saturated model) [54] results for a signal mass hypothesis of 1.8 GeV.

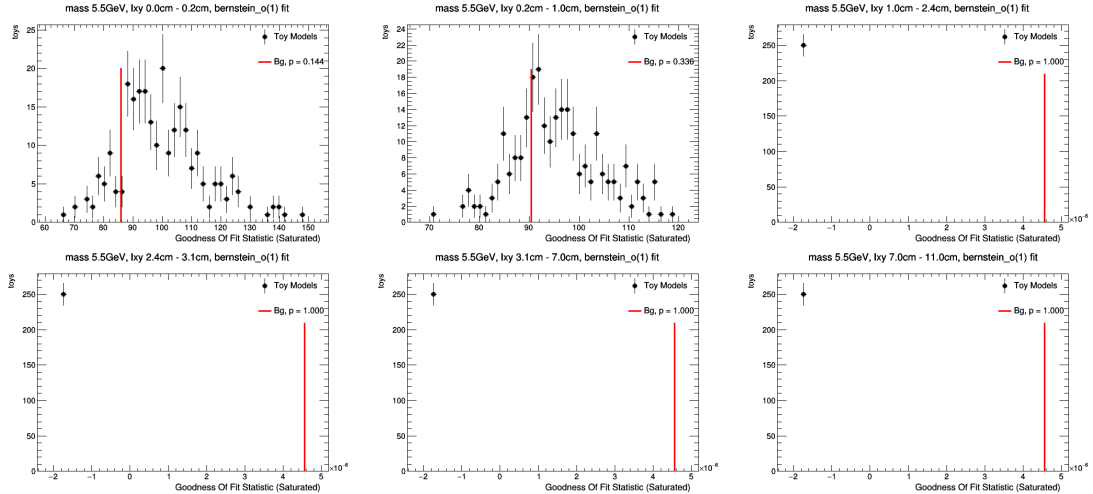


Figure 81: Goodness-of-fit test (saturated model) [54] results for a signal mass hypothesis of 5.5 GeV.

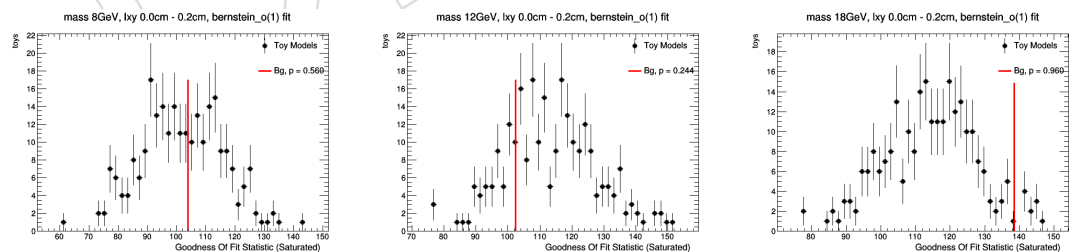


Figure 82: Goodness-of-fit test (saturated model) [54] results for a signal mass hypothesis of (left) 8.0 GeV and (right) 12.0 GeV.

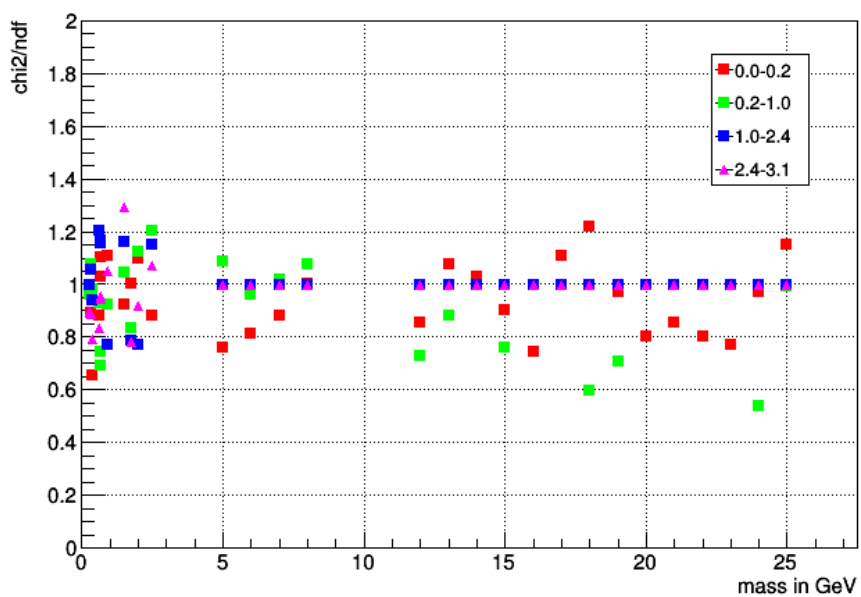


Figure 83: Distribution of χ^2/ndof for fits in different bins of l_{xy} , as a function of the signal mass hypothesis.

897 H On the choice of the background fit functional form

898 For the shape analysis, we use a polynomial functional form to parametrize the background
 899 dimuon mass spectrum in windows of $\pm 5\sigma$ around the signal mass hypothesis.

900 Different polynomial functional forms have been tested, including simple polynomials, Bern-
 901 stein polynomials, and Chebyshev polynomials. Bernstein and Chebyshev polynomials have
 902 been found to be stable across all of the search bins. In fact, polynomial functional forms are ex-
 903 pected to be equivalent to each other, except for potential numerical instabilities. We therefore
 904 choose to use Bernstein polynomials as a default choice.

905 In the following, we compare the background fit performance when Bernstein or Chebyshev
 906 polynomials are used. In particular, we compare the results of bias tests and goodness-of-fit
 907 (GOF) tests (see Appendix G).

908 Figure 84 shows the resulting mean bias (%) for the case where Chebyshev polynomials are
 909 used to fit the background component, as a function of $(m, c\tau)$, for $r_{\text{injected}} = 2$. As expected,
 910 there is no significant difference with respect to the case where Bernstein polynomials are used
 911 instead, as shown in Fig. 77 of Appendix G.

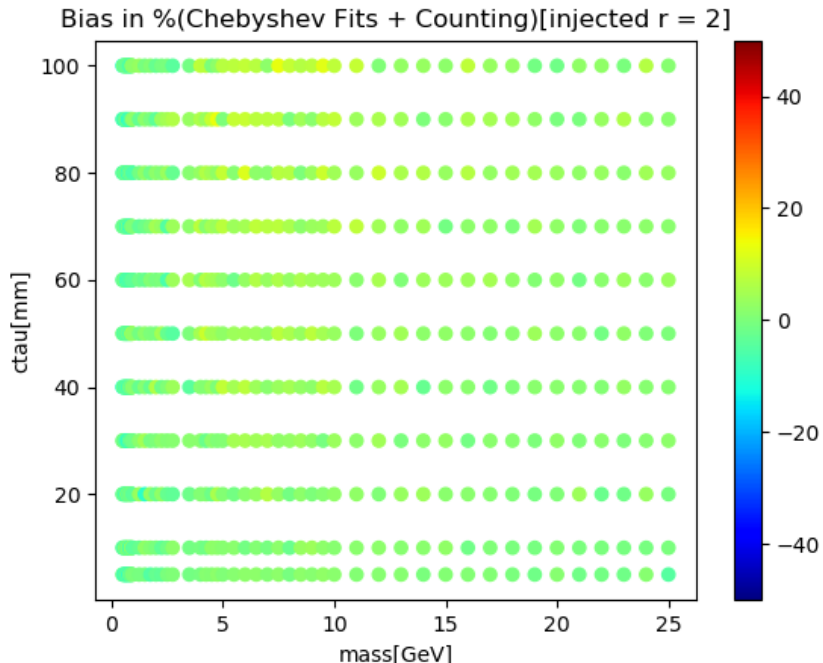


Figure 84: Mean bias (%) as a function of $(m, c\tau)$, for $r_{\text{injected}} = 2$, as obtained when Chebyshev polynomials are used to fit the background component.

912 As an additional figure of merit to evaluate the goodness of the fits, we also use the overall
 913 Figure 85 shows the overall χ^2/ndof in bins of l_{xy} as a function of the signal mass hypothesis
 914 under test, for the case where Chebyshev polynomials are used to fit the background compo-
 915 nent. As expected, there is no significant difference with respect to the case where Bernstein
 916 polynomials are used instead, as shown in Fig. 83 of Appendix G.

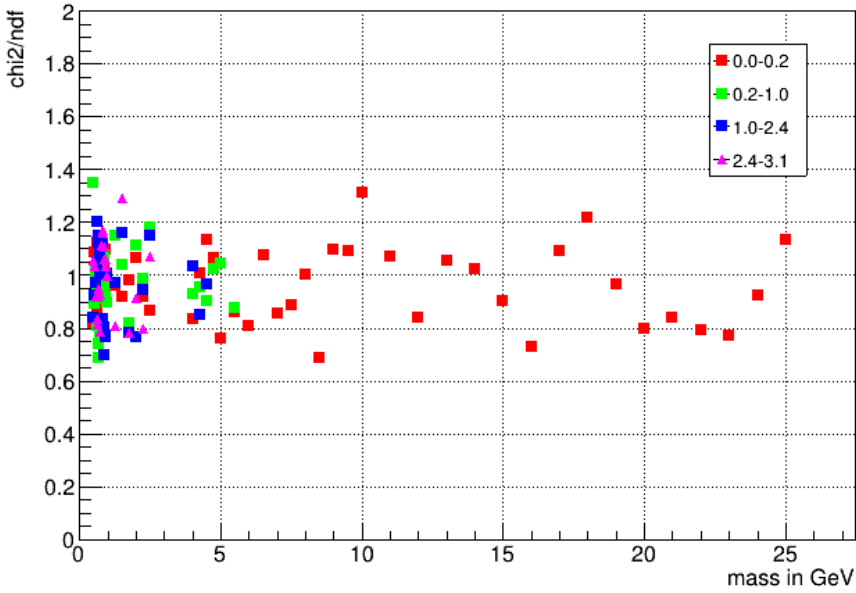


Figure 85: Distribution of χ^2/ndof for fits in different bins of l_{xy} , as a function of the signal mass hypothesis, as obtained when Chebyshev polynomials are used to fit the background component.

I Inclusive distributions

The events collected using the DST paths and L1T seeds detailed in Section 3.1, are preliminarily selected to contain at least a pair of oppositely charged (opposite-sign, OS) muons associated to a displaced vertex (DV). A large fraction of events contain only one OS muon pair and an associated DV. Among those events with more than a pair of OS muons, if more pairs satisfy the baseline selection described below then only the pair whose associated DV has the lowest transverse (x, y) error is used.

In the following, we collect distributions of the main selection variables, for data (10.1fb^{-1}) and illustrative signal models, after only selection requirements described in Sections 3.1, 5.1.1 and 5.1.2 are applied.

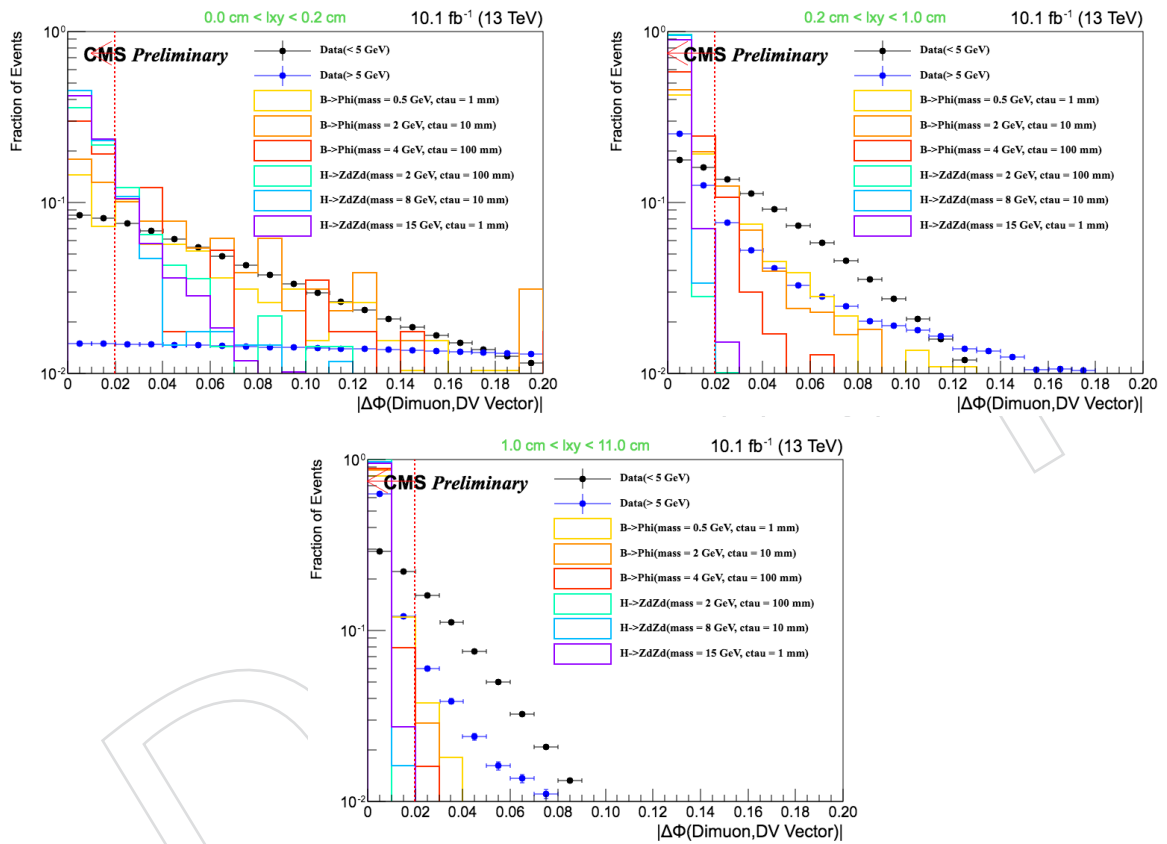


Figure 86: Distribution of $\Delta\phi(\mu, \bar{D}\bar{V})$ in data (10.1fb^{-1}) and illustrative signal models in three different l_{xy} ranges. The cut value is indicated by the red vertical dashed line. Only selections described in Sections 3.1, 5.1.1, and 5.1.2 are applied.

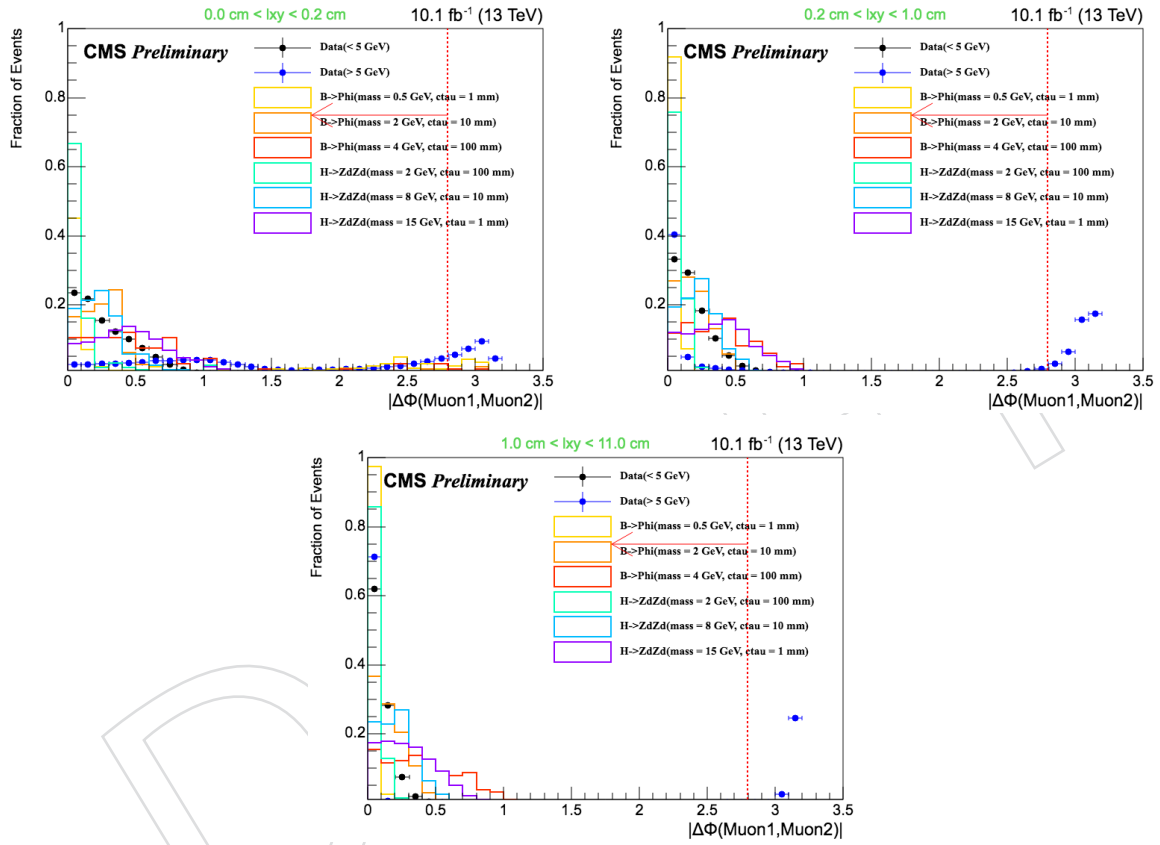


Figure 87: Distribution of $\Delta\phi(\mu, \mu)$ in data (10.1fb^{-1}) and illustrative signal models in three different l_{xy} ranges. The cut value is indicated by the red vertical dashed line. Only selections described in Sections 3.1, 5.1.1, and 5.1.2 are applied.

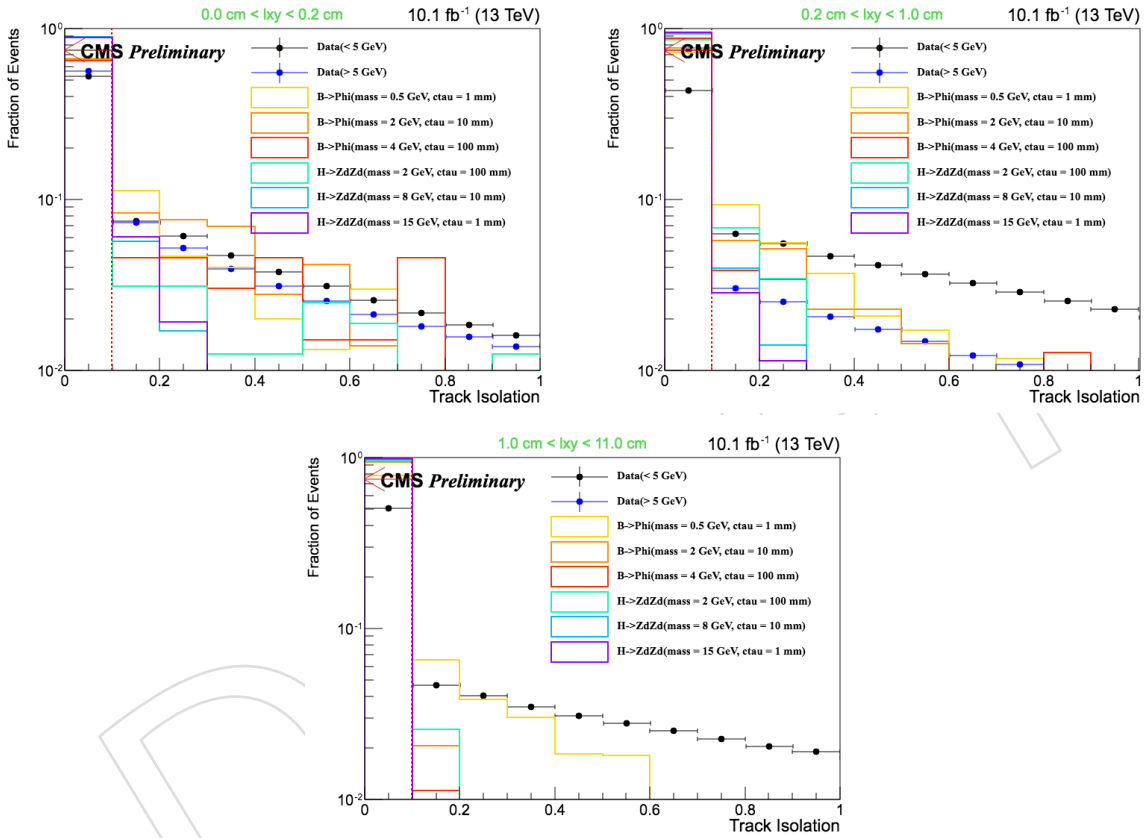


Figure 88: Distribution of the muon relative track isolation in data (10.1 fb^{-1}) and illustrative signal models, in three different l_{xy} ranges. The cut value is indicated by the red vertical dashed line. Only selections described in Sections 3.1, 5.1.1, and 5.1.2 are applied.

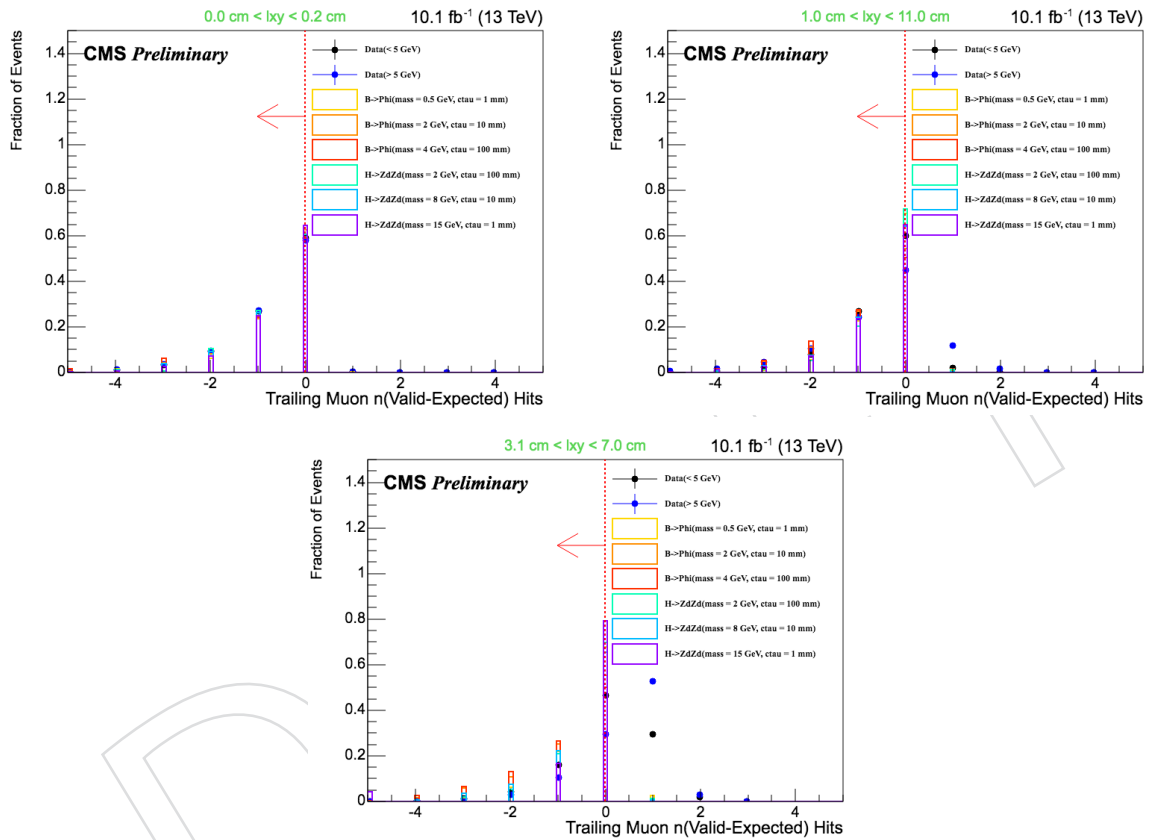


Figure 89: Distribution of number of excess pixel hits in data and illustrative signal models, in three different l_{xy} ranges. The cut value is indicated by the red vertical dashed line (the cut is only applied at $l_{xy} > 3.5 \text{ cm}$). Only selections described in Sections 3.1, 5.1.1, and 5.1.2 are applied.

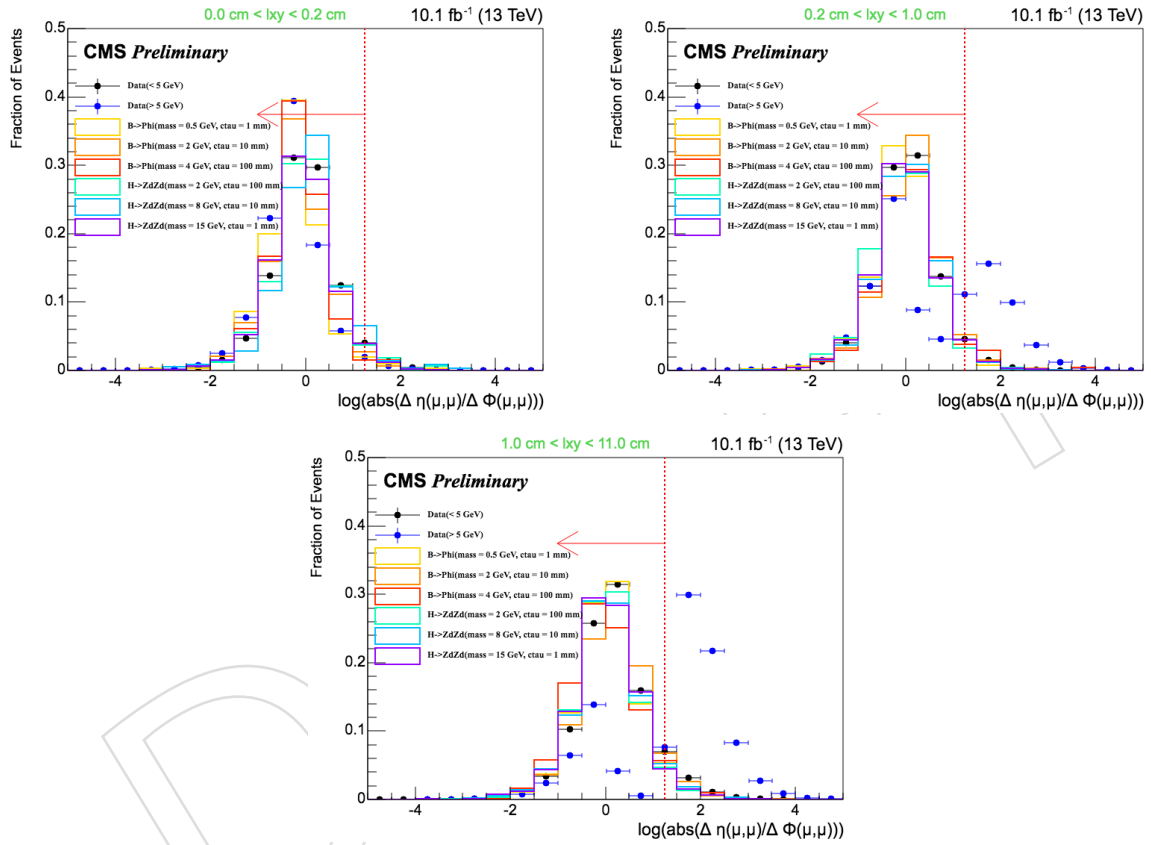


Figure 90: Distribution of $\log_{10}(|\Delta\eta_{\mu\mu}| / |\Delta\phi_{\mu\mu}|)$ in data (10.1fb^{-1}) and illustrative signal models in three different l_{xy} ranges. The cut value is indicated by the red vertical dashed line. Only selections described in Sections 3.1, 5.1.1, and 5.1.2 are applied.

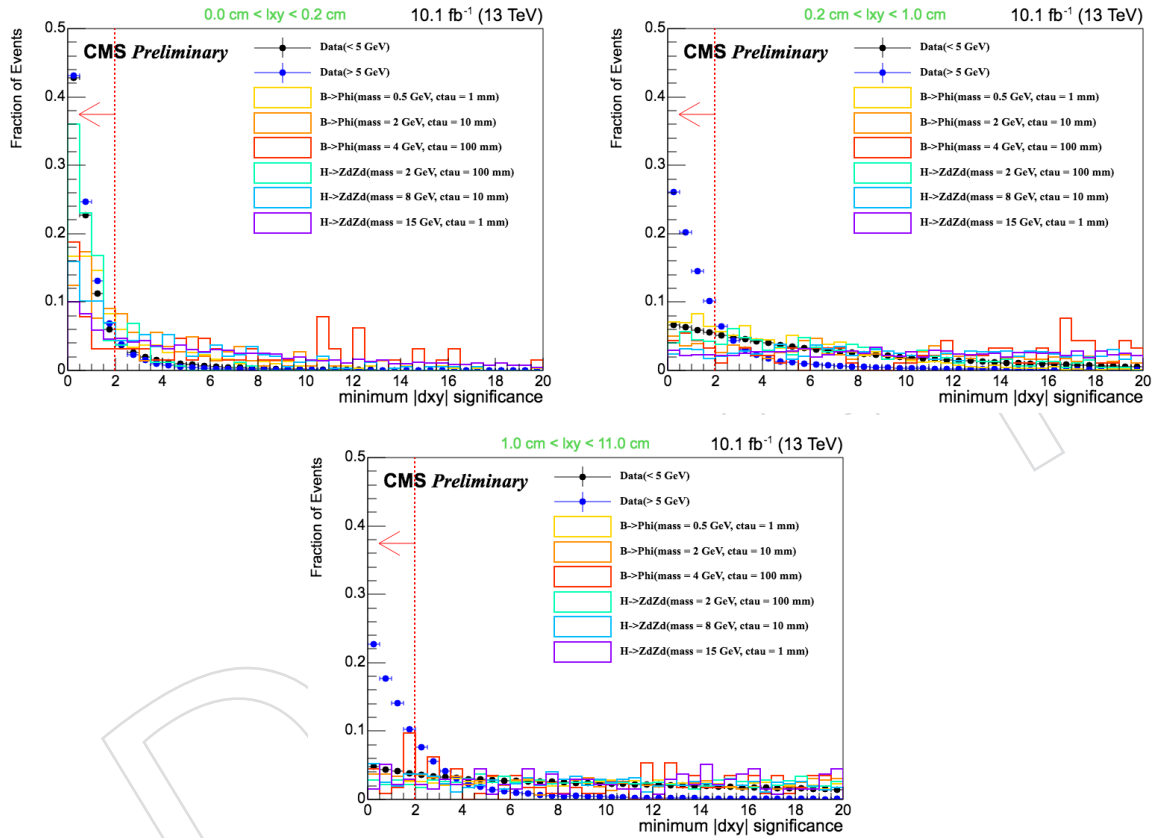


Figure 91: Distribution of $d_{xy}/\sigma_{d_{xy}}$ in data (10.1fb^{-1}) and illustrative signal models, in three different l_{xy} ranges. The cut value is indicated by the red vertical dashed line. Only selections described in Sections 3.1, 5.1.1, and 5.1.2 are applied.

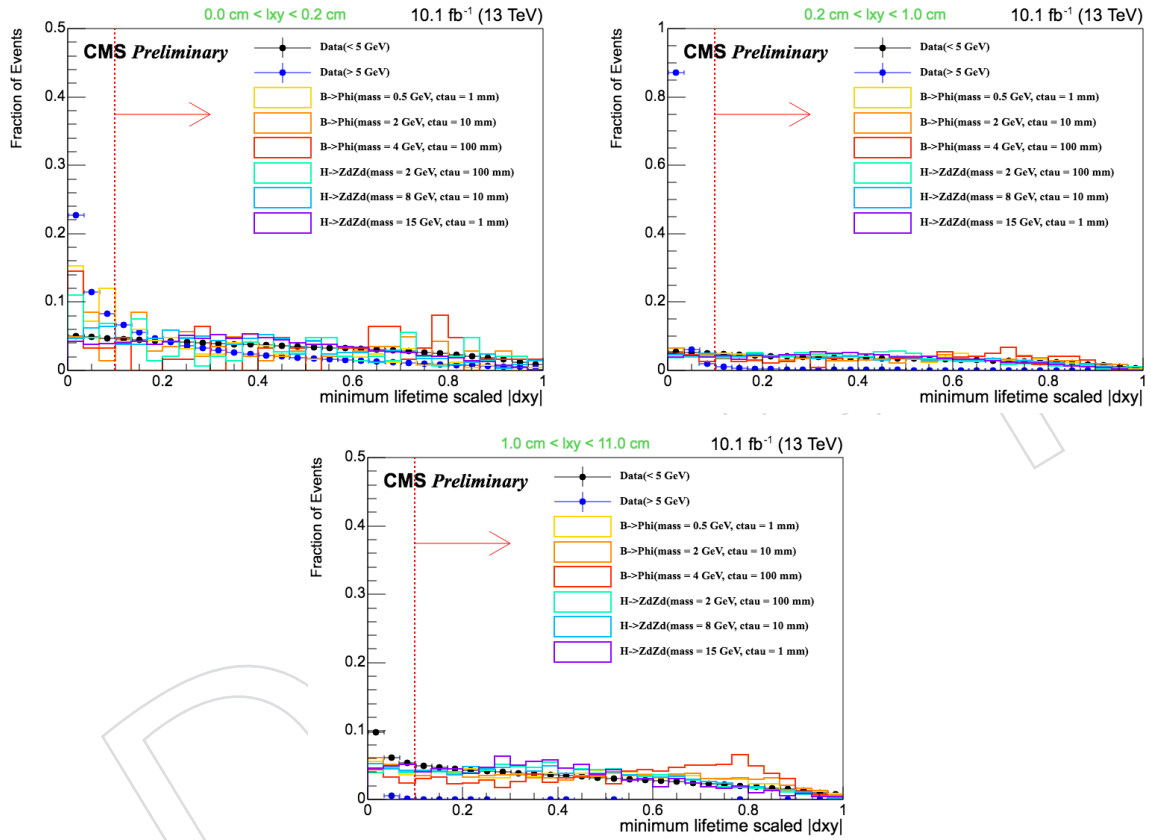


Figure 92: Distribution of $|d_{xy}| / (l_{xy} m_{\mu\mu} / p_T^{\mu\mu})$ in data (10.1fb^{-1}) and illustrative signal models, in three different l_{xy} ranges. The cut value is indicated by the red vertical dashed line. Only selections described in Sections 3.1, 5.1.1, and 5.1.2 are applied.

927 J Selection cut-flow

928 Table 4 lists the cut-flow of unweighted events passing sequential selections developed in this
 929 analysis. Yields are split into low and high mass regions for data, and low and high transverse
 930 displacement for both data and signal models.

Table 4: Analysis cut-flow for data (10.1fb^{-1}) and selected signal models. Values represent unweighted events.

Selection	Data (< 5 GeV)		Data (> 5 GeV)		$H \rightarrow Z_d Z_d$ (2 GeV, $c\tau=1$ mm)		$H \rightarrow Z_d Z_d$ (2 GeV, $c\tau=10$ mm)		$H \rightarrow Z_d Z_d$ (8 GeV, $c\tau=100$ mm)	
	$l_{xy} < 1\text{ cm}$	$l_{xy} > 1\text{ cm}$	$l_{xy} < 1\text{ cm}$	$l_{xy} > 1\text{ cm}$	$l_{xy} < 1\text{ cm}$	$l_{xy} > 1\text{ cm}$	$l_{xy} < 1\text{ cm}$	$l_{xy} > 1\text{ cm}$	$l_{xy} < 1\text{ cm}$	$l_{xy} > 1\text{ cm}$
Trigger, DV + 2 OS muons	280698463	3304466	46316053	108375	44301	73114	5509	28226	167	1042
Muon ID	270898775	3146897	44725033	91186	43933	72649	5466	28062	164	1040
Muon Iso.	100751784	840381	17704663	40702	37293	66169	4594	26064	148	1003
$\Delta\phi(\mu, \mu) < 2.8$	100751784	840381	12110510	30093	37062	66166	4581	26063	148	1003
$\Delta\phi(\mu, \overrightarrow{\text{DV}}) < 0.02$	11804721	356795	152944	10249	34187	66155	4262	26058	137	995
Excess hit veto	11804721	349627	152944	9377	34187	65424	4262	25307	137	958
Material veto	11804721	343449	152944	9181	34187	63886	4262	24741	137	933
$\log_{10}(\Delta\eta_{\mu\mu} / \Delta\phi_{\mu\mu}) < 1.25$	11312762	301663	128883	35	33082	61476	4117	23790	128	898
$d_{xy}/\sigma_{d_{xy}} > 2$	6260014	273746	10806	25	24624	60262	3152	23570	121	896
$ d_{xy} / (l_{xy} m_{\mu\mu} / p_T^{\mu\mu}) > 0.1$	6197560	245967	10037	0	24381	55576	3112	21625	114	798

DRAFT